TÉCNICO LISBOA

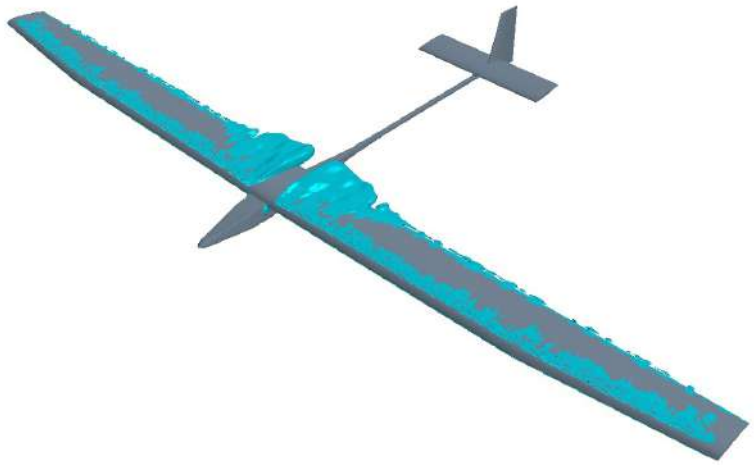

Parametric Design, Aerodynamic Analysis and Parametric Optimization of a Solar UAV

Nuno Miguel António Silva

Thesis to obtain the Master of Science Degree in

Aerospace Engineering

Supervisors: Professor André Calado Marta and Doctor José Manuel da Silva Chaves Ribeiro Pereira

Examination Committee

Chairperson:	Professor Fernando José Parracho Lau
Supervisor:	Professor André Calado Marta
Member of the Committee:	Professor Filipe Szolnoky Ramos Pinto Cunha

June 2014

To my parents. For their love and support.

Acknowledgments

My most sincere thanks to:

First and foremost, my supervisors Professor André Calado Marta and Dr. José Manuel da Silva Chaves Ribeiro Pereira for their patience, guidance and support throughout the period it took me to complete this thesis.

LASEF for the use of its installations and resources.

The LASEF team that relentlessly helped me when any technical adversities occurred when using their equipment in order to perform all the aerodynamic simulations.

My family and friends for their constant support and belief in me through the years.

Resumo

O objectivo desta tese foi desenvolver uma ferramenta CAD que faça uso de scripts por forma a desenhar diferentes configurações de UAVs e a posterior análise aerodinâmica dessas configurações. Com recurso ao Star-CCM+ analisou-se um UAV em particular. O UAV de estudo consiste num Long Endurance Electric UAV (LEEUAV). O LEEUAV, foi submetido a uma série de estudos aerodinâmicos onde se usou os modelos de turbulência Spalart-Allmaras e $k-\omega$ SST, este último usado em conjunto com o modelo de transição $\gamma - Re_\theta$, e os seus resultados comparados com dados experimentais. Apenas o modelo de turbulência $k-\omega$ SST em conjunto com o modelo de transição $\gamma - Re_\theta$ foram usados nas simulações aerodinâmicas mais detalhadas. Em voo cruzeiro, o LEEUAV apresenta uma razão de finesse de 14.01, velocidade de perda de 6.21 m/s e velocidade máxima em voo cruzeiro de 29.3 m/s. Para melhorar a performance do LEEUAV implementaram-se estudos paramétricos à forma do nariz, asa e fuselagem. Com a modificação da forma do nariz, os gradientes de pressão adversos aí localizados foram eliminados ou diminuídos. Com a ponta da asa arredondada reduziu-se em 3 cm as bolhas de separação laminares na asa. Modificando a geometria da raiz da asa eliminou-se uma zona de escoamento separado que se gerava a partir dos 2º. Diminuindo o ângulo de incidência da asa permitiu-se o controlo através de ailerons até pelo menos 10º.

Palavras-chave: UAV Solar, Longo Alcance, Propulsão Híbrida, CFD, CAD, Modelação Paramétrica, Análise de Sensibilidade.

Abstract

The aim of this thesis was to develop and implement a computational process to enable the swift design of different UAV configurations and their aerodynamic analysis. To this end, a CAD tool using scripts was adopted to define the UAV external shape which was later imported into a CFD tool to generate suitable meshes. The test case consisted of a Long Endurance Electric UAV (LEEUAV), that was aerodynamically analyzed and parametrically optimized. While performing the aerodynamic analyses, turbulence models Spalart-Allmaras and $k-\omega$ SST, the later being employed in tandem with the $\gamma - Re_\theta$ transition model, were employed and their predictions compared with experimental data. Only the $k-\omega$ SST turbulence model and the $\gamma - Re_\theta$ transition model were employed in the detailed aerodynamic simulations. During cruise, the baseline LEEUAV presents a lift-to-drag ratio of 14.01, stall speed of 6.21 m/s and maximum cruise speed of 29.3 m/s. To enhance the baseline cruise performance, a series of parametric optimization and sensitivity studies were performed where its nose, wing and fuselage shapes were modified. With the nose shape modification proposal, the adverse pressure gradients that previously existed in that surface were reduced. With rounded wingtips, the wing long laminar separation bubbles were predicted to decrease. With the proposed wing root fairing, a region of separated flow that formed beginning at 2º disappeared thus reducing the aircraft drag. With the proposed wing washout, aileron control effectiveness was extended to angles of attack up to 10º.

Keywords: Solar UAV, UAV Airframe, Long Endurance, Hybrid Propulsion, Computational Fluid Dynamics, Computer-Aided Design, Parametric Modeling, Sensitivity Analysis.

Contents

List of Tables

List of Figures

Nomenclature

Greek symbols

α Angle of attack.

α_{0lift} Zero lift angle of attack.

$\alpha_{\frac{CL^{\frac{3}{2}}}{CD}_{max}}$ Three-dimensional angle of attack of the maximum lift$^{3/2}$-to-drag ratio.

$\alpha_{\frac{Cl^{\frac{3}{2}}}{Cd}_{max}}$ Two-dimensional angle of attack of the maximum lift$^{3/2}$-to-drag ratio.

$\alpha_{\frac{CL}{CD}_{max}}$ Three-dimensional angle of attack of maximum lift-to-drag ratio.

$\alpha_{\frac{Cl}{Cd}_{max}}$ Two-dimensional angle of attack of maximum lift-to-drag ratio.

$\alpha_{C_{Lmax}}$ Three-dimensional maximum lift angle of attack.

$\alpha_{C_{lmax}}$ Two-dimensional maximum lift angle of attack.

ϵ Turbulent dissipation.

η_{total} Propulsive system total efficiency.

γ Intermittency factor.

κ Turbulent kinetic energy.

μ Molecular viscosity coefficient.

μ_t Eddy viscosity.

ν Kinematic viscosity coefficient.

ν_t Kinematic eddy viscosity.

$\tilde{\nu}$ Kinematic eddy viscosity factor.

Ω Vorticity.

ω Specific turbulence dissipation rate.

ρ Density.

τ Wall shear stress.

τ_{ij} Wall shear stress tensor.

Roman symbols

a Speed of sound.

A Wing aspect ratio.

b Wingspan.

c Wing section chord.

C_D Three-dimensional drag coefficient.

C_d Two-dimensional drag coefficient.

$C_{D,0}$ Three-dimensional zero lift drag coefficient.

$C_{d,0}$ Two-dimensional zero lift drag coefficient.

C_{Dmin} Three-dimensional minimum drag coefficient.

C_{dmin} Two-dimensional minimum drag coefficient.

C_L Three-dimensional lift coefficient.

C_l Two-dimensional lift coefficient.

$\frac{C_l^{\frac{3}{2}}}{C_d}$ Two-dimensional lift$^{3/2}$-to-drag ratio.

$\frac{C_L^{\frac{3}{2}}}{C_D}$ Three-dimensional lift$^{3/2}$-to-drag ratio.

$\frac{C_l^{\frac{3}{2}}}{C_d}_{max}$ Two-dimensional maximum lift$^{3/2}$-to-drag ratio.

$\frac{C_L^{\frac{3}{2}}}{C_D}_{max}$ Three-dimensional maximum lift$^{3/2}$-to-drag ratio.

$C_{l\alpha}$ Two-dimensional lift vs α curve slope.

$C_{L\alpha}$ Three-dimensional lift vs α curve slope.

$\frac{C_l}{C_d}$ Two-dimensional lift-to-drag ratio.

$\frac{C_L}{C_D}$ Three-dimensional lift-to-drag ratio.

$\frac{C_l}{C_d}_{max}$ Two-dimensional maximum lift-to-drag ratio.

$\frac{C_L}{C_D}_{max}$ Three-dimensional maximum lift-to-drag ratio.

C_{Lmax} Maximum three-dimensional lift coefficient.

C_{lmax} Maximum two-dimensional lift coefficient.

$\bar{c}$ Wing section mean chord.

C_M Three-dimensional moment coefficient.

C_m Two-dimensional moment coefficient.

C_p Pressure coefficient.

E Aircraft endurance.

E^* Battery specific energy.

g Gravitational acceleration.

L Aircraft lift.

m Aircraft total mass.

Ma Mach number.

m_{batt} Battery mass.

p Pressure.

R Aircraft range.

Re Reynolds number.

S Wing planform area.

t Time.

Ti Turbulence intensity.

U Velocity vector.

U_{cruise} Cruise velocity.

W Aircraft weight.

$y+$ Dimensionless wall distance.

Subscripts

∞ Free-stream condition.

$c/4$ Conditions at the quarter-chord point.

i, j, k Computational indexes.

max Maximum conditions.

min Minimum conditions.

$stall$ Stall conditions.

x, y, z Cartesian components.

Glossary

AoA	Angle of attack.
CAD	Computer-aided design (CAD) is the use of computer systems to assist in the creation, modification, analysis, or optimization of a design.
CAE	Computer-aided engineering (CAE) is the broad usage of computer software to aid in engineering analysis tasks.
CFD	Computational fluid dynamics (CFD) is a branch of fluid mechanics that uses numerical methods and algorithms to solve and analyze problems that involve fluid flows.
DES	Detached eddy simulation (DES) is a modification of a RANS model in which the model switches to a subgrid scale formulation in regions fine enough for LES calculations.
FreeCAD	FreeCAD is an open-source three-dimensional modeler.
GUI	Graphical User Interface (GUI) is a user interface that allows users to interact with electronic devices through graphical icons and visual indicators such as secondary notation, as opposed to text-based interfaces, typed command labels or text navigation.
IGES	The Initial Graphics Exchange Specification (IGES) is a file format which defines a vendor neutral data format that allows the digital exchange of information among CAD systems.
LEEUAV	Long Endurance Electric Unmanned Aerial Vehicle.

LES Large Eddy Simulation (LES) is a model for simulating turbulent flows used in CFD where the larger three-dimensional unsteady turbulent motions are directly represented, whereas the effects of the smaller scale motions are modeled.

LSB Laminar Separation Bubble.

RANS Reynolds Averaged Navier–Stokes equations are time averaged equations of motion for fluid flow.

SA Spalart-Allmaras turbulence model.

STEP International CAD standard for product data exchange protocols.

STL STL is also known as Standard Tessellation Language. This file format is supported by many software packages and it is widely used for rapid prototyping and computer-aided manufacturing.

Star-CCM+ Star-CCM+ is a commercial CFD software package capable of managing multi-physics and complex geometries.

TS Turbulence Suppression model.

UAS An Unmanned Aerial System (UAS) refers to the systems involved in a UAV control such as the UAV itself, the control station or the on ground personnel.

UAV An Unmanned Aerial Vehicle (UAV) is an aircraft without a human pilot aboard.

XFOIL XFOIL is an interactive program for the design and analysis of subsonic isolated airfoils.

Chapter 1

Introduction

1.1 Motivation

Nowadays, with the advent of personal computers and with their increasing memory capacity and processing power, performing tortuous tasks such as designing complex geometries or implementing and running demanding algorithms that no longer than a decade ago would take days if not weeks to accomplish is now easier than ever to do. Designing complex geometries such as aircraft wings, wing root fairings, vertical and horizontal stabilizers, not to mention intricate geometries like engines and their nacelles or pylons, had the potential to turn a seemingly straightforward task into an exasperating one. Luckily, times have changed and nowadays designing aircrafts and running complex aerodynamic algorithms has become increasingly easy and accessible.

This thesis aims to make good use of the current computer capabilities of both commercial and open source software packages by developing a design tool that enables the swift design of complex Unmanned Aerial Vehicles (UAVs) geometries through the use of Computed-Aided Design (CAD) tools and providing rapid and reliable aerodynamic data in order to validate specific UAV configurations given key mission objectives. This tool was developed with the objective of being in between the conceptual and detailed UAV design phases so that after designing a specific UAV configuration the engineer would send that model into a Computational Fluid Dynamics (CFD) software package and collect valuable aerodynamic data so that a decision is made about whether a specific configuration would or would not satisfy the project objectives.

1.2 Objectives

This thesis takes part in a project proposal by several major institutions, one of them being the Laboratório Associado para a Energia, Transportes e Aeronáutica (LAETA) and was developed at the Laboratory of Fluid Simulation in Energy and Fluids (LASEF) and the Aerospace Section at Instituto Superior Técnico. The project is addressed as Long Endurance Electric UAV (LEEUAV) and its goals are to develop a low cost, small footprint, easy to build and maintain multirole electric UAV, capable of being

deployed from short airfields and highly flexible in such ways that it is able to adapt to different civilian surveillance missions, thus not being restricted to specific mission profiles.

Although such a project covers numerous areas of expertise such as aerodynamics, propulsion, structures and materials, aerospace design, optimization, among others, this thesis focuses on completing a cycle that starts with the definition of a UAV geometry parameters, builds that UAV using custom made scripts together with a CAD software, sends that UAV geometry onto a CFD software package in which thorough aerodynamic analyses are performed and, finally, the data is collected and processed. The aerodynamic data can then be used by an optimization algorithm to further enhance any UAV geometry thus completing an optimization cycle.

The designer will be working with scripts where the dimensions of a UAV different components will be provided. Those scripts will then interact with a CAD program that parametrically builds the different UAV airframe components such as the main wing, fuselage and tail. After building and assembling that UAV, several object and mesh files containing the different components are generated and sent to the CFD software. At this time, the CFD software will import and the designed UAV, generate surface and volume meshes and finally run the required aerodynamic analysis for different flight conditions. After these processes are completed, the CFD software will write and export several files containing aerodynamic data of that particular UAV. Figure 1.1 shows the UAV design cycle and the designer has the option of performing as many design iterations as needed in order to follow specific mission objectives.

In this thesis, one UAV configuration in particular will be the object of the geometric modeling, aerodynamic analyses and parametric optimization. That UAV will be addressed as LEEUAV throughout this thesis.

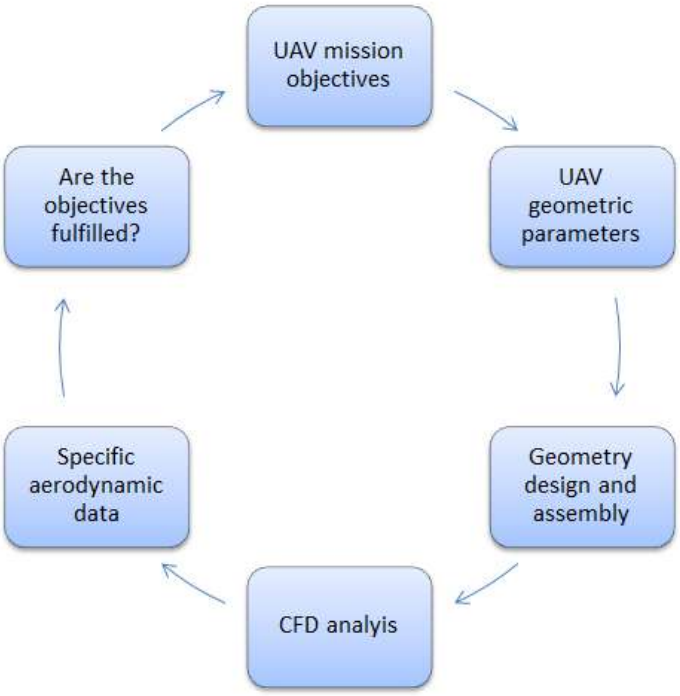

Figure 1.1: Design cycle.

1.3 Document Structure

This thesis is divided into eight chapters. The first chapter, provides an introduction and motivation for this thesis. The second chapter introduces the project in which this thesis is included. The third chapter deals with the CAD software selection processes and LEEUAV geometry design methodologies. The fourth chapter addresses the CFD software and turbulence models selection later employed in the aerodynamic studies. The fifth and sixth chapters are relative to the two- and three-dimensional aerodynamic studies on the LEEUAV airfoil and complete geometry, respectively. The seventh chapter introduces different parametric optimization studies based on the baseline LEEUAV aerodynamic performance. The eighth chapter addresses the work developed in this thesis and provides conclusions and suggestions for future work.

1.4 UAVs - Historical Perspective & State-of-the-Art

Since the beginning of time human beings look up to the skies and wish to fly as birds. A great example of such desires and ambitions is the Greek mythology tale of Daedalus and Icarus [1]. Like Icarus, we wish to see the world from above and covet the freedom only a select few animals have. Not being naturally apt to fly, human beings started experimenting and thinking of ways of experiencing flight. Leonardo da Vinci's Ornithopter [2] is an exquisite example of such efforts. There is no definite proof that this machine was actually built but its working mechanisms, as seen in Figure 1.2, were to mimic the flapping wing movement of birds. In 1709, Portuguese priest Bartolomeu de Gusmão came up with the Passarola [3] which was an airship that ascended through the skies by means of hot air. Later in the second half of that century the Montgolfier brothers designed and built hot air balloons that ascended and flew several kilometers across Paris [4]. Human beings were one step closer to conquer the skies. However, despite the success of actually flying through the skies, those balloons were not meant to achieve high velocities and maneuverability. This feat was achieved by George Cayley in 1799 and his airplane designs included a fixed wing to generate lift, a propulsion system to produce thrust and a cruciform tail for stabilization purposes [5]. By 1905 the Wright brothers invented the first practical airplane, the Flyer III, as illustrated in Figure 1.3.

Since the beginning of the twentieth century, airplanes and aviation in general have made tremendous advances, and the majority of them, understandingly, due to military conflicts. Throughout last century, tremendous efforts were made for the development and improvement of UAVs. These are powered aerial vehicles that do not carry human pilots, use aerodynamic forces to provide lift, can fly autonomously or be piloted remotely, can be expendable and carry payload. UAVs are predominantly used in military aviation but are increasingly being employed in civil aviation and science research missions. The range of applicability is so vast that these machines are used to carry out tasks such as aerial surveillance (livestock monitoring, wildfire mapping, pipeline security, home security, road patrol, anti-piracy), oil and mineral exploration and production means (UAVs can be used to perform geophysical surveys in order to calculate the nature of the soil in certain areas through the reading of the local gravity

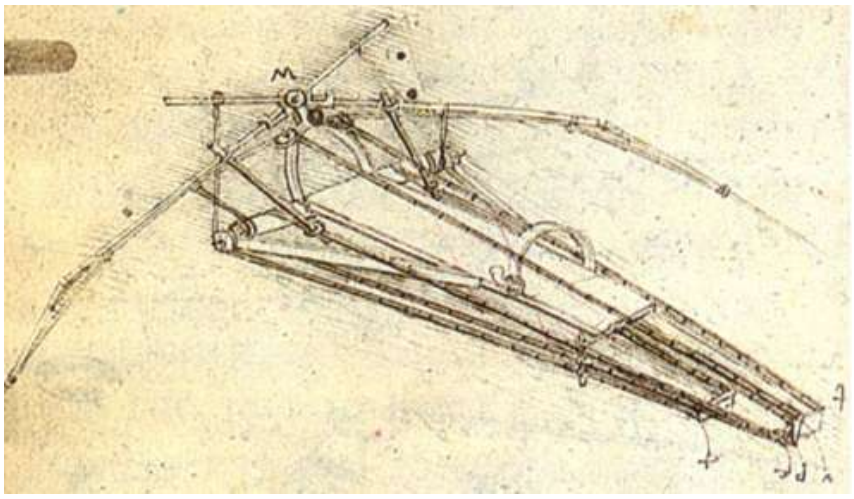

Figure 1.2: Sketch of Leonardo da Vinci's Ornithopter. [2]

Figure 1.3: Wright brothers' Flyer III. [6]

field), scientific research (UAVs are especially useful in penetrating areas that may be too dangerous for manned aircrafts), search and rescue (such as in hurricane search and rescue missions), conservation, forest fire detection (prevention and early detection of forest fires), among many more tasks.

Usually the propulsion of these vehicles is ensured by engines that function on oil derivatives. The reason is simple, these engines are widely used, well studied and reliable. However, throughout the last forty years, energy crisis have been a worldwide constant and most of these were oil crises. Naturally, in an effort to avoid serious social and economic implications due to global decline in oil production in the coming decades, there is the need to find alternatives at least ten to twenty years before the peak of global petroleum extraction [7]. Furthermore, with the continuing rise in the average temperature of the Earth atmosphere [8] and its side-effects which are believed to be a direct consequence, among other things, of the increasing and incessant consumption of oil derivatives and emission of green house gases into the atmosphere [9]. It is today, more than ever, one of the world's most imperative and pressing necessities to find clean energy alternatives. One of these alternatives resides in the use of electric energy.

Electric motors have been for years used in the most diverse fields of applications. However, when it comes to apply these engines in airplanes or UAVs it is common to find that oil engines are usually the

primary choice. Some of the reasons have to do with the battery storage capacity. Recent developments in lightweight electric motors and battery design are making feasible the use of electric propulsion from storage batteries. In particular, the improvements in rechargeable battery performance has reduced the mass/energy ratio and when compared with other power-plant systems (4-cycle, 2-cycle, stepped piston, rotary) it generally outperforms them as Figure 1.4 shows. Unfortunately, a down side of the electric power plant system is the large volume of the batteries where sometimes, for a given energy storage, electric batteries occupy up to four times the volume of that of fossil fuels thus presenting a major limiting factor.

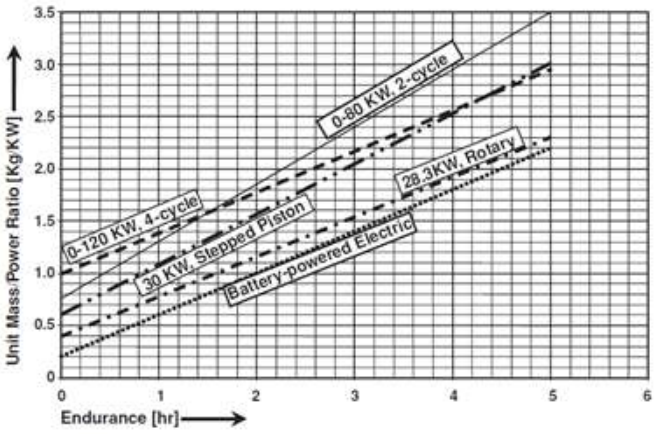

Figure 27.3 Power-plant performance

Figure 1.4: Power-plant performance. [10]

In the 1980s special attention was given to the development of UAVs propelled by means of solar power. A solar powered UAV could in theory fly indefinitely as long as it had an energy storage system to maintain its flight and other activities when no sufficient solar energy can be collected by its solar panels. To this day, solar photovoltaic cells are not very efficient, the consequence being that solar UAVs require large wing areas in order to accommodate the photovoltaic cells needed for charging electric batteries. Another characteristic of solar UAVs is that their structure must be lightly built to allow low powered takeoffs.

Project Sunrise, as seen in Figure 1.5, is believed to be the first solar powered radio controlled aircraft [11]. It had a wingspan of about 10 m, length of 4.36 m and a gross weight of 122 kg with batteries included. The solar cells were allocated, naturally, on the wing upper surface. This aircraft was envisioned as an unmanned sailplane that would have an operating altitude of about 22,250 m powered by a single Samarium-cobalt magnet electric motor. In order to have an aircraft as light as possible, its structure was built from balsa and maple woods. Due to their roughness the solar cells were only mounted on the aft two-thirds of the wing. Control was made via radio and the telemetry functions provided data on motor current, voltage and RPM, airspeed and two heading references from a sun compass for navigation. It first flew in 1974 in California on battery power and later the solar panels were mounted on the wing surface. This aircraft made 28 flights on solar power alone and although takeoffs were sluggish at first, once an altitude of a few hundred meters was achieved, the solar cells

cooled down and their efficiency increased thus electric power also increased and Sunrise was able to maintain a respectable climb rate. This project, a pioneer of its kind, proved that the concept of a solar UAV was possible and paved the road for future works.

Figure 1.5: Sunrise launching. [11]

A great example of what can be achieved using the power of solar energy was NASA's Pathfinder [12]. This was a solar-powered, lightweight (built primarily of composites, plastic and foam), remotely piloted flying wing used to demonstrate the use of solar power for high-altitude and long-endurance (HALE) flights. Solar arrays covered most of the upper wing surface and at high noon on a clear summer day its arrays provided up to 8,000 Watts of power. Because this aircraft does not have a rudder, roll and yaw control were accomplished by slowing down or speeding up the motors on the outboard sections of the wing. On July 7, 1997, it set an unofficial altitude record of approximately 21,800 m at Pacific Missile Range Facility, Kauai, Hawaii. Figure 1.6 shows one of NASA's Pathfinder flight tests.

Figure 1.6: NASA's Pathfinder. [12]

Another pioneering project that proved that the power of the sun can be successfully used to fly a plane for considerable periods of time is Airbus Space and Defense long endurance, solar powered, high altitude pseudo-satellite Zephyr [13]. As seen in Figure 1.7, it can carry a payload of about 2.5 kg, has a 22.5 m wingspan, a loaded weight of 53 kg and 2 Newcastle University custom PMSM powerplants.

Figure 1.7: Airbus Space and Defense Zephyr. [13]

This UAV as of July 2010 holds the world record for the longest duration flight of an unmanned air vehicle – two weeks of autonomous flight at an altitude of 21,500 m. Using solar power, state-of-the-art rechargeable lithium sulfur batteries and a carbon-fiber construction, it is expected that this UAV will be capable of hosting commercial communications and remote camera payloads for months at a time.

Finally, the Solar Impulse project aims to develop a piloted long range solar aircraft that eventually will circumnavigate the Earth thus making another fantastic example of the promising use of solar energy as a valid energy alternative in the aviation industry. Solar Impulse has developed two airplane prototypes HB-SIA and HB-SIB. Some of HB-SIB characteristics are its four high density energy electric batteries, 72 m wingspan, 23,000 kg and the use of more than 17,000 solar cells [14]. Some of this project's achievements and goals are the continental flight across the United States of America during 2013 and Earth's circumnavigation during a five month period beginning March 2015. Figure 1.8 shows Solar Impulse first prototype HB-SIA flying over San Francisco Golden Gate Bridge.

Figure 1.8: Solar Impulse HB-SIA flying over San Francisco Golden Gate Bridge. [15]

Chapter 2

Long Endurance Electric UAV

2.1 Project Description

Over the last decades there has been an amazing development in Unmanned Aircraft Systems (UAS). These comprise the control station which includes the facilities for the operators and the interfaces between personnel and machinery, the UAV, the communication system between the UAV and the control station and the support and maintenance equipment.

UAS despite being employed for the most part with military purposes can and should be used in a large number of civil applications such as fire detection and fire-fighting management, search and rescue missions, geographical and weather surveys, environmental research and air quality monitoring, digital mapping and planning, among others.

Unfortunately, civil applications of UAS did not evolve as fast. A few reasons are the prohibitive costs, the operational complexity and the typically large size of such systems. On the other hand, never the use of renewable energy has been more in demand by society, never the electric systems such as solar panels, motors and batteries have been more efficient nor the design tools, both numerical and experimental, have been so accessible.

These facts paved the way for this project ultimate objective: to design and build a low cost, small footprint electric UAV, capable of being deployed from short airfields, easy to build and maintain and flexible enough to perform different civilian surveillance missions.

A complete description of this project origins and long term goals is available in references [16] and [17].

2.2 Project Objectives

This project has two main goals:

- Develop an efficient and accurate multidisciplinary tool for designing UAVs, flexible enough to accommodate different configurations, sizes and propulsion systems;

- Access the feasibility of a small footprint, composite, low-cost, electric UAV mainly powered by high

efficiency solar panels, capable of being deployed from short airfields, easy to build and maintain, and flexible enough to perform different missions.

Among other features the UAV specifications will include:

- Long endurance flights accomplished by the use of an electric propulsion system and solar power collection cells. In particular using highly efficiency solar cells, high capacity/density batteries, efficient compact motors and appropriate long endurance aerodynamic design;

- Autonomous flight accomplished by equipping the vehicle with auto-pilot navigation systems such as inertial guidance systems and GPS;

- Obstacle avoidance accomplished by implementing obstacle avoidance algorithms that include detection, estimation and avoidance planning of obstacles;

- High-strength & low-weight structure accomplished by the use of composite materials, with fuselage/wing critical areas designed for good impact resistance on landing;

- Adaptability to multiple mission profiles accomplished by designing a sufficiently large payload range capability and developing upgradable modular avionics, to enable an easy software upload and/or hardware swap to meet the selected mission requirements.

If successful, the visible output of this project will be a small UAV, with a wing span of less than 5 m, capable of flying autonomously on solar power, with a manufacturing cost of less than a few thousand Euros, and with payload capability to perform different civil missions.

These objectives will be possible to accomplish by employing state-of-the-art analysis methods and out-of-the-shelf hardware, together with some innovations in terms of aircraft design and system integration solutions.

2.3 Mission and Performance Requirements

Table 2.1 shows a summary of the LEEUAV estimated performance with speeds and lift-to-drag ratio calculated at an altitude of 1,000 m, corresponding to the cruising altitude, and rate of climb and takeoff roll distance calculated at sea level. Furthermore, the LEEUAV will have a takeoff mass of 4.9 kg and be capable of flying for long periods of time while consuming as little energy as possible.

Table 2.1: LEEUAV estimated performance. [16]

Cruise speed	7.5 m/s
Maximum speed	21.1 m/s
Stall speed	6.1 m/s
Lift-to-drag ratio	20
Takeoff roll distance	8.1 m
Maximum rate of climb	2.2 m/s

The mission profile is summarized as follows:

1. Takeoff at sea level;
2. Climb up to 1,000 m altitude;

3. Fly for 8 hours in the equinox (21 March or 21 September) at an altitude of 1,000 m at low speed to be defined by system efficiency but greater than 6 m/s;

4. Descent;

5. Landing in the field at sea level.

Some requirements are a consequence of the mission objectives. The vehicle ought to be as light as possible in order to fly at maximum efficiency and to be able to takeoff and land in short runway airfields and eventually no airfields at all.

From the concept and design studies the flight speed in the cruise/loiter flight phase of 8 h is to be about 7.5 m/s (27 km/h).

2.4 LEEUAV Conceptual Design

The LEEUAV was designed to meet the performance parameters introduced in the previous section. To do so, a series of conceptual design studies were performed.

At the airfoil design level, a new airfoil was developed especially for this project using an in-house gradient based aerodynamic shape optimization tool and XFOIL [18] as the aerodynamic analysis tool. The design goal was to obtain an airfoil with minimum drag coefficient in the lift coefficient range of 0.6-1.5, subject to a maximum lift coefficient greater than 1.7, a relative thickness greater than 10% and a trailing edge thickness greater than 1 mm imposed to avoid damage during ground handling. Figure 2.1 shows the LEEUAV airfoil lift-to-drag ratio curves for $R_e(C_l^{3/2}) = 1.5 \times 10^5$ and $R_e(C_l^{3/2}) = 2 \times 10^5$.

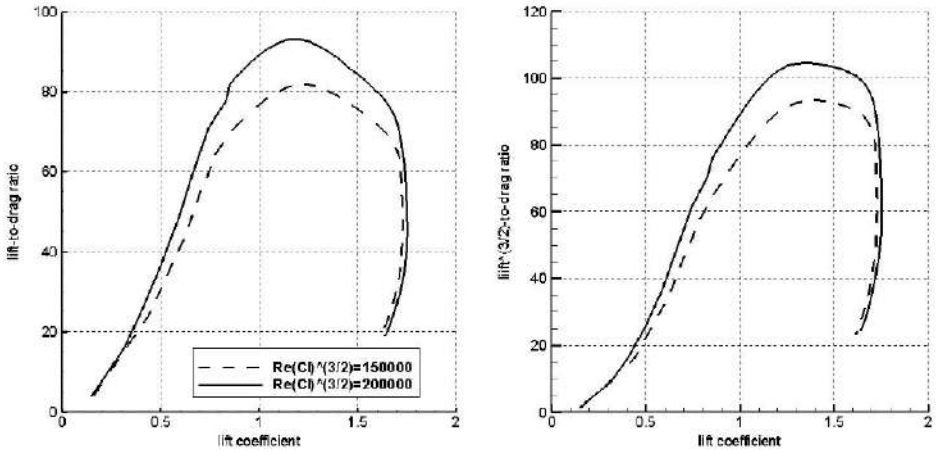

Figure 2.1: Airfoil design lift-to-drag ratio and lift$^{3/2}$-to-drag ratio. [16]

The correct sizing of the aircraft is very important in order to produce a high performance design. The design was based on parametric studies developed with in-house algorithms whose primary design parameters were the wing span and the wing mean chord. Other non constrained parameters were the cruise lift coefficient, center of gravity position, airfoil, motor and propeller. The design process was based on the mission profile and performance requirements. Lift and drag coefficients were computed

considering trimmed conditions. The propulsion model matches the propeller and the motor for a given speed and throttle setting and provides power, thrust, and power consumption. A solar energy model is also included to allow the calculation of the incident energy on the solar panels to be computed along the time of the flight. The weight model implements scales on the airframe component weights based on known wingspan, wing mean chord, airfoil relative thickness, load factor, maximum weight and fuselage size.

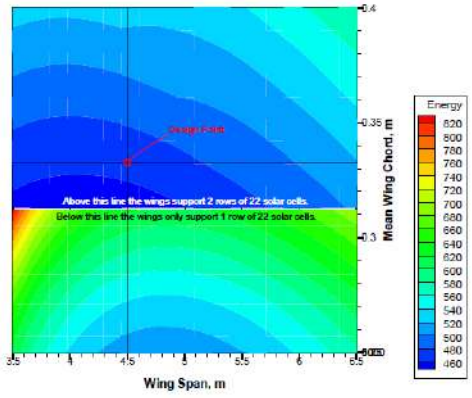

(a) Energy for flight.

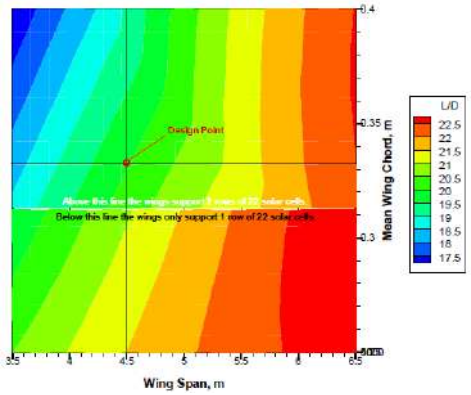

(b) Lift-to-drag ratio.

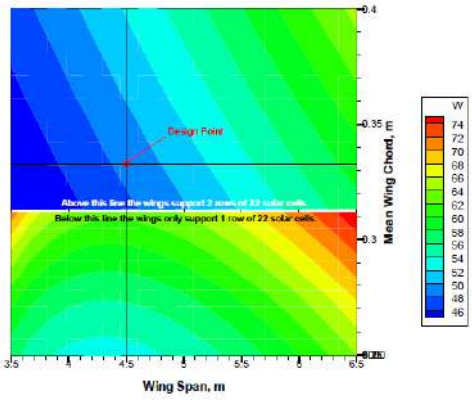

(c) Takeoff weight.

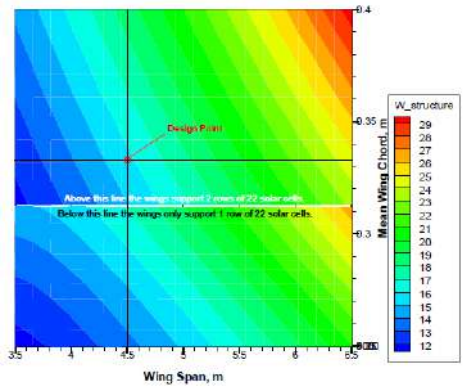

(d) Structure weight.

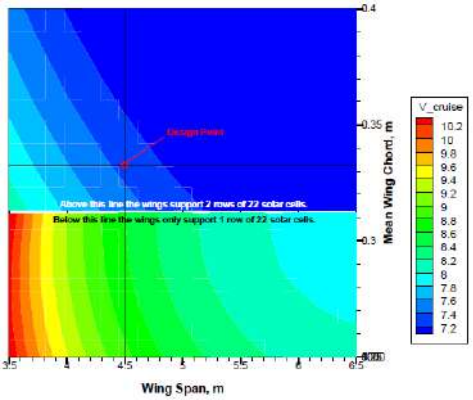

(e) Cruise speed at 1000m.

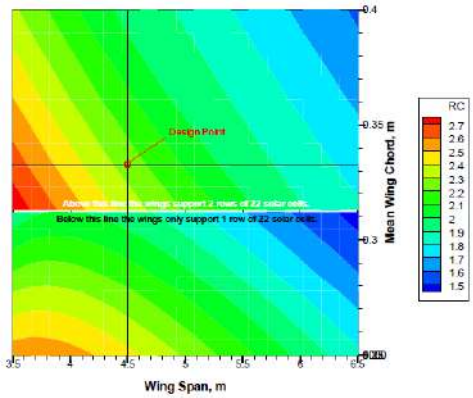

(f) Maximum rate of climb at sea level.

Figure 2.2: LEEUAV conceptual design studies. [16]

Figure 2.2 shows a summary of the LEEUAV conceptual design studies for the energy usage during the flight, lift-to-drag ratio, takeoff weight, structure weight, cruise speed and maximum rate of climb at

sea level. There is a change in the energy requirements for flight with a wing chord of about 0.31 m due to the fact that below this value the wing would only take one row of solar cells. This situation would have its impact on the takeoff weight since in that case there would be the need to add batteries to guarantee sufficient energy during takeoff, climb and cruise flight phases.

The design point was selected for a wing span of 4.5 m and a wing mean chord of 0.33 m. These values give the wing a large area to allocate the required solar cells on its upper surface. The wing can as well be divided into four parts capable of being disassembled for transportation purposes.

The LEEUAV dimensions and views are present on Table 2.2 and Figure 2.3.

Table 2.2: LEEUAV dimensions. [16]

Wingspan	4.5 m
Length	2.37 m
Wing root chord	0.350 m
Wing tip chord	0.25 m
Wing planform area	1.5 m^2
Wing aspect ratio	13.5
Tailplan chord	0.213 m
Tailplan span	0.85 m
Tailplan planform area	0.181 m^2
Empennage root chord	0.258 m
Empennage tip chord	0.364 m
Empennage planform area	0.077 m^2

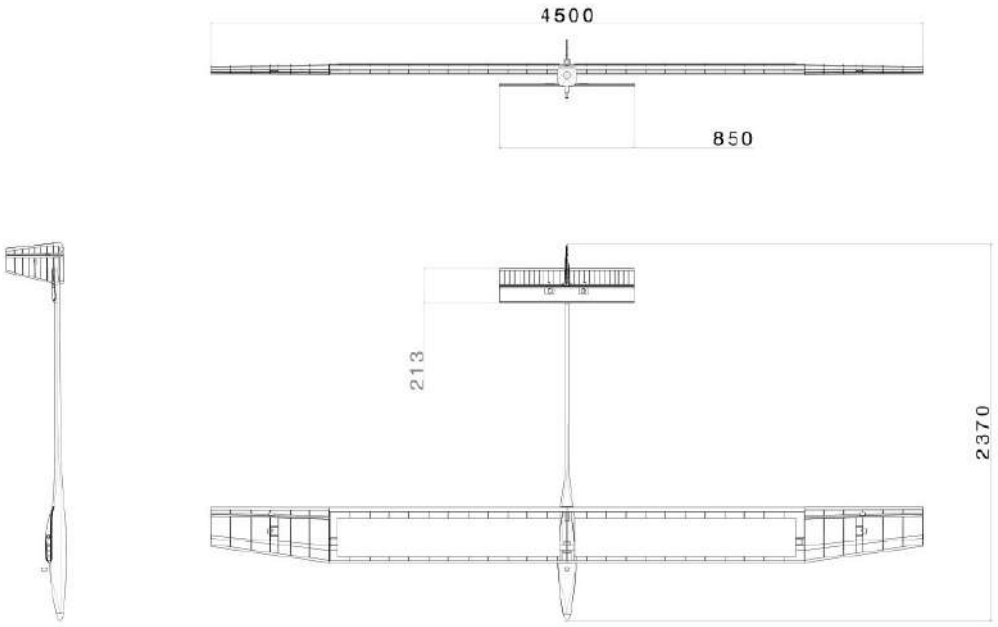

Figure 2.3: LEEUAV views and dimensions in mm. [16]

2.5 Hybrid Propulsion System

The LEEUAV is expected to fly during the summer months and to do so its propulsive system, which was developed as a Master Thesis in Instituto Superior Técnico [19], will rely on the solar radiation captured by its 44 mono-crystalline Silicon Photovoltaic (PV) cells and one 11.1 V and 8400 mAh Lithium-Polymer (Li-Po) battery. Furthermore, the propulsive system will be equipped with a Morningstar SunKeeper Solar Charge Controller (SCC), a Turnigy Super Brain Electronic Speed Controller (ESC) and an NTM PROP Drive Series electric motor and propeller. Figure 2.4 shows the LEEUAV propulsive system scheme.

Figure 2.4: LEEUAV hybrid propulsive system scheme. [19]

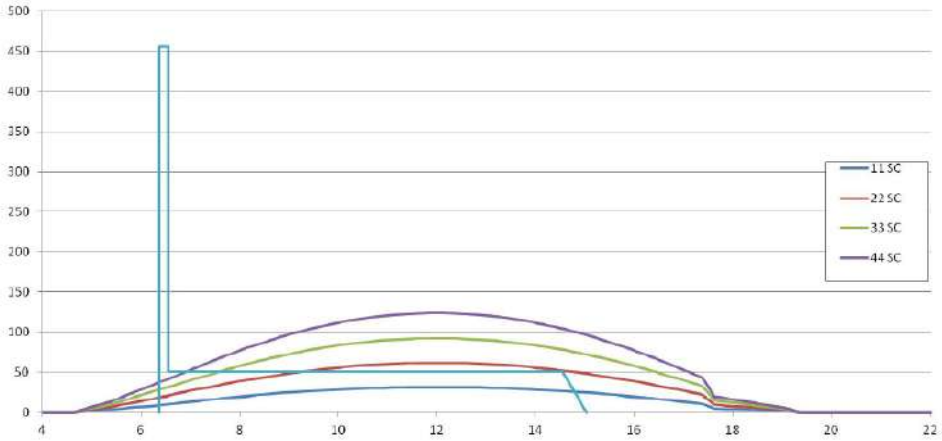

Figure 2.5: Radiation power available versus time of the day during July. [19]

Figure 2.5 shows the power different solar panel configurations can generate during a typical July day, and the energy needed for different flight phases. In that figure, represented in turquoise, is the required energy for the LEEUAV different flight phases. The LEEUAV will have 44 solar cells which is the configuration that produces the most excessive power. During the takeoff and climb phases the solar panels do not provide the sufficient amount of energy for the airplane to achieve cruise altitudes. As such, battery power is required in those phases. During flight, the battery is eventually completely recharged allowing the airplane to cruise the skies during the expected 8 hours. When there is no sufficient sunlight or when flying during the night, the LEEUAV will rely on its battery to provide energy to its electric motor and systems. The range and endurance in those situations are calculated respectively by [20]:

$$Range = R = E^* \eta_{total} \frac{C_L}{C_D} \frac{m_{batt}}{m} \frac{1}{g} \tag{2.1}$$

where E* is the battery specific energy, η_{total} is the propulsive system total efficiency, $\frac{C_L}{C_D}$ is the aircraft lift-to-drag ratio, $\frac{m_{batt}}{m}$ is the ratio between the battery and aircraft total mass and g is the gravitational acceleration.

$$Endurance = \frac{Range}{Velocity} \leftrightarrow E = \frac{R}{U_{cruise}} \tag{2.2}$$

For convenience, the relevant data for the range and endurance computation for the cruise flight phase is presented in Tables 2.3 and 2.4.

Table 2.3: LEEUAV propulsion system efficiency. [19]

Battery efficiency	100 %
Wires efficiency	100 %
ESC efficiency	95 %
Motor efficiency	89 %
Propeller efficiency	85 %
Total efficiency	71.87 %

Table 2.4: LEEUAV battery characteristics. [19]

Capacity	8.4 Ah
Voltage	11.1 V
Energy	335664 Ws
Mass	0.641 kg
Specific energy	523656.8 Ws/kg

Using Eqs. (2.1) and (2.2), Tables 2.3 and 2.4, and the computed lift and drag coefficients from Chapter 6, the LEEUAV range is determined to be approximately 70 km and its endurance 3 hours.

Chapter 3

LEEUAV Parametric Design

3.1 CAD Software Selection

This chapter addresses the CAD software selection process and scripting design methodologies when developing the building blocks that ultimately were employed in the LEEUAV design and are expected to be used in the design of other UAV configurations keeping in mind the project long term objectives.

As such, this chapter first addresses all the CAD software packages considered as plausible tools in the LEEUAV design phase. Afterwards, a description of the LEEUAV building processes will take place and finally a description of the proper object and mesh file formats will be addressed.

This thesis takes part in the design, evaluation and optimization processes of several UAV configurations, and as a consequence it is of the utmost importance to use a CAD software that allows the easy and swift modeling and assembly of general UAV configurations. The goal when dealing with the geometric design and assembly of different UAV components is to render this phase as user independent as possible. As such, a CAD software is to be selected only if there is the possibility of making the use of scripts where the user defines in a particular text file the UAV key dimension parameters and one or several scripts collect that data and interact with the CAD program in order to build, assemble and export the UAV components.

A total of six commonly used and well known CAD programs in the engineering and scientific fields were tested. Those programs were the Dassault Systèmes SolidWorks and CATIA, Siemens NX, NASA OpenVSP, Salome and FreeCAD. The first three programs are commercial programs and the last three are open source.

Usually, commercial products tend to be better equipped with specialized tools as opposed to their open source counter-parts that generally have just enough functions to satisfy the needs of students and hobbyists.

One of those commercial software packages is SolidWorks [21]. This is a powerful CAD tool that is employed in several industry fields like the automotive and transportation, aerospace and defense [22], engineering and construction, among many other areas.

Another well known commercial CAD program is CATIA [23]. This software, like many others of its

kind, has a broad range of applications and in the most diverse industries. One of its many costumers and of tremendous importance in the aviation and aerospace industries is Airbus.

Siemens has a role of its own when CAD programs are considered. Its NX software [24] can be used in tasks like design, simulation and manufacturing of diverse tools and for the most transverse industries. Several leading edge and fast pacing companies make good use of this tool like Airbus Defense and Space, Lockheed Martin Aeronautics and Pratt & Whitney.

Of course there are as well other software packages made specially for the aerospace industry such as NASA OpenVSP which is an open source parametric geometry tool [25]. OpenVSP allows its users to create three-dimensional models of an aircraft using common engineering parameters which afterwards can be processed into formats suitable for engineering analyses.

SALOME [26] which is also an open-source software, provides a generic platform for pre- and post-processing numeric simulations. This tool can be used for the generation of CAD models, their preparation for numerical calculations and post-processing.

Finally, FreeCAD [27] is yet another open source parametric three-dimensional modeler that can be used not only by home users or hobbyists but also by experienced CAD users and programmers. This program allows its users to easily design or modify the developed models, is completely modular, multiplatform, supports Python and reads and writes many open file formats like STEP, IGES, STL, among many others.

All of the above CAD software packages, and many others that for the sake of space management were not mentioned in this section, have their positive and negative aspects and depending on a specific project and financial goals have their use, or not, justified. Usually, specifically developed aerospace commercial CAD programs are more complete and offer a broader range of functionalities that an open-source program might not. However, one needs to keep in mind that having specifically developed CAD programs will naturally have its toll in licensing costs.

The selection process had several key aspects that had to be met, although not all of them were of critical importance. One of these requirements was the possibility of using both Windows and Linux as the working operating systems. All programs support Windows but only FreeCAD and Salome support Linux. All other programs naturally support a Unix or Unix-like operating system or Mac OS. Another requisite was the support of scripting so that the interaction between software and designer is as reduced as possible. From all of the above, only FreeCAD naturally supports the use of Python scripts and most of its functions are accessible trough Python. Since the generated geometries will be sent into a CFD software for aerodynamic analysis, a critical aspect will undoubtedly be the generation of sane files that are supported by that software. The tested programs seemed to be able to generate files that are easily imported into the CFD software and neither produced critical errors, although depending on the program and UAV component, minor geometry corrections had to be performed prior to generating surface and volume meshes.

Among all the software packages only one met all the mentioned criteria and that program was FreeCAD. This software is truly customizable and allows the parametric modeling of complex three-dimensional geometries and is aimed at general engineering, architecture and product design works.

It is open source, most of its functions are accessible using Python scripts and if not, the users can develop new ones that suit their needs. Finally, it can read and write open file formats such as STEP, IGES and STL which are easily imported with the selected CFD software.

3.2 Design Procedures

The design of a general UAV configuration, in this case the LEEUAV, can be divided into five main parts: the loading of the FreeCAD different modules required to run the program several functions and the definition of specifically developed algorithms, the statement of the geometric parameters or variables that are required for the complete definition of the UAV components, the test of those variables in order to ensure that those components relative dimensions are valid and make sense (e.g. it is undesirable to have the wing mean chord bigger than the entire fuselage), the building and assembly of the different components and finally the export of the generated mesh and object files later to be used by the CFD software. The design fluxogram is illustrated in Figure 3.1.

Prior to anything else, the designer is required to provide the geometric parameter inputs that will later define the airplane geometry. These variables relate to the LEEUAV different components such as the wing, fuselage, tail and nose. The complete set of the LEEUAV variables and their respective values is available in Appendix A, section A.1.

Before using FreeCAD for the virtual building and assembling each component, a series of exhaustive tests are performed regarding the geometric parameters dimensions and their relation to each other as part of a single entity - the UAV. These tests are performed with the objective of checking whether the variables have appropriate dimensions and their values fall between specific ranges so that cases such as the wing root chord being bigger than the fuselage length do not occur. If any such cases arise, the user will be presented with as many error messages as discrepancies are detected and the process is interrupted.

After completing the input test phase without any errors, the building of the LEEUAV different components takes place. The design script was developed in order to divide the baseline airplane into four different but dependent geometries. Different because the LEEUAV is composed by its wing, fuselage, tail and nose, and dependent because each component is placed and oriented with respect to each other. The order in which the airframe components are built is the following: wing, fuselage, tail and nose. The reason behind designing the wing prior to anything else is related with the next chapter which addresses the aerodynamic analysis of airfoils. As for the other components, the fuselage was built after the wing because its sections are related to the wing leading and trailing edges, the tail is built after the fuselage because the horizontal and vertical stabilizers are placed at specific fuselage sections and finally the nose is placed at the other end of the fuselage.

After building each component, they are assembled into a single entity so that the subtraction between the LEEUAV and the computational control volume used in the aerodynamic analyses can be easily performed. Afterwards a series of control volumes, which are simple parallelepipedic objects that englobe different airplane parts are generated as well.

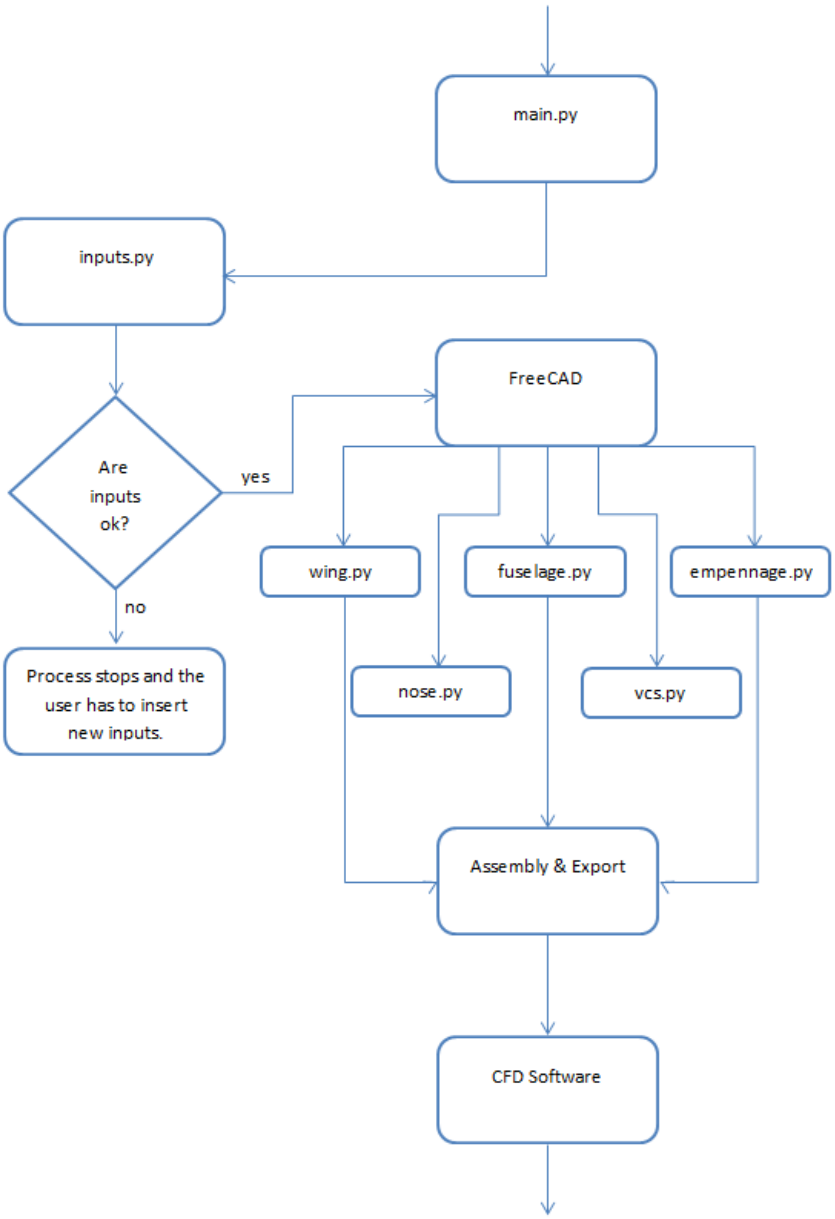

Figure 3.1: Design script fluxogram.

Finally, the required mesh and object files are exported in order to be used by the CFD software.

In the following subsections, the design methodologies and every scripting choice will be addressed. Every dimension was based on the original LEEUAV design.

3.2.1 Wing Design

The LEEUAV building process starts with the left half wing. The reason behind building the left half wing is related to the CAD software axis orientation and the reason behind building only half a wing is due to the aerodynamic analyses that will be performed. This is because most of the LEEUAV flight profile will be at cruise conditions. Later on, when other flight profiles and maneuvers might be of interest, the entire UAV is easily built simply by executing a mirror function in the UAV plane of symmetry.

As it was envisioned, the wing is defined by four sections. At each section an airfoil is specified by providing its coordinates in a specific file, together with five additional variables which are the airfoil chord, wing sweep, twist and dihedral angles, and each section spanwise location. Another set of variables is employed in the definition of the wing first section position and these are its airfoil leading edge coordinates. All other sections are placed with respect to the first one.

Looking at Figure 3.2, each section placement is defined in the following way: section 0 (S0) is located at the fuselage plane of symmetry and its airfoil chord is 350 mm; section 1 (S1) is located at a distance from S0 equal to the mid width of the fuselage at that section, measured at the wing leading edge and its airfoil chord is the same as in the previous section; sections 2 (S2) is located 1,400 mm apart from section S0 and its airfoil chord remains the same; section 3 (S3) is located 850 mm apart from the previous section and its airfoil chord is 252 mm. The entire wing has -5º of incidence when considering a positive rotation along the Oz axis, and -1º dihedral angle when considering a positive rotation along the Ox axis. Between sections S2 and S3 the wing has a sweep angle of 5.5º in the direction of the tail.

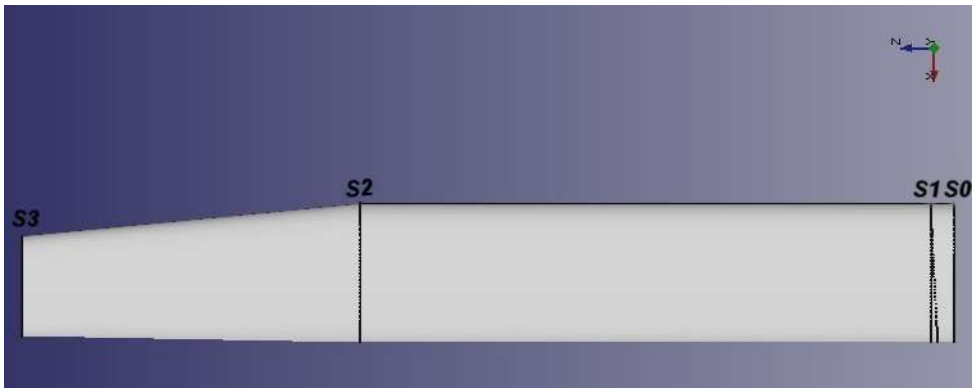

Figure 3.2: Wing section locations.

The wing building process starts by importing an airfoil for each of the four wing sections. A single airfoil was used in the entire wing, specifically designed for this project using an in-house gradient based aerodynamic shape optimization tool.

FreeCAD has its own functions for importing files containing airfoil coordinates. However, through the course of this thesis, it became apparent that those functions were not up to the challenge. The reasons behind this statement are related to scaling, lofting and fusion operations. More often than not, when connecting two wing sections through loft operations and later when fusing the entire wing, the fusing operation would generate an invalid geometry. This was found to be a consequence of the FreeCAD native scaling function which was being employed to assign each wing section its specific airfoil chord. As such, an airfoil importing script was developed to cope with the aforementioned issues.

After importing each airfoil, these are placed in their respective coordinates and assigned their respective angles. Once more, because there was no easy way of defining the different wing section angles, another script was developed to convert and assign each wing section their angles along a specific axis. Afterwards, every two contiguous sections are connected through lofting operations and later all wing segments are connected into a single entity after fusing them all together.

Due to the fact that the LEEUAV has a high wing configuration and due to the fuselage design, if the wing is built simply by importing airfoils and assigning each section their respective chord, location and angles, there would be a gap between the wing root region and the top fuselage surfaces. A solution to this problem was obtained when developing the airfoil importing script. With this script, when importing any airfoil coordinates from a text file, two lists are generated containing the upper and lower airfoil coordinates. If the user decides to use this function, an extra line is created connecting the airfoil points defining its leading and trailing edges. This way another airfoil is created so that its shape fits perfectly inside the aforementioned gap. Figure 3.3 shows a comparison between the two configurations, where the viewer is facing the fuselage from the positive Oz axis and the black surfaces represent the wing upper and lower surfaces. While Figure 3.3 a) evidences the gap between the wing and fuselage, Figure 3.3 b) shows the wing root gap solution.

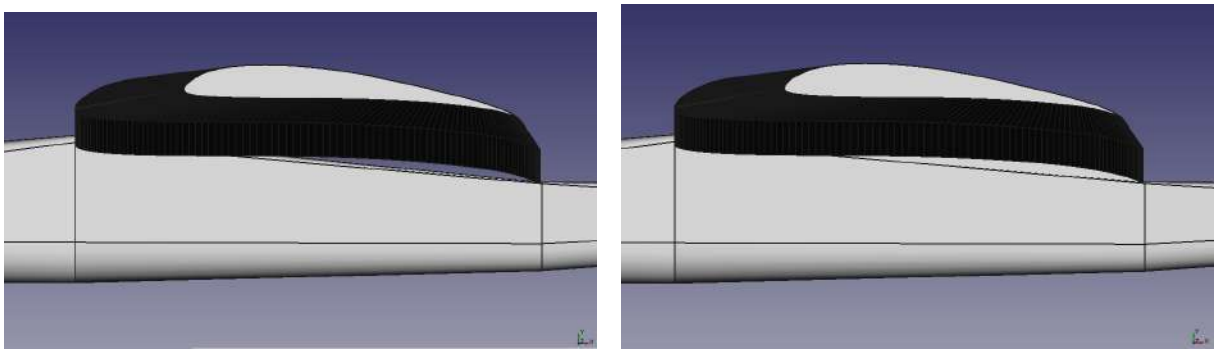

(a) Gap between wing and fuselage.

(b) No gap between wing and fuselage.

Figure 3.3: Wing root design.

3.2.2 Fuselage Design

After building and assembling the wing, the fuselage is built section by section, loft by loft, until the final geometry is fused together into a single entity.

The fuselage was built using a total of ten different cross-sections along its longitudinal axis to guarantee a smooth transition between sections as seen in Figure 3.4. Sections S0 through S5 correspond to the regions between the nose and tail boom which comprise the avionics bay compartment, sections S5 and S6 define the tail boom, and sections S6 through S9 correspond to the fuselage sections that manage the interface between the boom itself and the horizontal and vertical stabilizers. Circular section S0 will allow a smooth transition between the fuselage and nose given its axi-symmetric geometry. When dividing the fuselage in its different sections, sections S2 and S3 are defined as the wing root location for the leading and trailing edges, respectively. Not every section was defined in the same way. While fuselage sections S1, S2, S3, S4, S7, S8 and S9 are of rectangular shape with arcs instead of vertices, fuselage sections S0, S5 and S6 are of circular shape. Figure 3.5 offers a general representation of each type of cross-section and their respective control variables. Different sections have different variables. All rectangular sections are defined by a set of four variables that determine a specific section shape such as its width (*lu_i*), lateral height (*h_i*) and upper and lower arc radii (*r1_i* and *r2_i*, respectively). All

circular sections are defined by their radius (*Ri*). Furthermore, there are three additional variables that determine the distance between any two neighboring cross-sections (*dist_fuse_si_sj*), their vertical offset relative to the fuselage longitudinal axis origin (*delta_yi*) and a final one created to ensure that all rectangular cross-sections are centered with the longitudinal plane of symmetry (*delta lu_i*). The fuselage length is 2,170 mm.

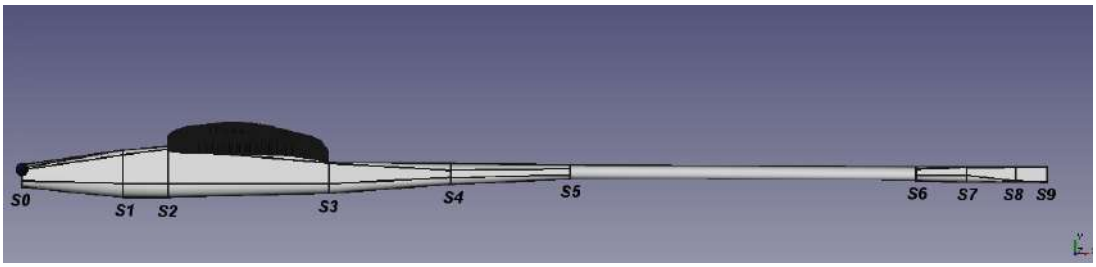

Figure 3.4: Fuselage sections.

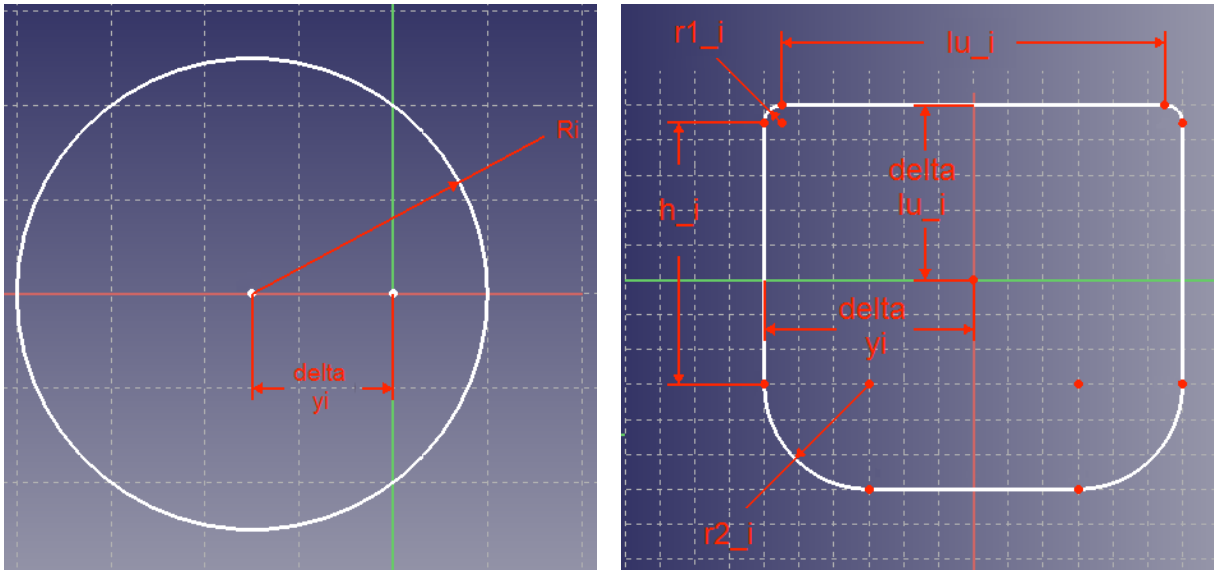

(a) Fuselage circular cross-section.

(b) Fuselage rectangular cross-section.

Figure 3.5: Fuselage cross section shapes.

After building and repositioning every cross-section in their respective places, several loft operations are performed in order to connect every fuselage cross-section. After completing the lofts, every fuselage segment is fused together so that the fuselage becomes a single entity.

3.2.3 Tail Design

The LEEUAV tail has a characteristic inverted cruciform shape with the horizontal stabilizer leading edge being placed ahead of the vertical stabilizer. Much of the tail building process is identical to that of the wing. The tail has a total of five sections which are defined by the location of different airfoils. Every airfoil is imported using the aforementioned developed script and they are located with their respective chords and angles at their proper coordinates. However, unlike the wing, in this case, a symmetrical NACA0010 airfoil is used in every tail section.

The horizontal stabilizer has two sections, one located at the fuselage symmetry plane (section S0) and the other 425 mm apart from it (section S1). Its leading and trailing edges are located at fuselage sections S6 and S8. This tail component has four degrees of incidence when considering a positive rotation along the Oz axis and a constant chord length of 214 mm.

The vertical stabilizer has three sections, all of them located at the UAV plane of symmetry. Section S0 is positioned on top of the tail boom and its leading edge is located at fuselage section S7. The other two sections (S1 and S2) are located above and bellow section S0, respectively. This component has a total vertical length of 365 mm where 65 mm correspond to the distance between sections S0 and S2 and 300 mm correspond to the distance between sections S0 and S1. Section S0 and S2 have chord lengths of 250 mm, section S1 has a chord length of 150 mm.

Figure 3.6 gives a better understanding of the tail sections, configuration and relative dimensions.

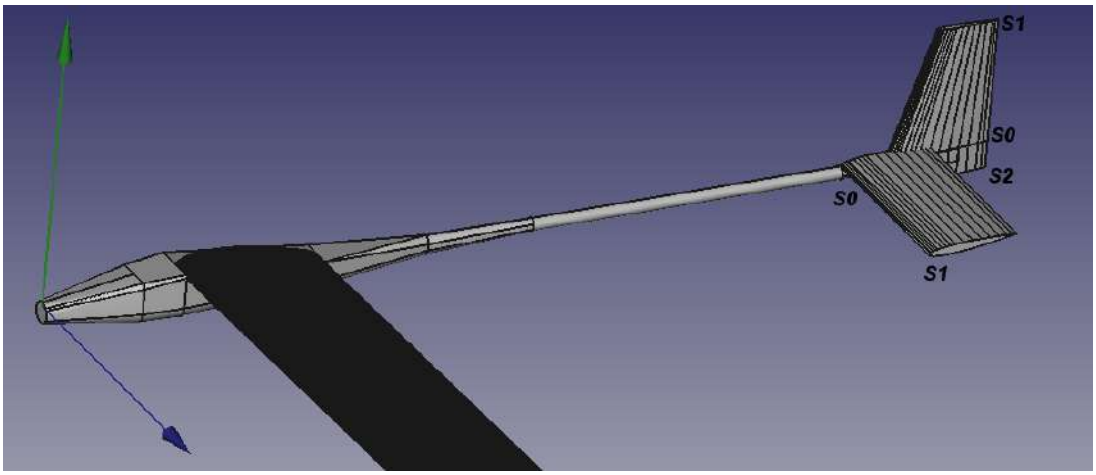

Figure 3.6: LEEUAV tail arrangement.

3.2.4 Nose Design

The LEEUAV nose will have a spinner, propeller and electric motor. However, designing such geometries would add a lot of unnecessary complexity, possibly cause serious mesh problems when generating the surface and volume meshes in the CFD software and probably, the flow going around that geometry would promote the generation of unsteady phenomena that would require the use of unsteady schemes in the aerodynamic simulations. To avoid adding unnecessary complexity to an already complex case, a simple ellipsoid geometry was produced to emulate the nose geometry.

The nose has an axi-symmetric shape and its base is located at fuselage section S0. The nose generation process, unlike any other LEEUAV component, is based on a face revolution around its longitudinal axis. First of all, three line segments and an arc are placed in their proper place and connected together with the adequate inter-relations. Line segment *ln* defines the nose length and is equal to 48 mm. Line segments *rn1* and *rn2* define the nose radii used in its revolution around line segment *ln* and measure 25 mm and 4 mm, respectively. Figure 3.7 shows the different nose geometry inputs. A view of the nose geometry is illustrated in Figure 3.8.

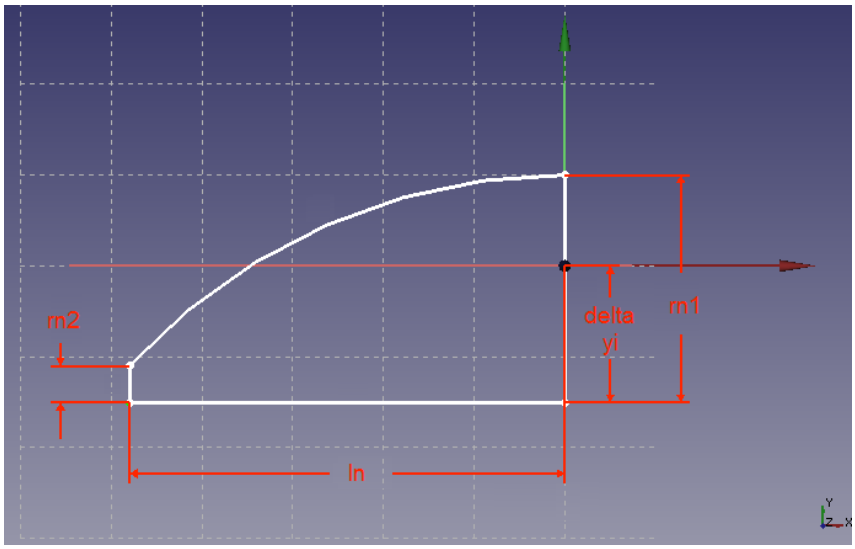

Figure 3.7: Nose variables.

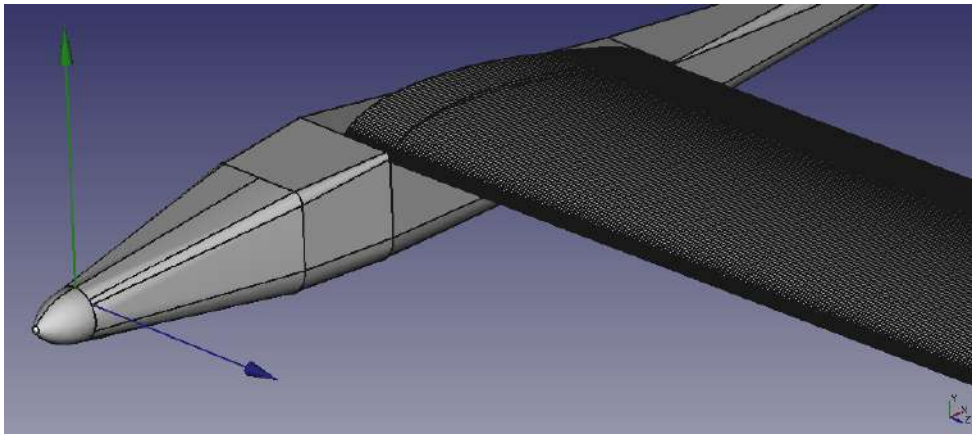

Figure 3.8: Nose in the airplane.

3.2.5 Control Volumes Definition and Generation

The control volumes employed in the aerodynamic simulations and used to refine specific areas of the LEEUAV meshes were developed using the design script. Although they could be developed using the CFD software, designing the different control volumes using the CAD software proved to be a better strategy. Because every control volume is defined with the objective of later refining specific mesh regions, their dimensions depend on those of the LEEUAV.

A total of five parallelepipedic control volumes were defined: two control volumes that cover the entire wing, where one goes from wing section S0 to wing section S2 and another from wing section S2 until wing section S3 (control volumes CV1 and CV2); another control volume that englobes the LEEUAV geometry comprised between the nose and half the tail boom (control volume CV3); a fourth control volume that englobes the entire UAV (control volume CV4) and a fifth that serves as the aerodynamic simulation control volume (control volume CV5).

Control volumes CV1 and CV2 apart from having the length of their respective wing segments, were defined to have a width of 1.5 times the wing root chord and an height of one half the wing root chord,

as seen in Figure 3.9. Control volume CV3 height and length are equal to the wing root chord and its width is five times that value, as seen in Figure 3.10. Control volume CV4 length is equal to one and a half times the wing semi-span, its width is equal to three times the fuselage length and its height is equal to three times the vertical stabilizer height, as seen in Figure 3.11. Finally, control volume CV5 length is equal to six times the semi-wingspan, its width equals seventy times the wing root chord and its height measures sixty times the wing root chord, as seen in Figure 3.12.

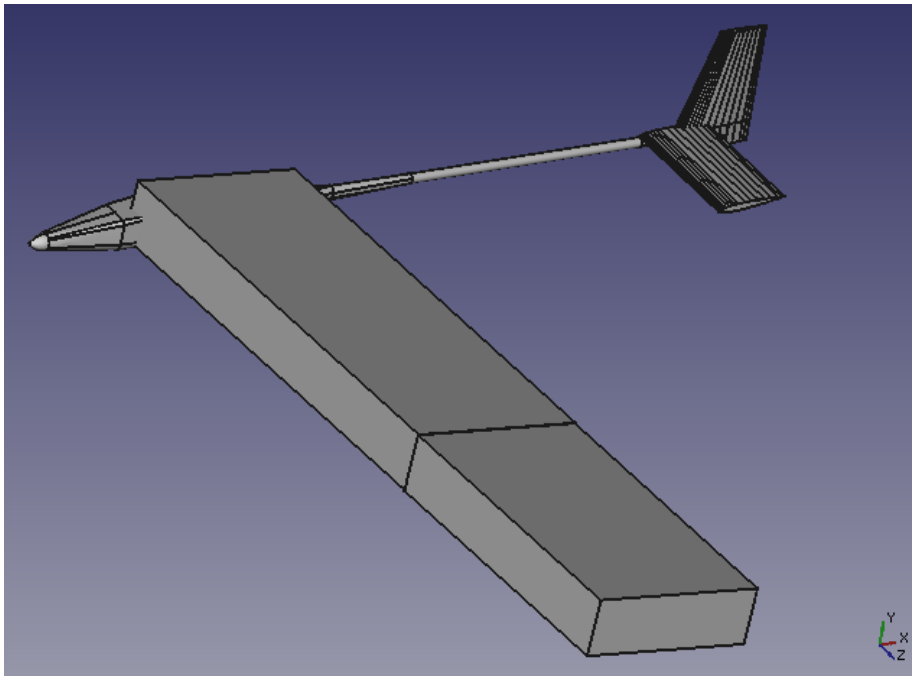

Figure 3.9: Control volumes CV1 and CV2.

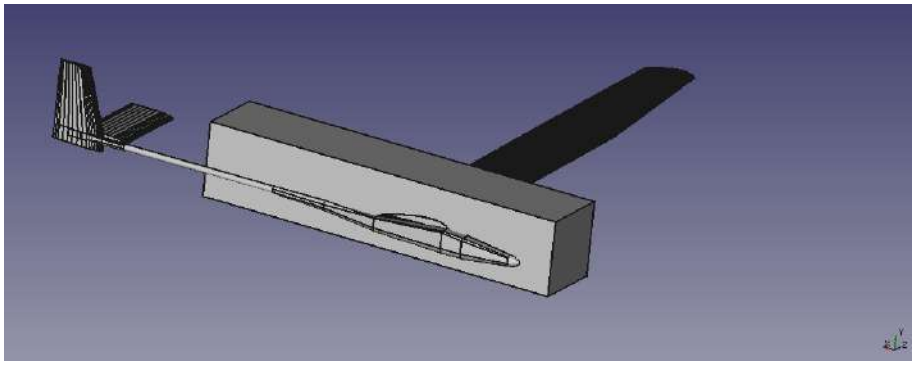

Figure 3.10: Control volume CV3.

3.3 Object and Mesh Files Export Considerations

After building every LEEUAV component and fusing them all together, these are exported in three different files formats: STEP, IGES and STL files. All file types are easily imported into the CFD software although depending on its version, certain file types are better suited for different tasks. Throughout

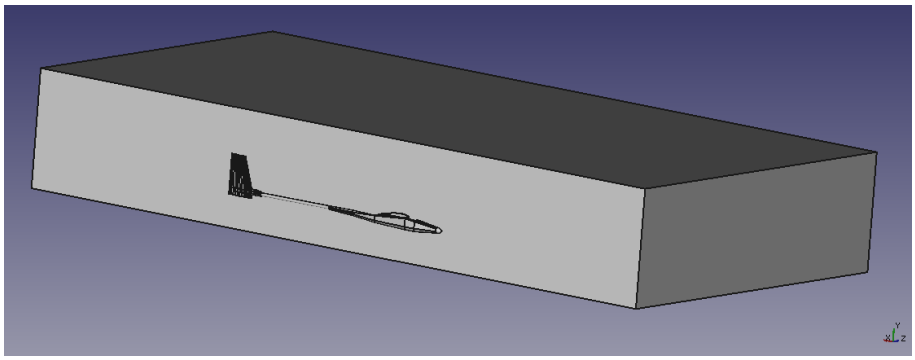

Figure 3.11: Control volume CV4.

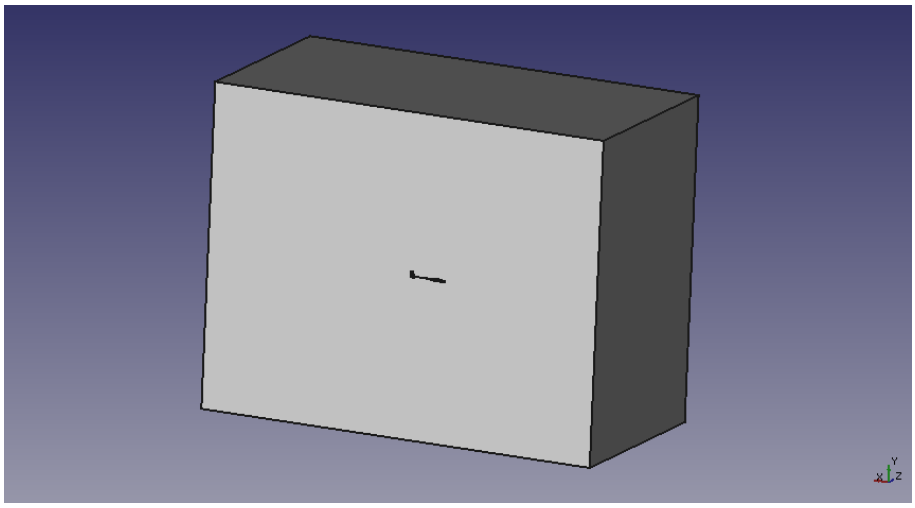

Figure 3.12: Control volume CV5.

this thesis, STEP file type objects proved to be very useful and allowed the user to import and generate surface and volume meshes without encountering critical errors.

3.4 General Design Conclusions

From all of the tested CAD software packages, FreeCAD stood out from the remainder for its multiple operative systems capabilities, for not involving licensing costs and last but not least, for supporting Python scripting and generating sane geometry file formats that are easily imported and dealt with by the CFD software.

Although most of the native FreeCAD functions worked extremely well and could be quickly employed in the design of the LEEUAV, at times there were minor issues that had to be addressed. Examples of such occurrences were the native scale function that although scaling the required wing section airfoils, later would not allow different wing segments to be fused together, and the nose definition where two revolutions had to be performed in opposite ways in order to fuse that geometry together. Apart from those issues, there was another one related to the fuselage section definition. Sometimes, when defining a random section and after assigning each line segment or arc its dimensional value, FreeCAD would raise a warning stating the sketch was over-constrained and would not generate valid fuselage segments

after the lofting operations. The causes behind this warning are related to the program intrinsic functions which are not yet fully compatible with an all scripting design methodology. A solution to this problem is the repositioning of a random sketch component, for example a line segment. Afterwards the warning message is replaced by a message stating the sketch is fully constrained.

Another issue was the fusing operation between all the LEEUAV components and later the subtraction with the global control volume. Because it was not possible to fuse the nose with the rest of the LEEUAV geometry, the nose, the LEEUAV without the nose and the computational control volume had to be sent to the CFD software in order to, through boolean operations, add and subtract those geometries from one another. This was found to work rather well and as such is the recommended approach to such problems.

Even though the necessity of changing or generating new functions or scripts were at times required, a conclusion was reached that using FreeCAD together with the developed Python scripts presents more advantages than disadvantages when designing the LEEUAV or similar aircraft geometries.

Chapter 4

Mesh, Turbulence and Transition Models Studies

This chapter addresses the aerodynamic software packages used in this thesis. To understand which aerodynamic models are best suited for the flow regime under study, a series of comparisons were established between experimental results and those obtained using a specific CFD software. These studies involved the comparison of aerodynamic data from flows around several airfoils at Reynolds numbers similar to the LEEUAV operating conditions. Furthermore, extensive mesh studies were performed. All these studies provided a better understanding of what aerodynamic models and mesh configurations were to be used in the remainder CFD simulations.

4.1 CFD Software Selection

In order to develop accurate engineering projects when a specific airplane configuration is to be analyzed in terms of its flying qualities, an engineer might use the classical theories of aerodynamics in a pre-design phase to get a grasp of the forces, moments and general flow physics the airplane will experience. However, in most cases that person will at a later phase perform CFD simulations and usually wind-tunnel tests for validating and experimenting with new configurations.

There are a number of software packages one can use and like it was the case with the CAD design tools, these are both open source and commercial software packages.

A well known CFD program is ANSYS Fluent [28] widely known for its physics modeling capabilities used in flow, turbulence, heat transfer and reactions for diverse industrial applications such as flow over an aircraft wing, combustion in a furnace, blood flow and many other applications. It is known to produce very accurate results although it might be very time consuming since it requires a considerable knowledge about the software and physics models.

CD-adapco Star-CCM+ [29] is another commercial package that is regarded as one of the best CFD solutions available on the market. This software is capable of managing multi-physics and complex geometries. With its powerful meshing algorithms and physics models this is without a doubt one of the

most powerful and user-friendly software packages.

The Swedish Defense Research Agency developed its unstructured CFD solver named Edge [30]. This software supports Reynolds Averaged Navier-Stokes equations (RANS), Large Eddy Simulation (LES) and Detached Eddy Simulation (DES) models and allows its users the use of turbulence models ranging from algebraic models to state-of-the-art two-equation models.

DLR-TAU [31] is a software package capable of solving RANS and Euler equations on hybrid grids. This software has powerful mesh generation algorithms that make good use of tetrahedral, prismatic, pyramidal and hexahedral meshes in complex geometries. Steady and unsteady flow solutions for incompressible and compressible flows can be computed with great efficiencies.

OpenFOAM [32] is an open source CFD software package which has a large user base in the engineering and scientific areas from commercial and academic organizations. This software capabilities include simulations ranging from complex fluid flows involving chemical reactions, turbulence and heat transfer to solid dynamics and electromagnetics. It includes tools for meshing and pre- and post-processing.

All of the programs mentioned above have similar features and are employed by major companies in the most diverse and demanding engineering and scientific fields. Because Star-CCM+ is available at the Laboratory of Fluid Simulation in Energy and Fluids (LASEF) and because it is widely known as one of the best flow simulation and mesh generators in the scientific and engineering fields, it is this software that will be employed in all the in-depth aerodynamic analyses. This software does all the pre-processing, including mesh generation, processing and post-processing.

Apart from Star-CCM+, XFOIL [18] was also employed in cases where no wind-tunnel data was available. XFOIL uses an e^N method for transition prediction and is widely regarded as one of the best tools for aerodynamic studies on airfoils.

4.2 Aerodynamic Validation Data Source

Prior to setting-up the aerodynamic simulations on the entire LEEUAV, there was the need to understand what aerodynamic models and mesh configurations should be used. This way, several mesh and aerodynamic model studies were carried out on simpler geometries.

As such, and because there was no wind-tunnel information regarding the LEEUAV airfoil, there was the need to find well studied airfoils subject to air flows having Reynolds numbers similar to those of the LEEUAV during its cruise flight phase. The objective was to compare the aerodynamic data from Star-CCM+ to that obtained with wind-tunnel experiments and while doing so, to understand what aerodynamic models and mesh characteristics should be employed first at the airfoil level, later at the wing level and finally at the airplane level.

After thorough research, two airfoils that fit this project objectives were selected. All data concerning these airfoils was obtained from the University of Illinois at Urbana-Champaign (UIUC) Aerodynamics Research Laboratory in its low-turbulence subsonic wind-tunnel. The reason to choose these airfoils in particular is related to their shape which resemble the LEEUAV airfoil and to the Reynolds numbers at

which these were tested. Details concerning the test facilities, test set-up and wind-tunnel results can be further checked in reference [33]. Figure 4.1 provides a better understanding of the two airfoils used in the mesh and aerodynamic analyses.

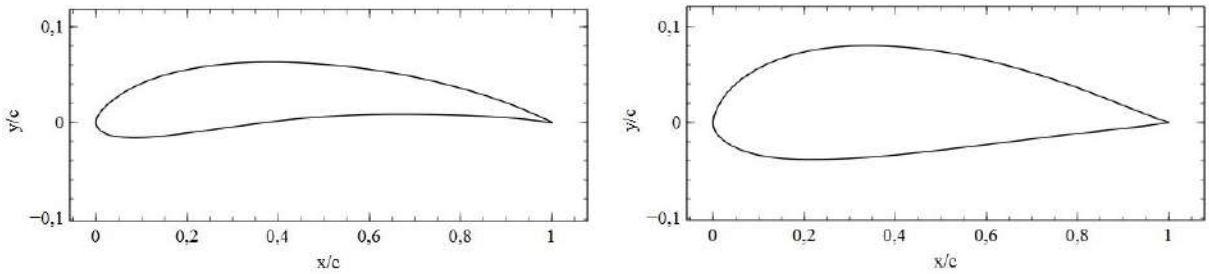

(a) MA409. (b) CAL1215J.

Figure 4.1: Validation airfoil shapes.

Both airfoils have a chord length of 0.30 m, airfoil MA409 has a maximum thickness of 6%c at x=33%c and maximum camber of 2%c at x=39%c whereas airfoil CAL1215J has 11%c maximum thickness at x=24%c and the same value for the maximum camber as the previous airfoil but at x=43%c.

4.3 STAR-CCM+ Aerodynamic Models

To understand the flow physics around these airfoils at the project Reynolds number, not only one has to generate good quality meshes that are adequate to the geometries under study, one needs as well to determine which aerodynamic models best suit this study. In the subsequent sections, a review of two turbulence and transition models is presented.

4.3.1 $k-\omega$ SST Turbulence Model

The $k-\omega$ SST turbulence model [34] is based on two transport equations that provide the computation of the turbulent kinetic energy κ and the specific turbulent dissipation rate ω. Menter published in 1994 this two-equation eddy-viscosity turbulence model that combines the best of previously developed turbulence models $k-\epsilon$ and $k-\omega$. This model uses the $k-\omega$ turbulence model in the inner regions of the boundary layer and the standard $k-\epsilon$ model in the outer regions and in free-shear flows.

This turbulence model transport equations are the following:

$$\frac{D\rho\kappa}{Dt} = \tau_{ij}\frac{\partial U_i}{\partial x_j} - \beta^*\rho\omega\kappa + \frac{\partial}{\partial x_j}[(\mu + \sigma_\kappa\mu_t)\frac{\partial\kappa}{\partial x_j}] \tag{4.1}$$

$$\frac{D\rho\omega}{Dt} = \frac{\gamma}{\nu_t}\tau_{ij}\frac{\partial U_i}{\partial x_j} - \beta\rho\omega^2 + \frac{\partial}{\partial x_j}[(\mu + \sigma_\omega\mu_t)\frac{\partial\omega}{\partial x_j}] + 2(1-F_1)\rho\sigma_{\omega 2}\frac{1}{\omega}\frac{\partial\kappa}{\partial x_j}\frac{\partial\omega}{\partial x_j} \tag{4.2}$$

where ρ is the density, t is the time variable, τ_{ij} is the wall shear stress tensor, U is the velocity vector, x is the position vector, β, β^*, σ_κ, σ_ω and $\sigma_{\omega 2}$ are constants, μ is the molecular viscosity coefficient, μ_t is the eddy viscosity, γ is the intermittency factor, ν_t is the kinematic eddy viscosity and F_1 is a blending

function that goes from zero away from the surface to one close to the surface. This function is also used to blend the constants of the standard Wilcox $k-\omega$ model [35] with those of the transformed $k-\epsilon$ model [36].

The constants ϕ of the new model are calculated from constants ϕ_1 and ϕ_2 as:

$$\phi = F_1\phi_1 + (1 - F_1)\phi_2, \tag{4.3}$$

where the constants of set ϕ_1 are from the Wilcox $k-\omega$ model and the constants of set ϕ_2 are from the Jones-Launder $k-\epsilon$ model.

4.3.2 $\gamma - Re_\theta$ Transition Model

With the objective of predicting where natural and bypass transition occurs, the $\gamma - Re_\theta$ transition model was used together with the $k-\omega$ SST turbulence model. This is a correlation-based transition model which is built strictly on local variables and is compatible with unstructured grids and parallel execution. This model is based on the transport equations for intermittency and transition onset criterion in terms of momentum-thickness Reynolds number, which can be used to trigger transition locally and capture the non-local influence of the turbulence intensity, respectively. Further information regarding this transition model development and validation tests is available in references [37] and [38], respectively.

The intermittency function is coupled with the $k-\omega$ SST turbulence model and is used to turn on the production term of the turbulent kinetic energy downstream of the transition point. The formulation of the intermittency equation has also been extended to account for the rapid onset of transition caused by separation of the laminar boundary layer.

The transport equation for the intermittency is as follows

$$\frac{\partial(\rho\gamma)}{\partial t} + \frac{\partial \rho U_j \gamma}{\partial x_j} = P_{\gamma 1} - E_{\gamma 1} + P_{\gamma 2} - E_{\gamma 2} + \frac{\partial}{\partial x_j}[(\mu + \frac{\mu_t}{\sigma_\gamma})\frac{\partial \gamma}{\partial x_j}], \tag{4.4}$$

with the transition sources defined as

$$P_{\gamma 1} = F_{length} c_{a1} \rho S[\gamma F_{onset}]^{c_\alpha}; E_{\gamma 1} = c_{e1} P_{\gamma 1} \gamma \tag{4.5}$$

where S is the strain rate magnitude. F_{length} is an empirical correlation that controls the length of the transition region. The destruction/relaminarization sources are defined as

$$P_{\gamma 2} = c_{a2} \rho \Omega \gamma F_{turb}; E_{\gamma 2} = c_{e2} P_{\gamma 2} \gamma \tag{4.6}$$

Ω is the vorticity magnitude. These terms ensure that the intermittency remains zero in the laminar boundary layer and also enables the model to predict relaminarization. F_{turb} is used to disable the destruction/relaminarization sources outside of a laminar boundary layer or in the viscous sublayer. σ_γ, c_{a1}, c_{a2}, c_α, c_{e1} and c_{e2} are constants. In the aforementioned references, the authors state that for good transition predictions to be performed, the wall y+ factor should be approximately one.

4.3.3 Spalart-Allmaras Turbulence Model

The Spalart-Allmaras (SA) turbulence model [39] is a one equation model developed for aerodynamic applications where a sole transport equation is solved for the turbulent viscosity. The objective in developing this model was to mitigate the incompleteness of algebraic and one-equation models based on the turbulent kinetic energy while at the same time being, from a computational point of view, simpler than two-equation models. Depending on the type of simulation the authors propose different transport equations and reference conditions.

This model transport equation is defined as

$$\frac{D\tilde{\nu}}{Dt} = c_{b1}[1 - f_{t2}]\tilde{S}\tilde{\nu} + \frac{1}{\sigma}[\nabla(\nu + \tilde{\nu})\nabla\tilde{\nu}] + \frac{c_{b2}}{\sigma}(\nabla\tilde{\nu})^2 - [c_{w1}f_w - \frac{c_{b1}}{k^2}f_{t2}](\frac{\tilde{\nu}}{d})^2 + f_{t1}\Delta U^2 \tag{4.7}$$

where $\tilde{\nu}$ is the kinematic eddy viscosity factor which is related to the eddy viscosity term ν, $\tilde{S}$ is the production term, f_w is the destruction function and f_{t1} and f_{t2} are transition functions being the remainder terms calibrating constants.

4.3.4 Turbulence Suppression Model

The Turbulence Transition (TS) model allows the user to mimic the effects of boundary layer transition by suppressing the turbulent kinetic energy generation in specific field regions. It is hardly a transition model since it requires the user's input of where transition is expected to occur.

4.4 Mesh Generation & Characteristics

After several thorough studies on mesh quality where parameters like the number of prismatic layers, its thickness and stretch factor, surface growth rate and volumetric control volumes were analyzed, a final compromise was met. This was obtained using a prismatic layer around the entire airfoils and polyhedral mesh in the remainder computational domain. Apart from the global control volume, a total of three smaller control volumes were employed in the mesh generation process. Two of these were located at the airfoils leading and trailing edges (cv1 and cv2, respectively) and another one englobes the entire airfoil and the two smaller control volumes (cv3).

For the $\gamma - Re_\theta$ transition model to accurately predict transition, the mesh has to be defined in such a way that the wall y+ factor should be approximately one. Furthermore, for the pressure field to be accurately computed around the airfoils, in the regions where the boundary layer will develop, the mesh ought to be accordingly refined in order to capture in detail the flow behavior at those locations. Also, a good transition between the refined areas and the remainder of the control volume should be ensured.

When generating the surface and volume meshes around both airfoils, the same parameters were employed in order to have as little mesh interference as possible in the final results. Furthermore, and because the simulated angles of attack are not extremely low or high, only one mesh for each airfoil was used in all aerodynamic simulations.

Figure 4.2 is relative to profile MA409 and provides a better understanding of the mesh characteristics. As it is clearly seen, the prismatic layer does not present the same thickness over the entire airfoil. The leading and trailing edges represent mesh areas that if not accurately refined can negatively influence the flow characteristics over the entire airfoil. That is why the prismatic layer thickness in those areas is smaller and its cells also have smaller widths. This way, the airfoils leading edge curvature is smoother while the boundary layer still develops inside the prismatic layer. Although not present in the figure, the prismatic layer thickness at the trailing edge is reduced due to that mesh transition from the airfoil upper to lower surface. If the prismatic layer had a significant thickness in that area, its transition from the upper to the lower surface would be quite abrupt thus jeopardizing the mesh quality.

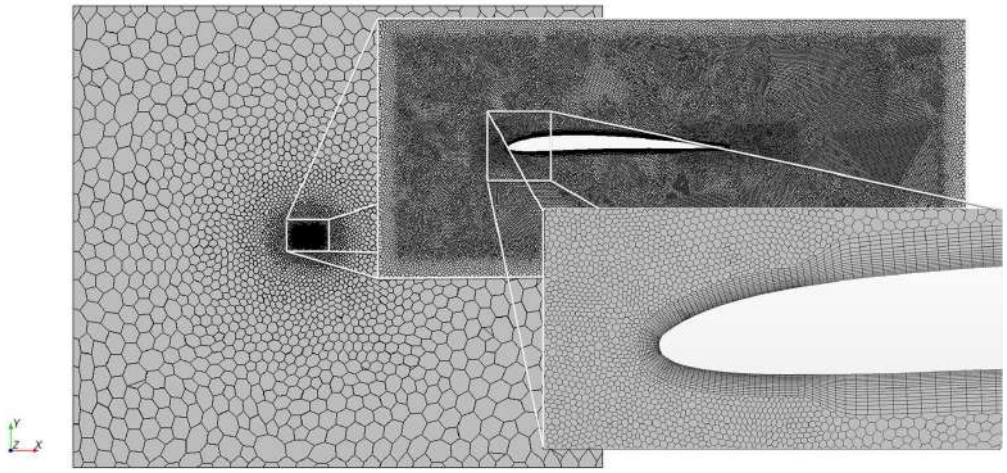

Figure 4.2: MA409 volume mesh.

The global control volume was built having the airfoil dimensions in consideration and as such, its height and width measure respectively 60 and 70 chord lengths. As for control volumes cv1 and cv2, they have 0.16c as their height and 0.23c and 0.5c as their width, respectively. Control volume cv3 has 1c and 2.5c as its height and width.

The global control volume has a base size of 1 m and surface growth rate factor of 1.1. The smaller control volumes have 15 prismatic layers and a prismatic layer stretching factor of 1.1 around the airfoils. The control volumes located around the leading and trailing edges both have cell custom sizes of 0.00125 m and prismatic layer thicknesses of 0.0040 m. The control volume that englobes the previous two, has a cell custom size of 0.0025 m and prismatic layers thickness of 0.008 m. Both meshes have approximately 70,000 cells.

4.5 CFD Simulations

The LEEUAV was designed to fly at Reynolds numbers regimes of about 1.6×10^5 and Mach numbers of approximately 0.02, corresponding air properties at 1,000 m above sea level (ν=1.5810^{-5} m^{2}s^{-1}, a=336.4 m/s), airplane mean chord (assumed the wing root chord) of 0.35 m and design cruising speed of 7.53 m/s.

$$Re = \frac{U\bar{c}}{\nu} = \frac{0.35 \times 7.53}{1.5810^{-5}} \simeq 1.6 \times 10^5 \tag{4.8}$$

$$Ma = \frac{U}{a} = \frac{7.53}{336.4} = 0.02 \tag{4.9}$$

The physics models used in Star-CCM+ had the following baseline definitions: gas (air at constant density), segregated flow, two dimensional, turbulent and low y+ wall treatment. Since there are no compressibility effects at this Mach number one can assume there are no changes in air density, two dimensional models are self explanatory given the nature of the simulations and turbulent models are employed since natural transition effects are expected to occur somewhere along the airfoil surfaces at these Reynolds numbers.

Both airfoils were subjected to two Reynolds flow regimes and these were $Re_1 = 2 \times 10^5$ and $Re_2 = 3 \times 10^5$.

Throughout the study of the $k - \omega$ SST turbulence model and when conducting analyses using steady state models, the residuals did not converge because vortex shedding was very active which in turn produced grave oscillations in the pressure field about the airfoil. When switching from steady to implicit unsteady models, the vortex shedding is properly resolved so that the residuals converged. The vortex shedding is a local phenomena with minor global relevance in terms of the integral quantities. On the other hand, when using the SA turbulence model, the vortex shedding phenomena was not captured which in turn allowed to achieve convergence with steady state models. This rapid residual convergence is a well known trait and more often than not is one of the reasons for employing this model.

Great care was given in the mesh generation processes so that the wall y+ factor is approximately one.

In all aerodynamic simulations, because no calibration data was available, the inlet turbulence intensity was assumed to be 0.1% and the turbulent length scale was assumed as 10% of the airfoil thickness. These values are in line with what is usually applied in simulations of this nature.

A comparison between all simulations and the UIUC wind-tunnel data presented in Figure 4.3 shows all available data on airfoil MA409 at both Reynolds numbers and turbulence models. Both turbulence models at either Reynolds number can accurately determine the lift coefficient with errors below 8%. However, that is not the case when comparing the drag coefficient data. In the majority of the simulations, the SA turbulence model fails to provide acceptable results with errors being below 50% while the $k - \omega$ SST turbulence model used together with the $\gamma - Re_\theta$ transition model provides the same data with errors below 15%. Similar results were obtained for airfoil CAL1215J, as seen in Figure A.1 in Appendix A.2.

An interesting fact is that the SA turbulence model drag predictions exhibits, in general, lower discrepancies as the angle of attack increases. A consequence of using this turbulence model without any transition model is that the flow is turbulent starting almost at the airfoil leading edge. When testing an airfoil using a wind-tunnel, as the angle of attack increases so does the velocity peak that also moves closer to the airfoil leading edge. As the velocity peak increases so does the adverse pressure gradient

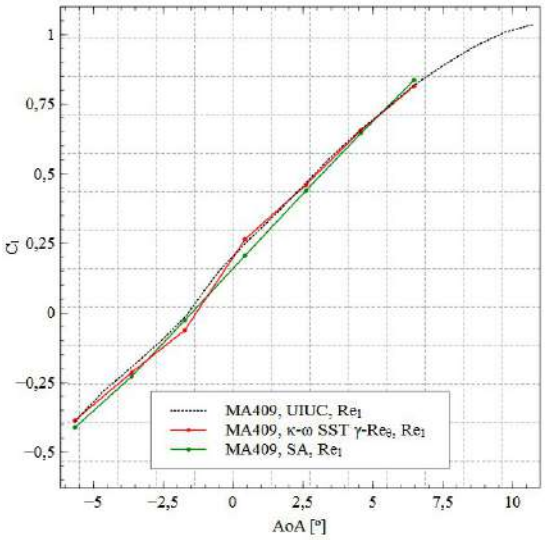

(a) C_l versus AoA, Re_1.

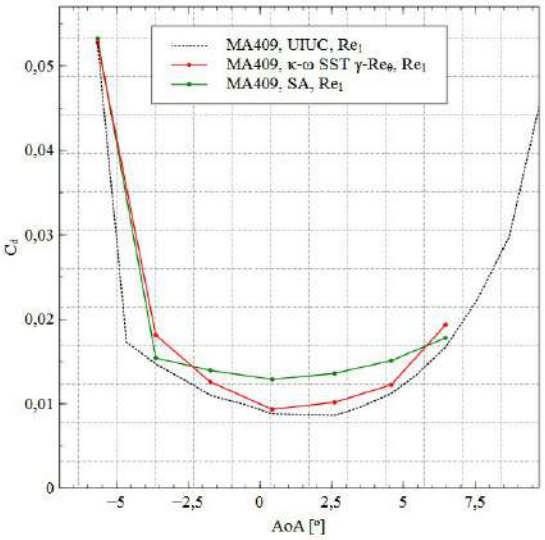

(b) C_d versus AoA, Re_1.

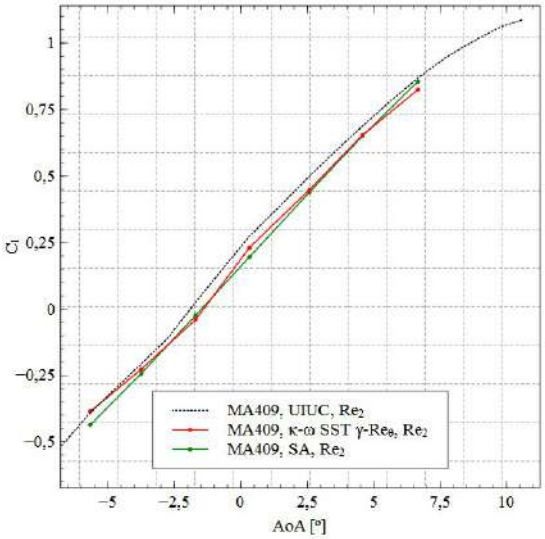

(c) C_l versus AoA, Re_2.

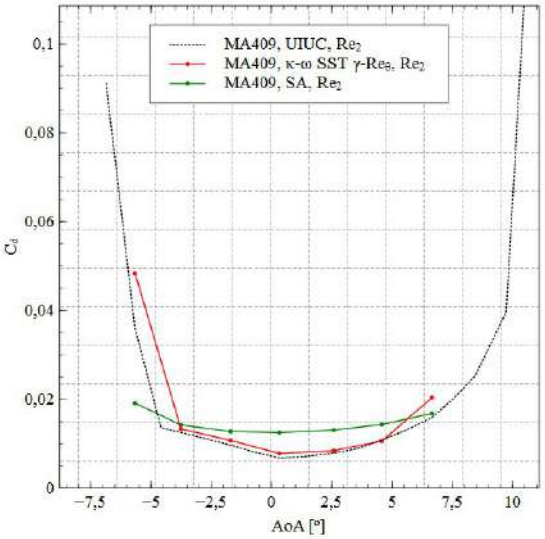

(d) C_d versus AoA, Re_2.

Figure 4.3: MA409 lift and drag coefficients at Re_1 and Re_2.

that follows and it is at that region that the flow under the right conditions becomes turbulent over the airfoil surface. In terms of the drag coefficient what this means is that the turbulent drag contribution increases as the angle of attack increases since natural transition occurs closer to the leading edge. This way, the increasing SA turbulence model drag prediction accuracy at higher angles of attack might just be the result of the model's turbulent kinetic energy generation in areas where there should not be any generation at all coupled with the airfoil upper surface transition location gradually moving in the direction of the leading edge.

There is no transition model available in Star-CCM+ that when used together with this turbulence model can determine or improve natural transition prediction. There is however the Turbulence Suppression model that one can use together with the SA turbulence model. With the TS model, the user states in what computational regions turbulence is to be suppressed. This approach provides good results when the transition location is known a priori like in such cases when the flow passes through

a boundary layer trip. While using this model, although it is not documented, the obtained C_l and C_d values are much closer to the UIUC data. However, as good as it may be, it is hardly a transition model and can not be used to predict natural transition.

When using the $k-\omega$ SST turbulence model without any transition model, the data obtained in that way is very similar to the SA model results. This suggests that if acceptable results are to be expected and if natural transition is to be determined, one ought to use the $\gamma - Re_\theta$ transition model.

Figures 4.4, 4.5, 4.6 and 4.7 are relative of airfoil MA409 at an angle of attack of 4.57º and Reynolds number Re_1. The first two images were obtained using the $k-\omega$ SST turbulence model used with the $\gamma - Re_\theta$ transition model and the remainder using the SA turbulence model. Those figures show the consequences of using both turbulence models when computing the flow physics around that airfoil in particular. Similar results were obtained for airfoil CAL1215J.

When observing turbulent flows at a specific instant of time and location, the flow can exhibit an intermittent behavior where sometimes it is turbulent and sometimes it is non-turbulent. In those cases the turbulent flow is separated from the non-turbulent flow by a sharp and irregular interface. The intermittency factor plays a central role in determining where the flow is laminar or turbulent since it contains the probability to encounter turbulent flow at a specific instant and location.

At low Reynolds numbers, and when the free-stream turbulence intensity is low, the flow starts as laminar and after the velocity peak, when the adverse pressure gradient is strongest the laminar boundary layer separates. If the conditions are adequate, the flow then experiences laminar-turbulent transition and the boundary layer re-attaches forming a laminar separation bubble (LSB). This LSB can be categorized as a long or short bubble depending on the airfoil surface percentage that it covers. If it is a short bubble the impact it has on the airfoil performance is almost irrelevant. However, if the bubble has a significant length, then it can significantly change the airfoil shape causing among other things the reduction of lift and increase in drag.

Figure 4.4 presents the intermittency factor of airfoil MA409 at an angle of attack of 4.57º. Close to the airfoil surface and prior to the LSB, the intermittency factor is zero. However, after the bubble there is a local maximum where the intermittency factor equals one. That region corresponds to the turbulent kinetic energy peak in Figure 4.5 where the flow becomes turbulent after the boundary layer re-attachment. The bubble shown in these two figures has a maximum thickness of 0.5%c and its length equals 30%c. Although the bubble thickness is very small when compared to the airfoil chord, the same can not be said about its length.

In all simulations using the $k-\omega$ SST turbulence model together with the $\gamma - Re_\theta$ transition model, the laminar flow that first develops on the airfoil surface grows unstable until at a certain point a laminar separation bubble forms as a consequence of the laminar boundary layer separation and later re-attachment now as a turbulent boundary layer.

Figure 4.6 was obtained using the SA turbulence model. As it was previously mentioned, this model does not determine where natural transition occurs and as such both the upper and lower airfoil fluid regions evidence turbulent kinetic energy generation. Unlike the two previous figures, at this angle of attack there is no LSB on the airfoil upper surface.

When activating the TS model in the field regions where there is no turbulent kinetic energy generation according to the $k-\omega$ SST and $\gamma - Re_\theta$ simulations, the presence of a laminar separation bubble still does not exist and turbulent kinetic energy generation gradients are the opposite of the other model. It seems turbulent kinetic energy generation occurs after the flow leaves the airfoil and does not dissipate as it would be expected to occur.

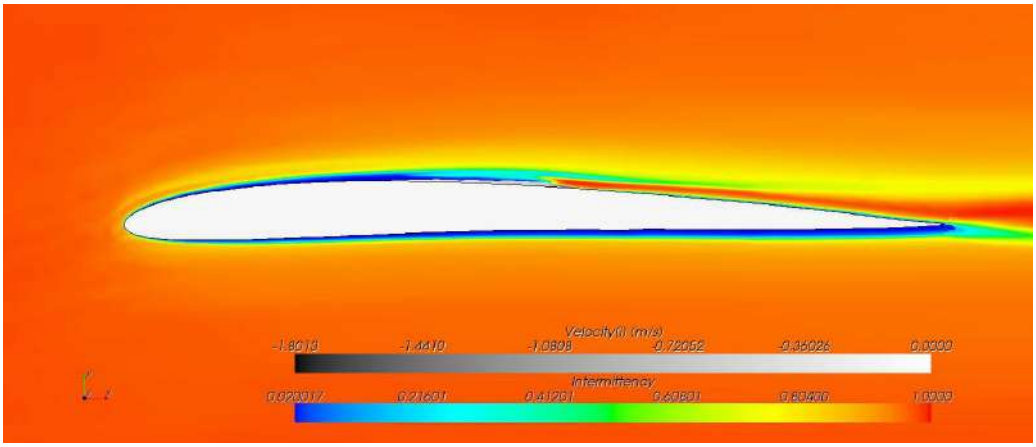

Figure 4.4: MA409, intermittency factor, $k-\omega$ SST, $\gamma - Re_\theta$, Re_1, AoA=4.57º.

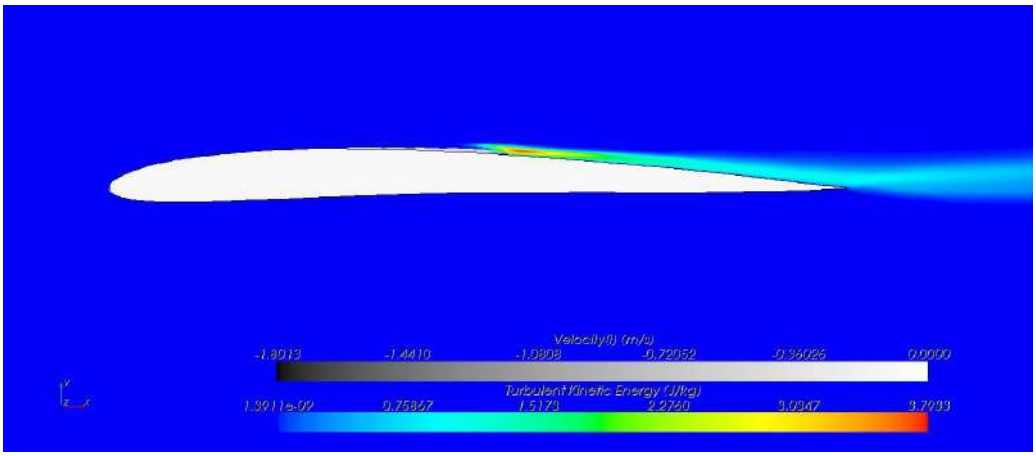

Figure 4.5: MA409, turbulent kinetic energy (J/kg), $k-\omega$ SST, $\gamma - Re_\theta$, AoA=4.57º, Re_1.

Table 4.1: Free-stream turbulence intensity studies on the laminar separation bubble behavior, MA409, AoA=4.57º, Re_1.

Ti (%)	dx (m)	dy (m)	x_{tr} (%c)
0.1	0.0950	0.00154	0.158
1.5	0.0906	0.00154	0.156
2.0	0.0910	0.00154	0.153
5.0	0.0870	0.00117	0.153

Figure 4.8 shows the transition curves of airfoil MA409 for both Reynolds numbers and compares the natural transition location predictions between XFOIL and the $k-\omega$ SST turbulence model used together with the $\gamma - Re_\theta$ transition model. Generally, and although the results are very similar, XFOIL

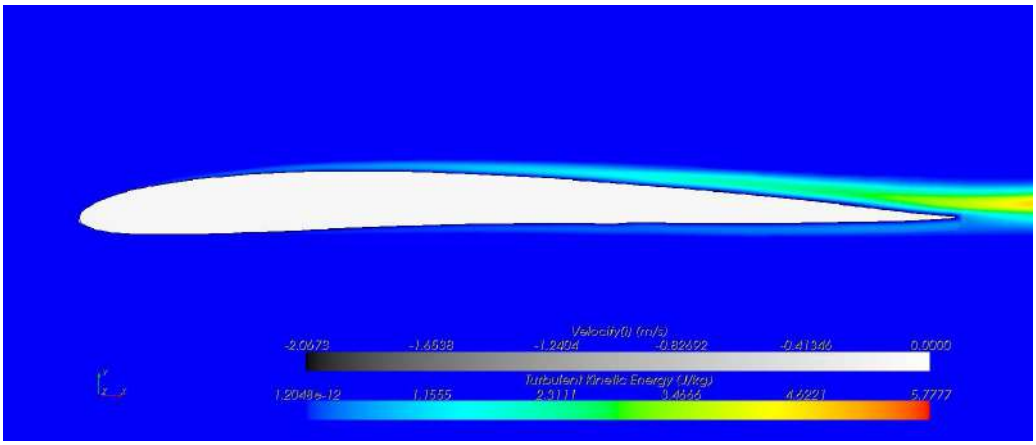

Figure 4.6: MA409, turbulent kinetic energy (J/kg), SA, AoA=4.57º, Re_1.

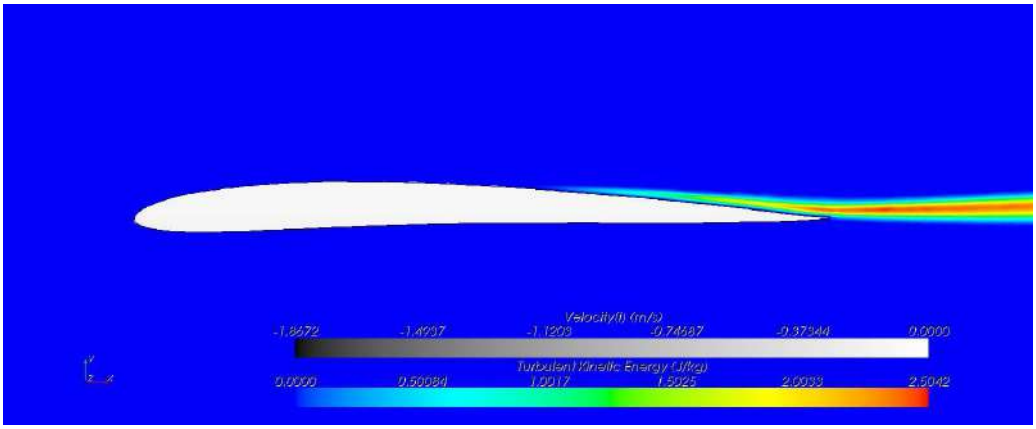

Figure 4.7: MA409, turbulent kinetic energy (J/kg), SA, TS, AoA=4.57º, Re_1.

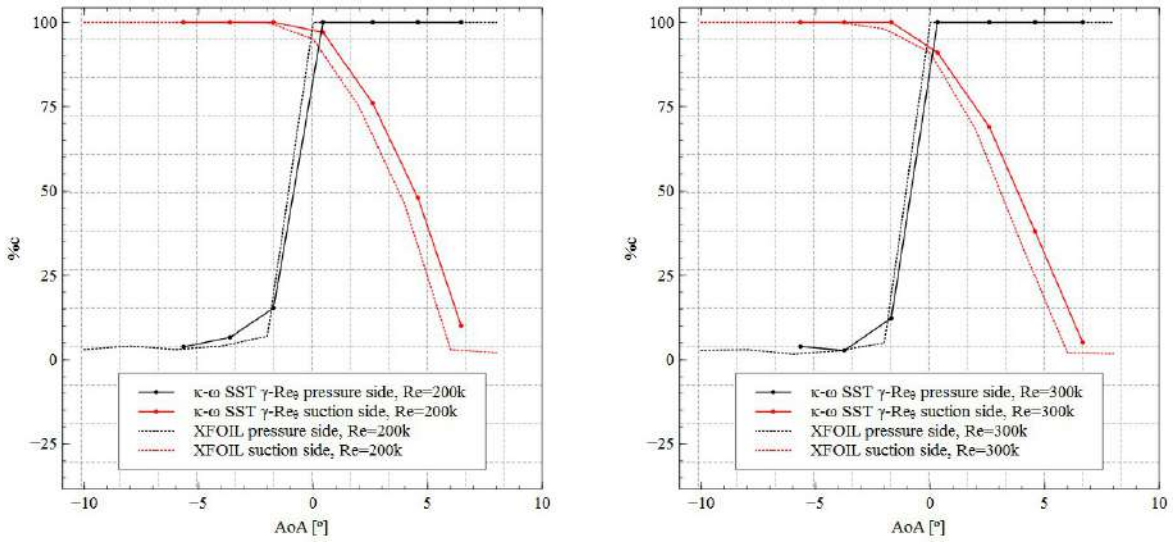

(a) Re_1 (b) Re_2

Figure 4.8: MA409, transition curves, XFOIL vs $k-\omega$ SST & $\gamma - Re_\theta$.

predicts natural transition to occur prior to the Star-CCM+ results. Similar results were obtained with airfoil CAL1215J, as seen in Figure A.2 in Appendix A.2. There are a few reasons that can justify these

small discrepancies. For one, the airfoils coordinates could be better defined. Airfoil MA409 leading edge and lower surface are a good example where surface irregularities can alter the pressure field about the airfoil. While XFOIL connects two adjacent coordinates using line segments, in Star-CCM+ splines had to be used instead of line segments in order to ensure a smooth airfoil surface. The use of splines might alter the surface original form, hence producing unexpected and different results. While using XFOIL, and when the input airfoil coordinates were of poor quality, XFOIL PANE function was employed. This function creates a better panel node distribution based on the original airfoil shape. No studies were performed with the objective of investigating the extent of the original airfoil deformation. Nonetheless, the possibility of having dissimilar airfoil shapes in both software packages might have its toll on the natural transition location discrepancies. Another factor was that XFOIL was used without any calibration having the user run the program with its default values, namely N_{crit} equaling nine. The e^n method has the user specified N_{crit} parameter which is the log of the amplification factor of the most amplified frequency which triggers transition. A suitable value of this parameter depends on the ambient disturbance level in which the airfoil operates, and mimics the effect of such disturbances on transition. When that parameter is equal to nine, the user is using the standard e^9 method which mimics conditions inside an average wind tunnel. Star-CCM+ can as well be a source of errors. Something that comes to mind has to do with the simulation inlet conditions where the user had to define the free-stream turbulence intensity and turbulent length scale without appropriate calibration tests based on wind-tunnel and flight test data. The consequence of doing so is that the transition model determines natural transition to occur at a determined place based on the inlet conditions. Several simulations using different free-stream turbulence intensity levels were performed using airfoil MA409 at Reynolds number Re_1 at an angle of attack of 4.57º while using the $k-\omega$ SST turbulence model and $\gamma - Re_\theta$ transition model. As seen in Table 4.1, for airfoil MA409 at an angle of attack of 4.57º, when the free-stream turbulence intensity levels increased, the LSB length (*dx*) and thickness (*dy*) decreased, and natural transition occurred further upstream. Lian and Shyy [40] also demonstrated using the same turbulence model, although using a transition criterion based on the e^N model, that the LSB became shorter and thinner with increasing free-stream turbulence intensity levels. In that study the transition location also occurred further upstream when increasing the free-stream turbulence intensity. These two studies show that the transition location and the flow characteristics are sensitive to the inlet conditions, although results show no significant discrepancies. Another aspect to have in consideration is the grid sensitivity. If the surface and volume meshes are not sufficiently defined around critical areas, the field might not be accurately resolved and as such the acquired aerodynamic data will not be realistic. Because extensive mesh studies on both airfoils were carried out in tandem with the aerodynamic simulations, and because the data from both turbulence models resemble the experimental data, it is very unlikely the airfoil surface and volume meshes produce a significant impact on these studies. There is also the fact that when using transition model $\gamma - Re_\theta$, two correlations were not published by its authors and what was used instead was the original correlations adaptation by the Star-CCM+ staff. No studies were performed regarding the transition model correlations, but naturally one has to keep in mind that minor adaptations might have significant impacts.

4.6 General Validation Conclusions

This chapter laid the bases for the subsequent aerodynamic simulations. Two turbulence models and two transition models were studied and their results compared with experimental data. When using those models certain precautions had to be taken into consideration, namely the mesh near the airfoils surfaces must be of acceptable quality and the inlet conditions must be appropriate.

Turbulence model Spalart-Allmaras although performing fairly well in terms of the lift coefficient did not perform as well when computing the airfoils drag coefficient at either Reynolds number. In terms of determining where natural transition occurs, even though the Turbulence Suppression model can be employed in certain field areas, it requires prior knowledge of the transition locations which is not known and is ultimately one of the objectives to meet. This model does not seem to detect where regions of reversed flow occur. In terms of convergence, this model residuals did converge to acceptable magnitudes much faster than the $k-\omega$ SST. This tendency is in line with the Stuart E. Rogers [41] studies where four turbulence models were compared, being Spalart-Allmaras and $k-\omega$ SST two of them. In conclusion, although highly regarded as one of the best turbulence models to perform aerodynamic analyses with, this model under-performs when dealing with simulations where the fields exhibit shear or separated flows.

On the other hand, the $k-\omega$ SST turbulence model when used together with the $\gamma - Re_\theta$ transition model provides accurate data for both aerodynamic coefficients and the natural transition location predictions are very similar to the XFOIL predictions. Combining the $\kappa - \epsilon$ turbulence model in the free-stream with the $\kappa - \omega$ turbulence model near walls, the $k-\omega$ SST model seems to be very accurate when solving the field in regions near walls. One negative aspect is that its residuals often do not rapidly converge like the SA turbulence model. P. Godin [42] arrived at similar conclusions using three two-dimensional airfoil configurations (two of them with high-lift surfaces) when testing the Spalart-Allmaras and $k-\omega$ SST turbulence models under different conditions. His conclusions are that the Menter model is more accurate in separated flow regions and the Spalart-Allmaras model is more accurate in attached flows and wakes, including merging boundary layers and wakes. As a final remark it is stated that the Spalart-Allmaras model is preferred for general computations of aerodynamic flows, whereas the Menter model is the better choice when separated flows are of primary interest.

Another aspect one has to bear in mind is how the mesh quality can influence the wall y+ factor and as a consequence transition predictions and its inherent aspects.

Finally, with all the simulations, validation tests and bibliography reviews, it was understood that only when using the $k-\omega$ SST turbulence model together with the $\gamma - Re_\theta$ transition model that acceptable lift, drag and transition predictions are to be expected.

Chapter 5

LEEUAV Airfoil Considerations

This chapter addresses the study of the LEEUAV airfoil. Picking up from last chapter, a series of aerodynamic simulations using XFOIL and Star-CCM+ were performed in order to understand what is expected of this airfoil at the design Reynolds number. In these studies, the application of the $k-\omega$ SST turbulence model used together with the $\gamma - Re_\theta$ transition model will once more be addressed and a series of studies simulating the flow behavior at different angles of attack performed. Transition studies are also addressed. Since the LEEUAV wing will have solar panels on its upper surface, two solar panel configuration studies are performed to understand their impact on the aircraft aerodynamic performance.

5.1 Clean Airfoil Aerodynamic Characteristics

As referenced in Section 2.4, the LEEUAV airfoil was designed for a minimum drag coefficient in the lift coefficient range of 0.6-1.5, subject to a maximum lift coefficient greater than 1.7, a relative thickness greater than 10% and a trailing edge thickness greater than 1 mm. Its shape is shown in Figure 5.1.

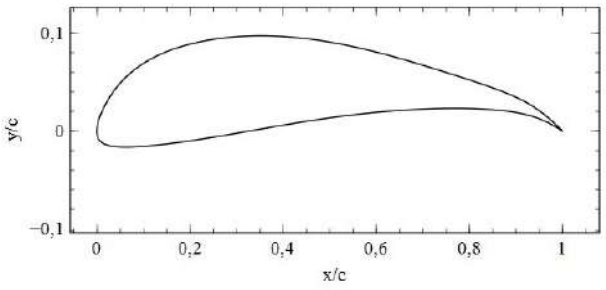

Figure 5.1: LEEUAV airfoil shape.

Analyzing the LEEUAV airfoil was an interesting task in the sense that no experimental data was available. Once again Star-CCM+ was the software of choice when performing CFD analyses. The same physics, turbulence and mesh models were employed as in the two previous airfoils.

Like the previous aerodynamic studies, the residuals did not converge when the steady state model was active. Vortex shedding was once more very active as shown in Figure 5.2 by the difference between the pressure coefficient curves obtained using XFOIL and Star-CCM+ at an angle of attack of 0^o. In that

figure three pressure coefficient curves are represented: the one obtained using XFOIL, and two other curves obtained using Star-CCM+, one of which is the instantaneous and the other that corresponds to the mean pressure coefficient curve. The instantaneous curve presents strong oscillations located at the airfoil aft lower surface. Because the XFOIL and Star-CCM+ averaged C_p curves resemble each other very much, this is a clear indicator the mean pressure field is very similar between the two programs. The laminar separation bubble extent and natural transition location are also being predicted to occur at the same location. Figure 5.3 shows the Q criterion at an angle of attack of 0º. This is a scalar used to visualize two- and three-dimensional turbulent fields and is sometimes preferred over contours of vorticity components to visualize flow structures like vortexes. This figure evidences vortex shedding from the airfoil with a determined frequency of 32.4 Hz.

Figure 5.4 was obtained from the same simulation and shows that in fact, the pressure coefficient variance is located at the airfoil lower surface trailing edge.

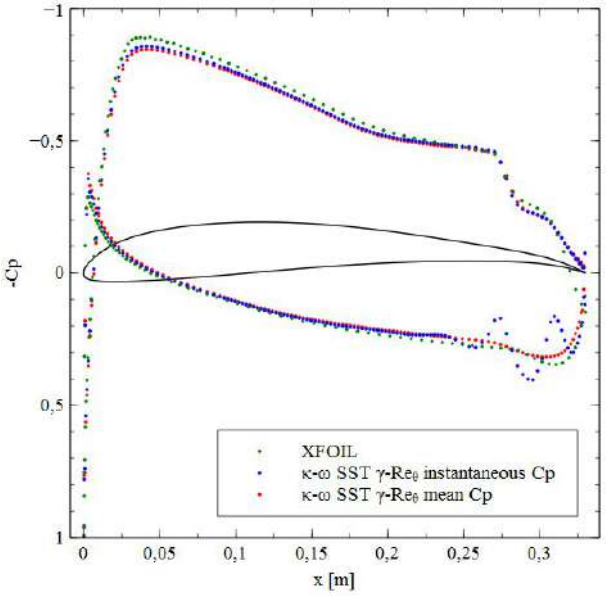

Figure 5.2: LEEUAV airfoil C_p curves, AoA=0º.

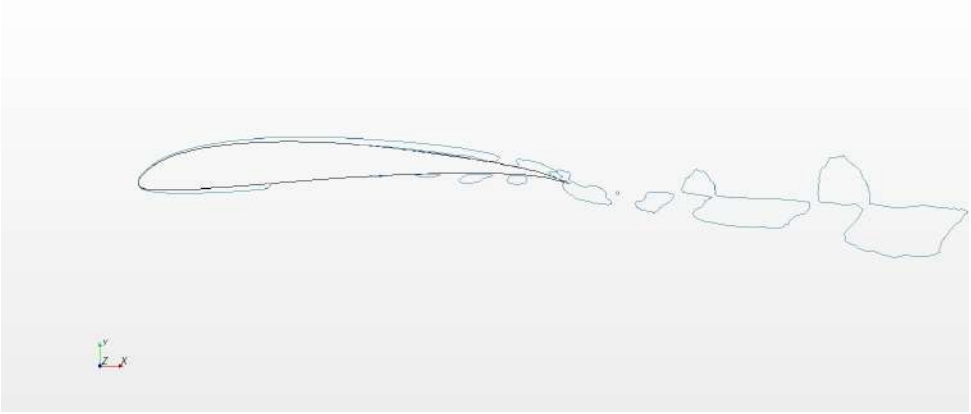

Figure 5.3: Q criterion contour, AoA=0º.

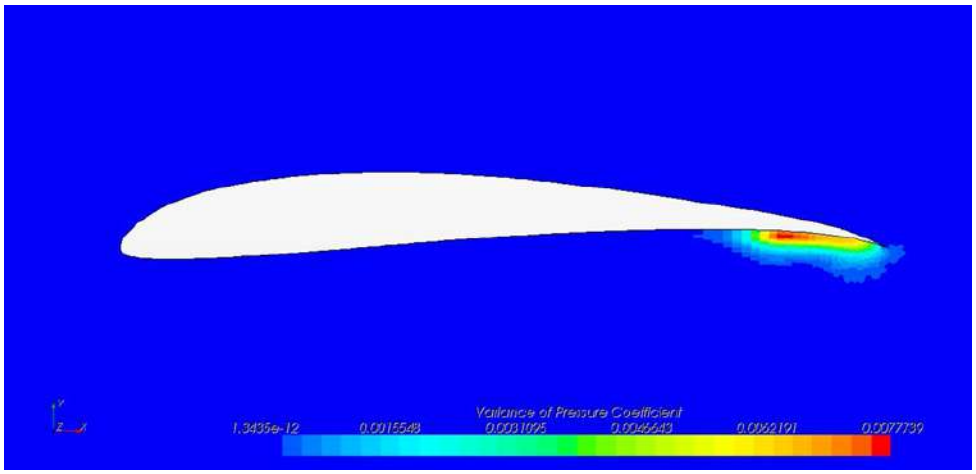

Figure 5.4: LEEUAV airfoil C_p variance, AoA=0º.

Like in the previous chapter, natural transition studies were performed. Great care was given in the mesh generation process so that the wall y+ factor is approximately one in the entire airfoil. Figure 5.5 compares the predicted natural transition locations using XFOIL and the $k-\omega$ SST turbulence model used together with the $\gamma - Re_\theta$ transition model. As it was the case with the transition curves from last chapter, both curves follow each other very closely and it seems in this case the predictions are slightly better. Unlike the aerodynamic studies of the previous two airfoils, the LEEUAV airfoil was well defined with enough point coordinates granting it a smoother surface, thus no spline treatment was necessary in either software. The wall y+ factor is also closer to unity which is also expected to produce better transition predictions.

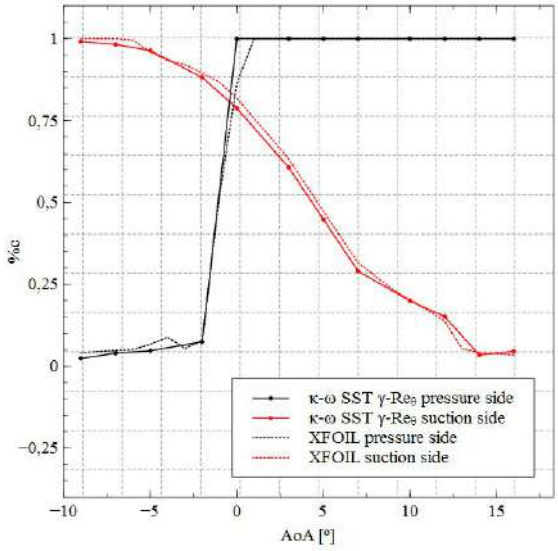

Figure 5.5: LEEUAV airfoil natural transition curves.

The mechanism in which transition occurs is the same as was first described in the previous chapter. The laminar separation bubble is a consequence of this particular Reynolds number regime. The boundary layer starts as laminar at the leading edge and after a while the flow starts to grow unstable and that is when the laminar boundary layer separates after the velocity peak. Afterwards the boundary

layer re-attaches itself now as a turbulent boundary layer thus forming a laminar separation bubble.

Looking at Figure 5.5 it is obvious that transition occurs gradually on the airfoil suction side. A laminar separation bubble forms near the trailing edge and as the angle of attack increases that bubble decreases in length and moves closer to the leading edge. This behavior is clearly illustrated in Figures 5.6 and 5.7. However, this gradual transition does not occur at the pressure side. No laminar separation bubbles were detected until angles of attack below 0º whereupon the flow becomes turbulent at the airfoil the leading edge. Figure 5.8 shows precisely one of those bubbles.

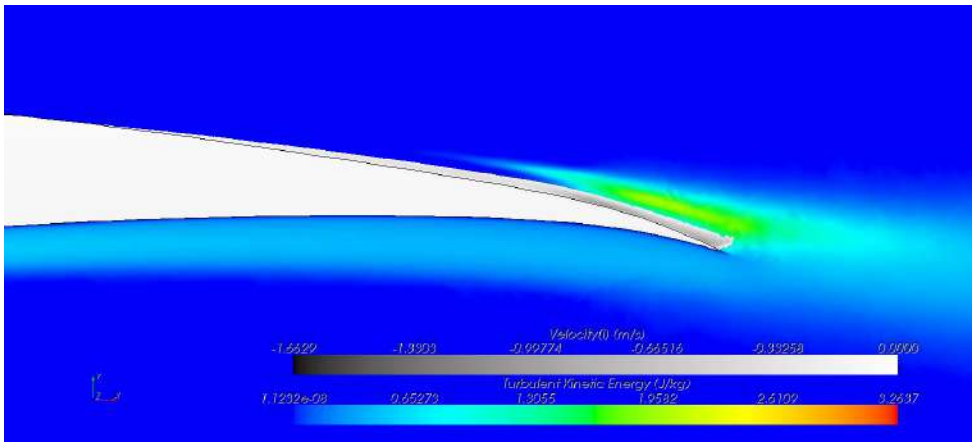

Figure 5.6: LEEUAV airfoil upper surface laminar separation bubble, AoA=-2º.

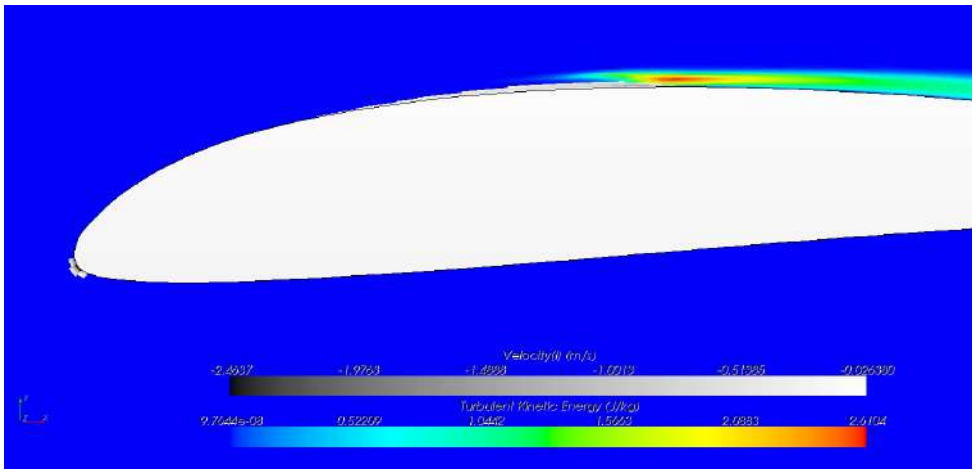

Figure 5.7: LEEUAV airfoil upper surface laminar separation bubble, AoA=7º.

Figure 5.9 shows the intermittency factor at an angle of attack of 5º. Close to the wall, in the viscous sublayer, the intermittency factor equals zero. There is a region on the outer boundary layer where the intermittency is approximately 0.5 which is caused by the laminar separation which occurs upstream of the re-attachment point. This flow strip disappears in the downstream direction as the turbulent boundary layer thickness increases.

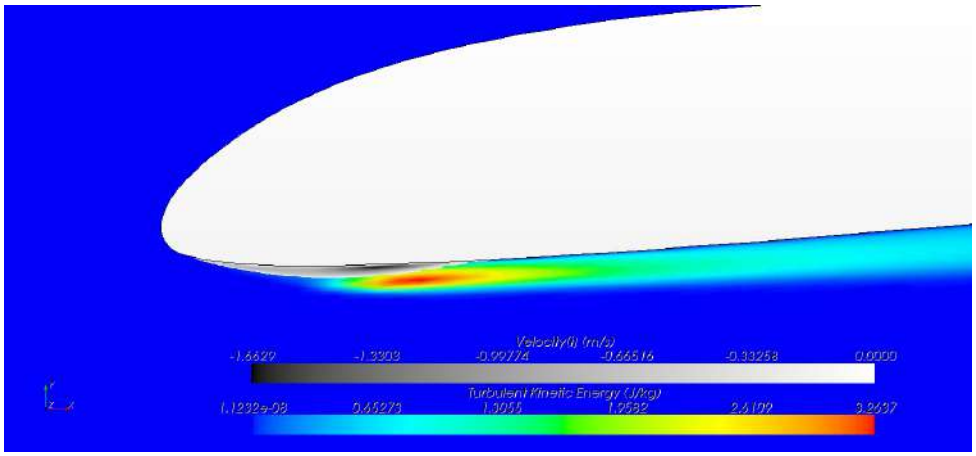

Figure 5.8: LEEUAV airfoil lower surface laminar separation bubble, AoA=-2º.

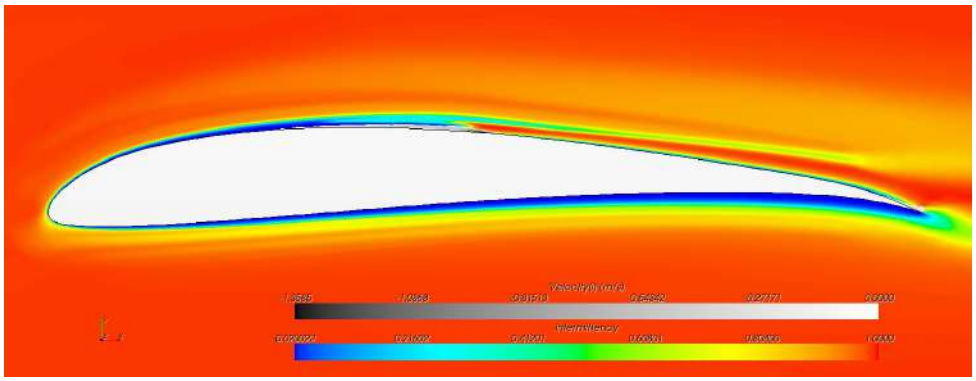

Figure 5.9: LEEUAV airfoil intermittency factor, AoA=5º.

5.2 Solar Panel Aerodynamic Considerations

The LEEUAV has a solar powered assisted propulsion and as such its batteries may recharge as it flies by using the energy surplus generated by its solar panels. These solar panels are placed on top of its wing, which can be a source of problems due to the fact that adding extra surfaces to the wing is essentially adding discontinuities to its surface which can produce effects similar to those of boundary layer trips. With the objective of understanding what happens at a two-dimensional level, two studies reproducing the effects of having offset surfaces on top of the LEEUAV airfoil were performed, simulating the effect of having solar panels on top of the wing. With the two-dimensional results one can infer what might happen on a three-dimensional level.

These studies, as seen in Figures 5.10 and 5.11, consisted of having two panel configurations: in configuration 1 a panel is placed on top of the original airfoil, thus increasing its thickness and adding two steps to the airfoil upper surface; in configuration 2 a tilted panel is added in order to have the panel trailing edge overlapping with the airfoil surface. It is expected that at high angles of attack the boundary layer will detach from the airfoil or wing surface due to the high adverse pressure gradients produced at those angles. The forward or leading edge step produced by the solar panels might help to decrease those effects by forcing the boundary layer to transition to turbulent, this way remaining attached at higher angles of attack. The solar panels used in these studies have a thickness of 2 mm and length of

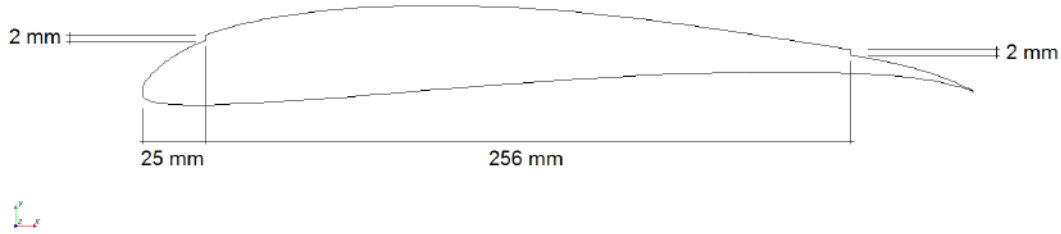

Figure 5.10: Solar panel configuration 1.

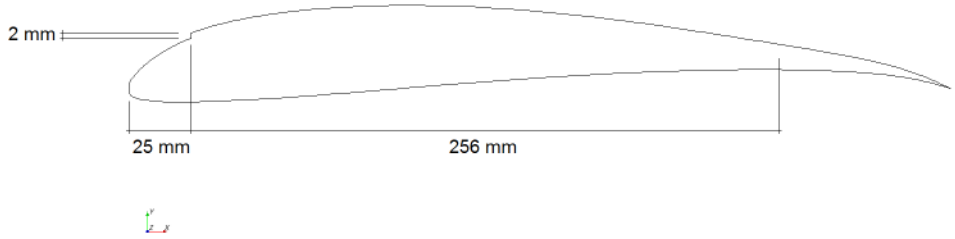

Figure 5.11: Solar panel configuration 2.

256 mm corresponding to two solar cells placed chordwise.

These aerodynamic simulations used a similar mesh, and the same turbulence and transition models as before.

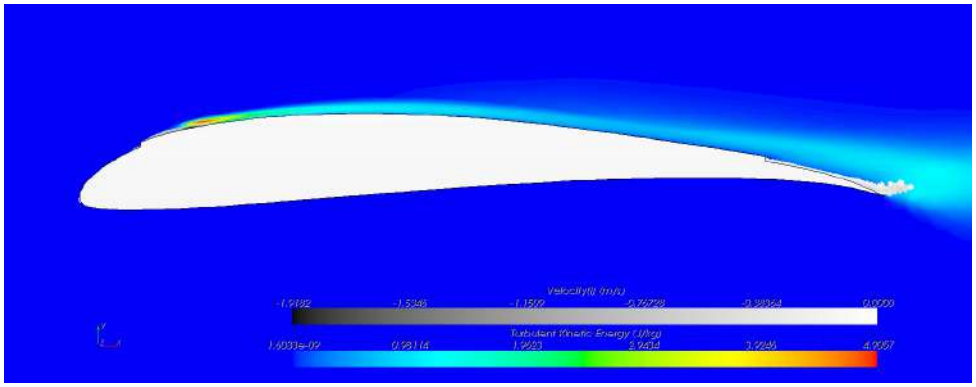

Figure 5.12: Solar panel configuration 1, turbulent kinetic energy (J/kg), AoA=5º.

Figures 5.12 and 5.13 show the turbulent kinetic energy generation around both solar panel configurations at an angle of attack of 5º. The simulations from both solar panel configurations show that the leading edge step promotes the formation of a laminar separation bubble which in turn forces the flow to become turbulent at that location. When simulating the air flow at negative angles of attack there is as well a laminar separation bubble near the leading edge but located on the lower surface like it was the case with the clean airfoil. The aft step in configuration 1 promotes the formation and locking of a

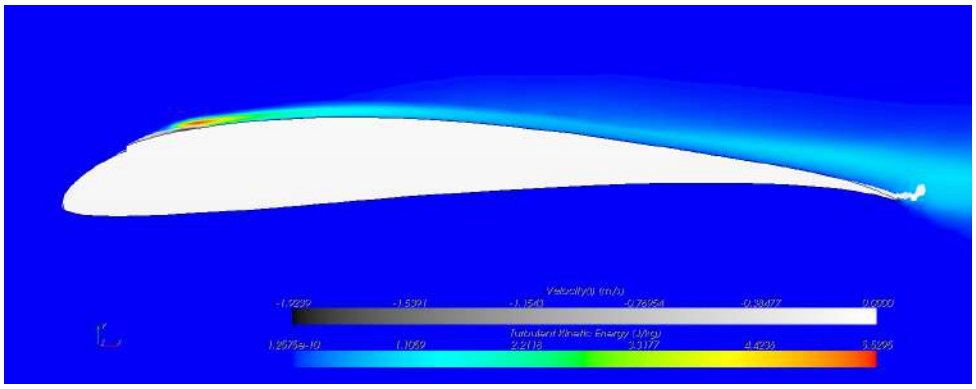

Figure 5.13: Solar panel configuration 2, turbulent kinetic energy (J/kg), AoA=5º.

recirculation bubble that at high angles of attack produces a region of reversed flow beginning at that location. The flow behavior around configuration 2 is very similar to what was encountered with the clean airfoil configuration with the exception of the effects from the panel leading edge step.

5.3 General Airfoil Conclusions

This chapter had the objective of providing an understanding of the LEEUAV airfoil air flow behavior at the design Mach and Reynolds numbers. In order to accurately simulate the air flow at different angles of attack, the mesh and physics models had to be adequate if later one wished to perform transition studies. The previous chapter had the purpose of addressing those issues and with its conclusions, this chapter simulations were performed following what was understood to be the best practice.

While generating the meshes for this chapter three test cases, great care was taken regarding the wall y+ factor. A better correspondence between XFOIL and Star-CCM+ natural transition locations was obtained when y+ was generally closer to unity. The fact that the LEEUAV airfoil has enough coordinate points so that its surface is well defined is another factor to keep in mind regarding the transition prediction between the two tested programs.

Transition occurs in much the same way as it was described in the previous chapter. The flow starts as laminar at both surfaces and after the pressure peak and strong adverse pressure gradient that follows, a laminar separation bubble forms. The flow experiences natural-turbulent transition when the boundary layer re-attaches. This bubble can appear in the upper or lower surfaces depending on the angle of attack. There is however the prevalence of this bubble on the airfoil upper surface and its movement while on this surface happens gradually from the trailing to the leading edge as the angle of attack increases. Its length also decreases as the angle of attack increases. The lower surface separation bubble forms at angles of attack below 0º in which case it has a length equal to half the airfoil chord. When decreasing the angle of attack even further, that long bubble moves towards the leading edge and is very short in length as Figure 5.8 clearly shows. Figure 5.9 presents the expected profile for the intermittency factor which leads to believe the field is being accurately computed.

Given the nature of the project, and since the LEEUAV requires the installation of solar panels on top

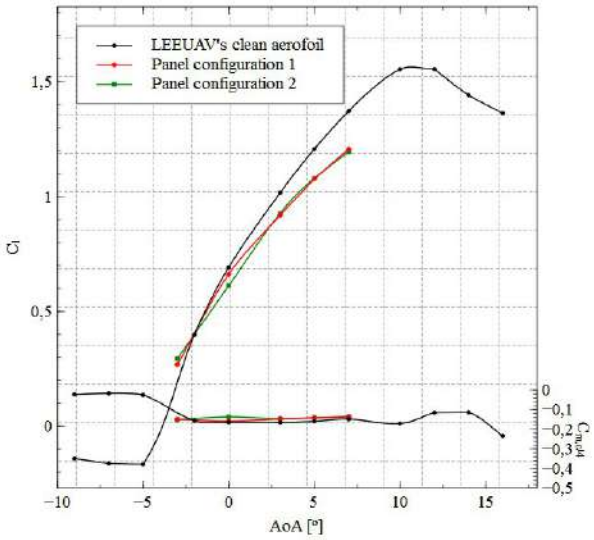

(a) C_l and $C_{m,c/4}$ versus AoA.

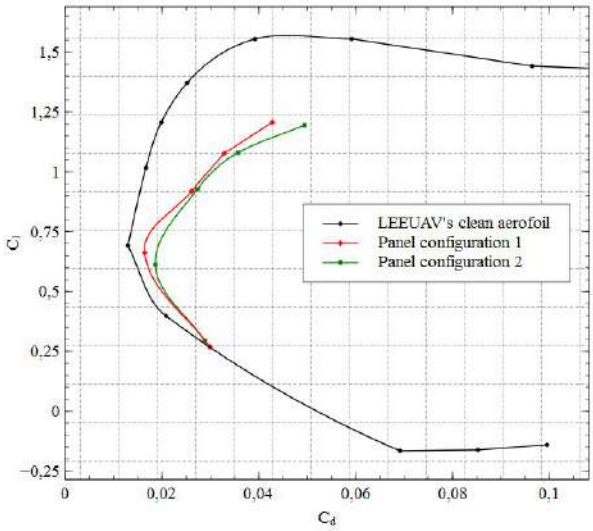

(b) C_l versus C_d.

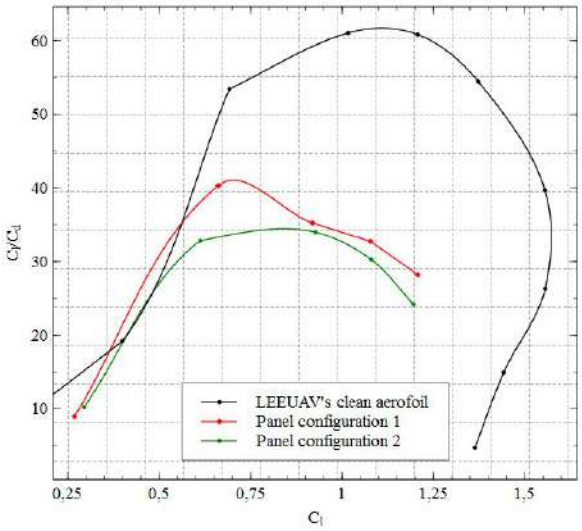

(c) C_l/C_d versus C_l.

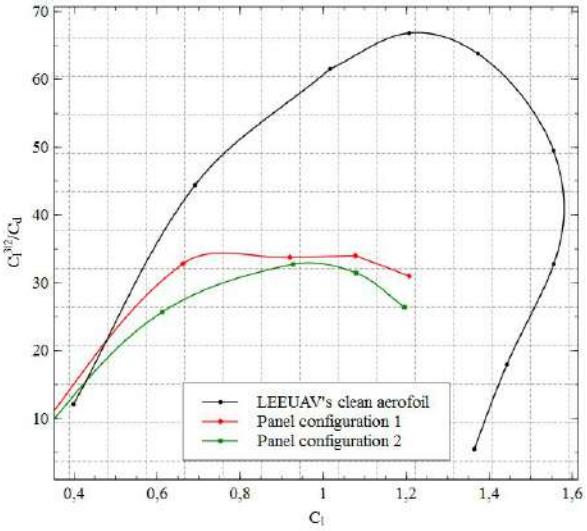

(d) $C_l^{\frac{3}{2}}/C_d$ versus C_l.

Figure 5.14: LEEUAV airfoil aerodynamic performance charts.

of its wing as a means to recharge its electric batteries and power its flight, two solar panel configurations were studied with the objective of understanding what are the consequences and alternatives regarding the solar panel installation locations and adaptations to the wing. In both configurations the panel forward step promotes the generation and fixation of a laminar separation bubble. The implications are the forced transition at that location with the inherent drag penalties due to turbulence. Configuration 1 presents a recirculation bubble at the panel aft step. As far as the lower laminar separation bubble is concerned, its length and locations exhibit the same behavior as the clean airfoil configuration.

Figure 5.14 shows the comparison between the lift and drag coefficients of the clean airfoil and both solar panel configurations. This figure shows that, for the tested configurations, placing a solar panel on top of the airfoil produces enormous penalties in both the lift and drag coefficients at any angle of attack. As bad as it may be, solar panel configuration 1 seems to present the best results as far as both configurations are concerned. It is obvious that the solar panels that will eventually make part of

the LEEUAV ought to be installed inside its wing, or if not, there is the need for implementing a smooth transition between the airfoil and solar panel. Possibly a new airfoil has to be developed with the objective of mitigating or reducing the negative impacts just discussed.

On the other hand, the LEEUAV clean airfoil configuration shows good aerodynamic performance. This is a relatively thin airfoil and as such its C_l vs AoA curve is very characteristic. Looking at the extremes of the range of angles of attack in Figure 5.14 a), and recalling the airfoil transition curves, the high angle of attack lift loss is somewhat gradual in comparison with the lower angle of attack abrupt lift slope variation at -5º. As the angle of attack increases so does the pressure peak as it moves towards the leading edge. This increase in adverse pressure gradient has its consequences on the upper surface laminar separation bubble location and length. The lift loss is rather abrupt at low angles of attack given the airfoil leading edge shape and the laminar separation bubble that develops there. C_l vs AoA curve slope has an estimated 6.15 rad^{-1} which is very close to the classical thin airfoil theory lift slope 2π rad^{-1} [43]. The airfoil presents, for cruise conditions, a maximum lift coefficient of 1.56 that occurs at an angle of attack of approximately 11º, which is below the expected 1.7. The airfoil moment coefficient at the quarter-chord point remains negative at the simulated angles of attack thus producing a pitch-down moment. Another performance objective was that the minimum drag coefficient should lie between the lift coefficient range of 0.6 to 1.5, and as can be seen in Figure 5.14 b), not only does this requirement is achieved but also the minimum drag coefficient is equal to 0.0129 and occurs when the lift coefficient equals approximately 0.07. Looking at Figures 5.14 c) and d), maximum C_l/C_d and $C_l^{3/2}/C_d$ occur when the lift coefficient equals 1.2. Figure 5.14 d) is only to be considered when using fuel consuming motors rather than electric motors. This airfoil aerodynamic performance data is listed in Table 5.1.

Table 5.1: LEEUAV airfoil aerodynamic performance table.

Maximum lift coefficient	C_{lmax}	1.56
Maximum lift angle of attack	$\alpha_{C_l max}$	11º
Zero lift angle of attack	α_{0lift}	-4º
Lift vs angle of attack curve slope	$C_{l\alpha}$	6.15 rad^{-1}
Minimum drag coefficient	C_{dmin}	0.0129
Zero lift drag coefficient	$C_{d,0}$	0.0207
Maximum lift-to-drag ratio	$C_l/C_{d_{max}}$	61.03
Angle of attack of maximum lift-to-drag ratio	α_{C_l/C_dmax}	3º
Maximum lift$^{3/2}$-to-drag ratio	$C_l^{3/2}/C_{d_{max}}$	66.8
Angle of attack of the maximum lift$^{3/2}$-to-drag ratio	$\alpha_{C_l^{3/2}/C_dmax}$	5º

Chapter 6

LEEUAV Baseline Aerodynamic Performance

This chapter introduces the full three-dimensional LEEUAV mesh generation process and physics model selection. By the end of the chapter, a number of aerodynamic details concerning the LEEUAV cruise flight phase will be addressed including its flight performance.

6.1 Physics Models and Mesh Considerations

Last chapter focused on understanding the flow physics around the LEEUAV airfoil at the design Reynolds number. Not only that, the mesh and physics models studies substantially helped to understand what would be the starting point when making the transition from the two-dimensional to the three-dimensional studies.

The physics models and settings are the same as those used for the LEEUAV airfoil. At this point it should be emphasized that four transport equations, two for the turbulence model and two for the transition model, are being computed in each iteration step, in addition to the Navier-Stokes equations for mass and momentum.

The previous mesh studies also helped to understand what mesh characteristics should be defined around the wing. However, mesh studies around the fuselage and tail regions needed to be addressed in order to understand what kind of settings and control volumes should be employed. The final decision was to have four control volumes covering different regions of the LEEUAV: control volumes 1 and 2 (CV1 and CV2, respectively), cover the entire wing, control volume 3 (CV3) covers the fuselage regions between the nose and mid tail boom and control volume 4 (CV4) englobes the entire LEEUAV. The reason behind having two control volumes covering the entire wing was due to the fact that the wing was built through sections and with the objective of adapting the control volumes to different wing sections, two control volumes were generated. Apart from control volume CV4, no control volume is present around the aircraft tail region. This decision was made based on one of this thesis objectives which was to allow the swift aerodynamic analysis of general UAV configurations. One of the implications is that if

there are several UAV regions that are extremely refined, the number of mesh cells grows rapidly and the simulations take even longer to converge, if they converge. Apart from the refining control volumes, there is as well the computational control volume here referenced as global CV. Figure 6.1 and Table 6.1 show the different control volumes locations and relative dimensions, respectively. The dimensions in Table 6.1 are relative to the LEEUAV mean airfoil chord ($\bar{c}$) and wingspan (b).

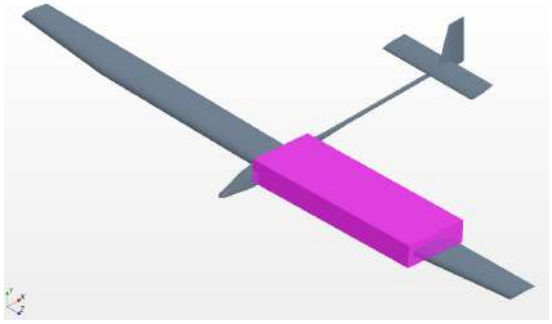

(a) CV1.

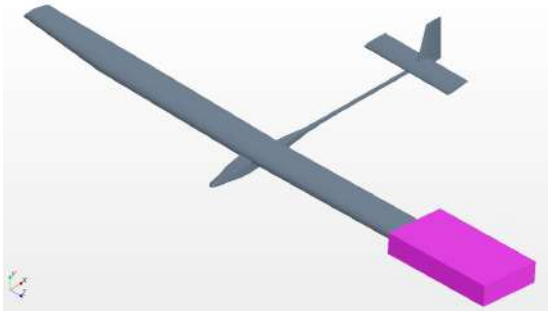

(b) CV2.

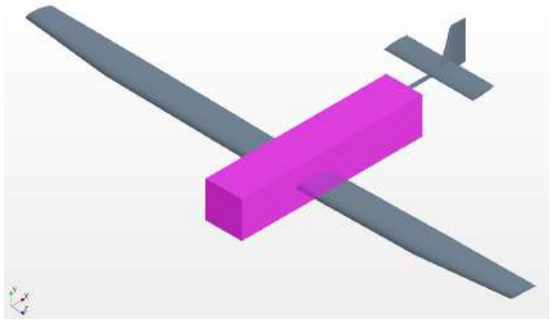

(c) CV3.

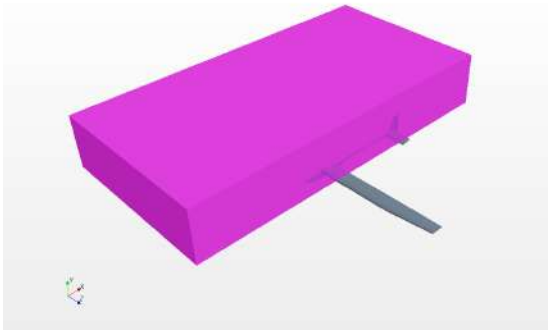

(d) CV4.

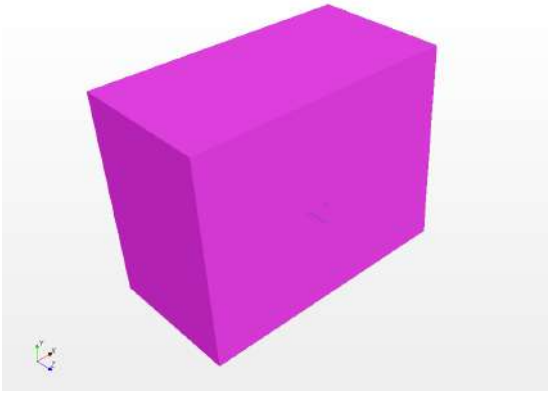

(e) Global CV.

Figure 6.1: Three-dimensional control volume dimensions.

Table 6.1: Control volumes dimensions in the three-dimensional simulations.

	CV1	CV2	CV3	CV4	Global CV
Length	1.5$\bar{c}$	1.5$\bar{c}$	5$\bar{c}$	20$\bar{c}$	70$\bar{c}$
Width	4.5$\bar{c}$	3$\bar{c}$	$\bar{c}$	10.5$\bar{c}$	3b
Height	0.5$\bar{c}$	0.5$\bar{c}$	$\bar{c}$	3.5$\bar{c}$	60$\bar{c}$

6.2 Mesh Selection

The strategy employed in the mesh selection process was to begin with a coarse mesh having a small number of cells and increasingly refine that first mesh while adjusting key parameters. Based on the lift and drag coefficients and CPU time per iteration evolution, a final mesh would be selected and with that mesh several in-depth simulations would be performed. Having these criteria in mind, a total of five meshes were created. These meshes had approximately 3, 5, 7, 10 and 20 million cells and the parameters under analysis were the cell base size in control volumes CV1, CV2, CV3 and CV4. The different meshes will from now on be addressed as 3M, 5M, 7M, 10M and 20M according to their respective number of cells. This mesh refining study is described in Table 6.2.

Table 6.2: LEEUAV three-dimensional mesh parameters.

	3M Cells	5M Cells	7M Cells	10M Cells	20M Cells
Base Size (m)	0.35	0.35	0.35	0.35	0.35
Number of Prism Layers	25	25	25	25	25
Prism Layer Stretching	1.2	1.2	1.2	1.2	1.2
Prism Layer Thickness (m)	0.015	0.015	0.015	0.015	0.015
Surface Growth Rate	1.1	1.1	1.1	1.1	1.1
VC1 Custom Size (m)	0.009	0.006	0.0047	0.0041	0.003
VC2 Custom Size (m)	0.009	0.006	0.0047	0.0041	0.003
VC3 Custom Size (m)	0.09	0.09	0.08	0.07	0.05
VC4 Custom Size (m)	0.1	0.1	0.1	0.1	0.09

In order to decide which mesh should be employed in the final and more detailed aerodynamic analyses, three simulations per mesh would be performed accounting to a total of fifteen simulations. Those three simulations per mesh would definitely include first and second-order steady and possibly unsteady discretization techniques which were expected to produce different residual magnitudes, convergence rates and aerodynamic data. If the aerodynamic coefficients and residuals converged and the later presented acceptable magnitudes at steady state regimes, there would be no need to use unsteady state models since these take considerably longer to present acceptable results.

For the airplane to fly horizontally, its weight ought to be balanced by the lift it generates. This simple principle allowed to determine what was the minimum lift coefficient to fly at steady horizontal flight, based on the LEEUAV data provided in Chapter 2.

$$Weight = Lift \Leftrightarrow W = L = \frac{1}{2}\rho_\infty U_{cruise}^2 S C_L \Leftrightarrow C_L = \frac{W}{\frac{1}{2}\rho_\infty U_{cruise}^2 S} = \frac{4.9 \times 9.81}{\frac{1}{2} \times 1.1116 \times 7.53^2 \times 1.5} = 1.015 \tag{6.1}$$

Having computed the minimum C_L with which the LEEUAV would maintain a steady horizontal flight with Eq. (6.1) it was determined from the aerodynamic simulations that the airplane should fly at an angle of attack of approximately 0º. Based on this result, the different mesh selection simulations were performed at the aforementioned angle of attack.

Figure 6.2 shows three studies between the different meshes. The objective was to understand what

was happening in terms of the lift and drag coefficients and CPU time per iteration as the number of cells increased. Looking at Figure 6.2 a), as the number of cells increases, the lift coefficient decreases and at twenty million cells that coefficient still is not stabilized, although the coefficient magnitude is changing at the order of 10^{-2}. Mesh 7M exhibits the closest results between steady and unsteady state simulations. On the other hand, mesh 20M presents the most similar results between second order steady and unsteady state simulations. Figure 6.2 b) shows the drag coefficient evolution for the different meshes. Unlike the previous figure, the steady second order and unsteady state drag coefficients seem to be converged after mesh 7M which leads to believe that this mesh might be appropriate for the remainder simulations. Figure 6.2 c) shows the CPU time per iteration step evolution as the number of cells increases. There is little difference between the first and second order steady state simulations. As for the unsteady state simulations, the CPU time increases dramatically with increasing number of cells. Ideally, to obtain the aerodynamic data as fast as possible, it would be best to run simulations using steady state schemes. However, to make this decision, one first needs to look at the different meshes residuals magnitudes.

From all the simulations with the different meshes, only mesh 7M and 20M presented acceptable residual magnitudes while using steady state second order schemes. Looking at Figure 6.2 the decision to use mesh 7M in the remainder aerodynamic simulations was made. Although it seems the lift coefficient has not yet stabilized as the number of cells increases, that is not the case for the drag coefficient. Furthermore, the CPU time per iteration of mesh 7M, using six Intel XEON processors, is 297.12 s while for mesh 20M is 774.42 s. Having in consideration it took respectively 1800 and 2000 iterations for the residuals of meshes 7M and 20M to converge, one is dealing with simulations that are expected to take approximately five and a half and almost eighteen days to present acceptable results. This time estimate does not account for the I/O time and the communication channel delay. In terms of memory usage, mesh 7M required 12 GB of RAM while mesh 20M required at least 30 GB. This way, mesh 7M seems to be the best compromise between cost and accuracy.

6.3 LEEUAV Three-Dimensional Aerodynamic Analysis

Having the final mesh been selected, several aerodynamic simulations were performed at different angles of attack for the cruise flight phase.

In the previous chapter it was understood that there are laminar separation bubbles present on the airfoil surfaces and, depending on the angle of attack, those bubbles change their location, length and thickness. The flow behavior and its intrinsic consequences found on the LEEUAV airfoil are present on its wing. The flow naturally transitions on the wing surfaces thus creating the well known laminar separation bubbles. Although at low angles of attack the bubbles thickness are relatively small, the wing effective shape does not remain the same which in turn affects the pressure field in its vicinity. Throughout the simulations, and depending on the angle of attack, there are long laminar separation bubbles located on the wing upper and lower surfaces.

The wing lower surface LSB is only predicted at negative angles of attack and can be quite exten-

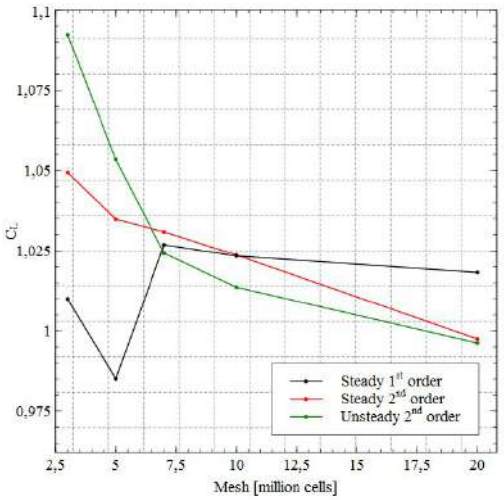

(a) C_L evolution.

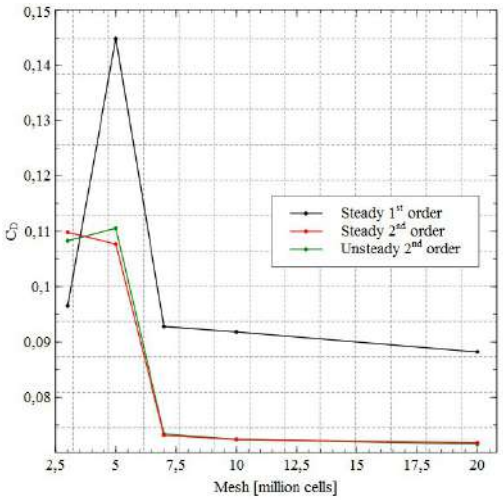

(b) C_D evolution.

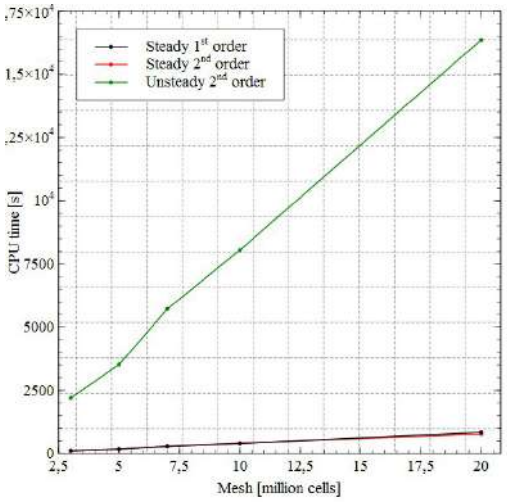

(c) CPU time evolution.

Figure 6.2: C_L, C_D and CPU time evolution with mesh refinement.

sive. Its presence is first detected at -4º and is located generally over the wing's latter half, as seen in Figure 6.3. Its width is not the same throughout the wingspan. The bubble width near the wing root is approximately 30%c, and gradually increases until wing section S2 where it remains approximately constant and equal to 60%c until the wingtip. Its thickness is approximately one or two millimeters over the wingspan. As the angle of attack decreases to -6º, the bubble locates itself at the wing leading edge and its width is approximately half the wing chord. At this angle of attack the bubble width can be considered approximately constant over the entire wingspan and its thickness ranges from one to four millimeters. At -8º, the LSB width decreases and locates itself near the wing leading edge. At -10º the flow is no longer attached to the wing and there are large regions of separated flow as seen in Figure 6.4. Beginning at -6º, located at the wing lower surface near the wing root a region of reversed flow starts to develop and increases as the angle of attack decreases.

The wing upper surface presents laminar separation bubbles at every simulated angle of attack and every bubble has a length of about 90% the wingspan. No laminar separation bubbles are detected on the wing area on top of the fuselage and close to the wingtip. Below -6º there is only one small LSB

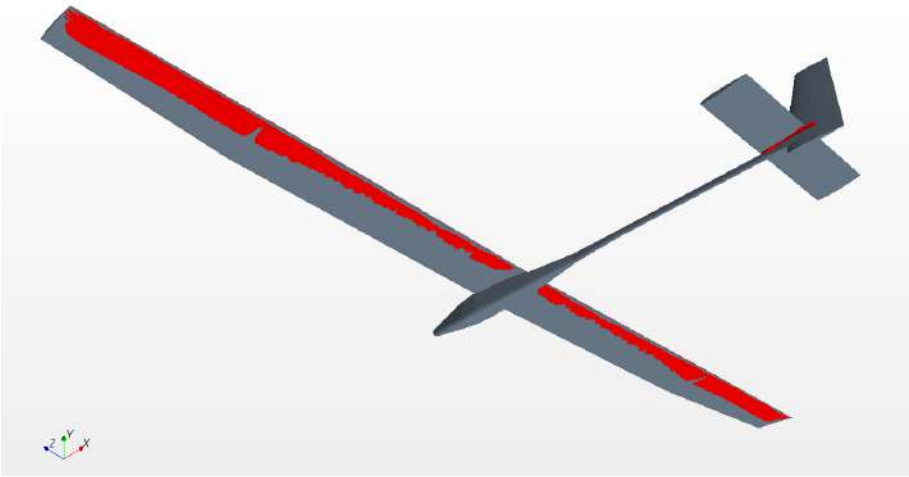

Figure 6.3: Spanwise lower laminar separation bubble, AoA=-4º.

Figure 6.4: Spanwise lower laminar separation bubble, AoA=-10º.

located at the trailing edge. At -6º, the LSB is uniformly distributed over the wing upper surface and its width is approximately 30%c and is located at the trailing edge. As the angle of attack increases the bubble moves closer to the leading edge which is consistent with the airfoil simulations. In the angle of attack range of -6º to 0º the bubble width decreases to values of approximately 15%c. Figure 6.5 shows the wing upper surface bubble at 0º. In the angle of attack range of 2º to 4º the bubble naturally keeps moving closer to the leading edge but its width now increases to values of approximately 45%c. From then on, as the angle of attack increases even further, the bubble width gradually decreases while remaining close to the leading edge. Above 2º, located in the surface region where the wing meets the fuselage and starting at the wing leading edge, a region of separated flow starts to develop. As the angle of attack increases the flow region where the flow is separated grows even further in both the Oy and Oz directions. Figure 6.6 shows this region of separated flow at an angle of attack of 8º. After 8º, when the lift coefficient has its maximum value, the leading edge bubble bursts at several locations along the wingspan and consequently the flow is no longer attached to the wing surface which in turn produces massive lift loss. The regions where separated flow occurs start at the leading edge which in terms of lift loss present what is typically known as leading edge loss. It is the worst kind of lift loss since it tends

to occur abruptly. Figure 6.7 shows three main regions of separated flow: the wing-fuselage surface, the mid-wing surface and in between wing sections S2 and S3. This later region is particularly dramatic since it is where the ailerons are located. This means that at high angles of attack, when the flow is separated in most of the wing surface, there is no way of controlling the LEEUAV roll actuating surfaces. Depending on the angle of attack, the wing upper surface bubble thickness presents different values. In general, away from the wing root region and while the bubbles have not burst yet, their thickness were found to range between one and six millimeters.

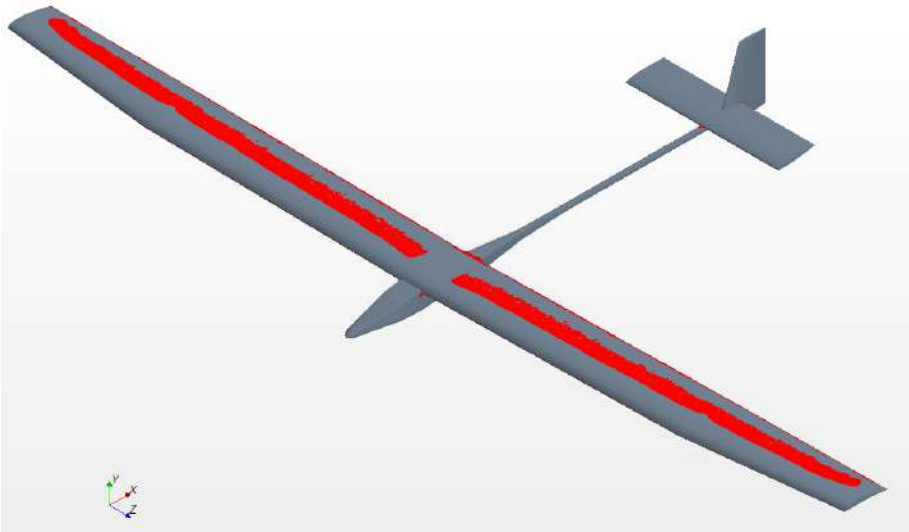

Figure 6.5: Spanwise upper laminar separation bubble, AoA=0^o.

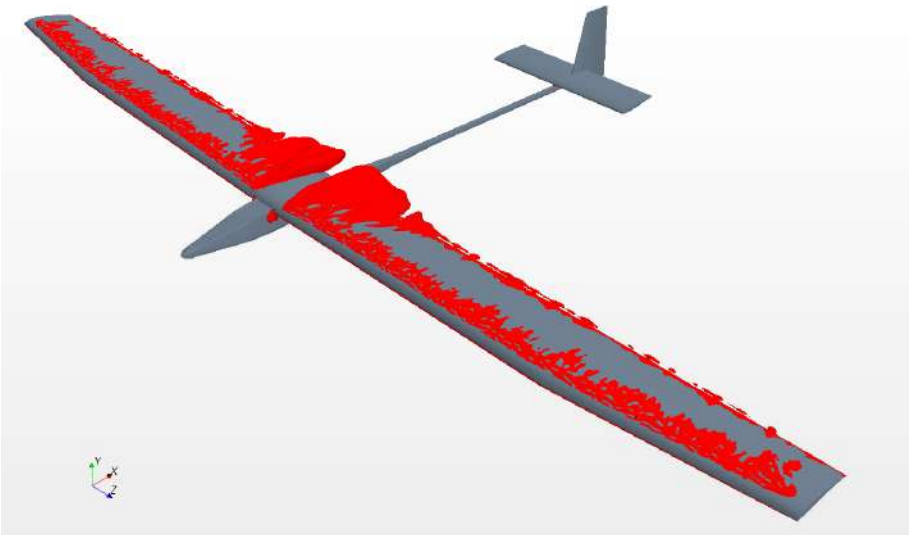

Figure 6.6: Wing upper surface flow separation, AoA=8^o.

Apart from the laminar separation bubbles, there are a few other aspects around this UAV that might need some attention and improvement. One of those, which might help with the wing upper surface bubble wingspan reduction resides at the wingtip. As it was designed, the wingtip is truncated rather than being a round smooth surface which accompanies the lower and upper wing surfaces. This geometric feature produces small recirculation bubbles and does not facilitate the natural flow passage from the

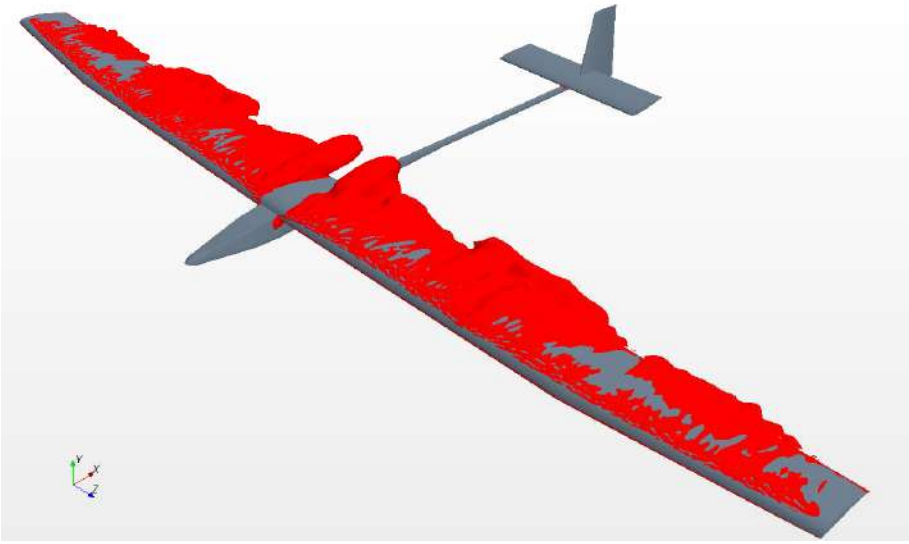

Figure 6.7: Wing upper surface flow separation, AoA=10º.

wing pressure to the suction side which in turn could possibly reduce the spanwise laminar separation bubble length.

Figure 6.4 shows another region that might have some influence on the UAV aerodynamics which is located at the wing root area. In that region, located at the wing lower surface and in the interface with the fuselage, there is a large reversed flow region that is present at angles of attack ranging from -10º to -4º. Because the LEEUAV wing root region was not designed to enable a particularly smooth transition between the wing and fuselage, this geometric feature produces undesired effects such as the one just described or the wing upper surface region of reversed flow that starts to develop at angles of attack above 2º.

Figure 6.8 shows the lift distribution along the wingspan. It has the expected quasi-elliptical shape where near the fuselage the lift coefficient is slightly inferior than the maximum lift coefficient along the wingspan, which at 0º is 1.14 located at z=600 mm. Near the wingtip, as expected, the lift coefficient gradually decreases to values nearing zero.

Figure 6.9 presents the pressure coefficient curves, at an angle of attack of 0º, at four different wing sections that are perpendicular to the wingspan direction as Figure A.8 from Appendix A.3 shows. The three pressure curves closer to the fuselage present pressure peaks occurring at the same location because the wing chord at those locations remains the same and the wing has no sweep. Among the four pressure curves, the two closer to the fuselage present similar pressure peaks and the same happens to the later two curves. This evidences a decrease in the local velocity along the wingspan direction. Because the laminar separation bubble presents the same width and is generally located at the same distance from the leading edge, the pressure curve suction side oscillations occur at the same location.

In the two previous chapters and when analyzing the laminar separation bubbles, it was understood through the intermittency factor and turbulent kinetic energy that the bubble generation process happened after the laminar boundary layer separated and later re-attached itself now as a turbulent

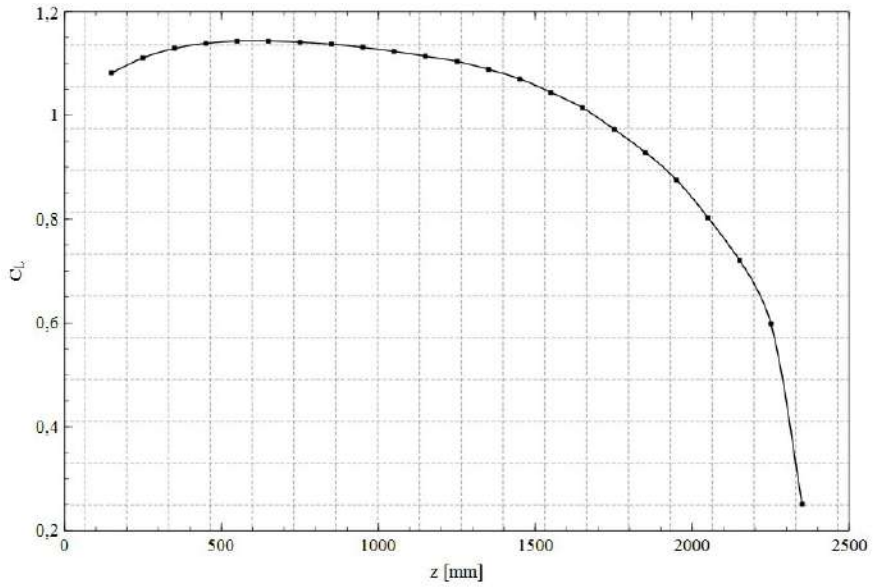

Figure 6.8: Spanwise lift distribution, AoA=0º.

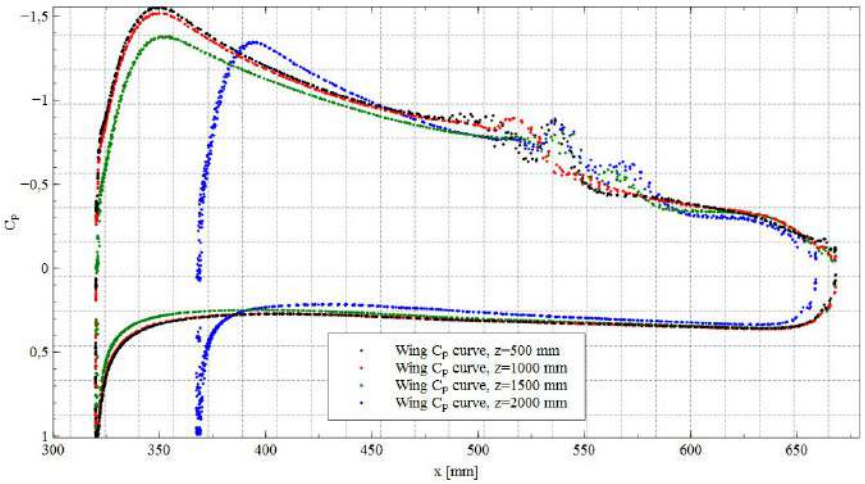

Figure 6.9: Wing Ox C_p curves, AoA=0º.

boundary layer. This way, it is expected that the simulated air flow becomes turbulent after passing over the bubbles on the wing surfaces. Furthermore, it is expected that the flow becomes turbulent along the fuselage due to adverse pressure gradients in the nose region.

Figure 6.10 gives an idea of the transition process at an angle of attack of 0º by showing in red the isosurface where reversed flow is detected and in blue the isosurface of the turbulent kinetic energy that gives an idea where the flow is expected to be turbulent. The flow first becomes turbulent after going around the LEEUAV nose where it encounters adverse pressure gradients. Figure 7.7 shows in red the pressure coefficient around the aircraft nose. Afterwards, the turbulent boundary layer grows and propagates over the fuselage, tail boom and tail. This figure shows that the horizontal and vertical stabilizers inner surfaces are in the turbulent wake region that was shed from the fuselage upstream of the tail. The transition model predicts bypass transition in these surfaces as a consequence of the high local freestream turbulence intensity from the wake. Outside the wake, the local freestream turbulence

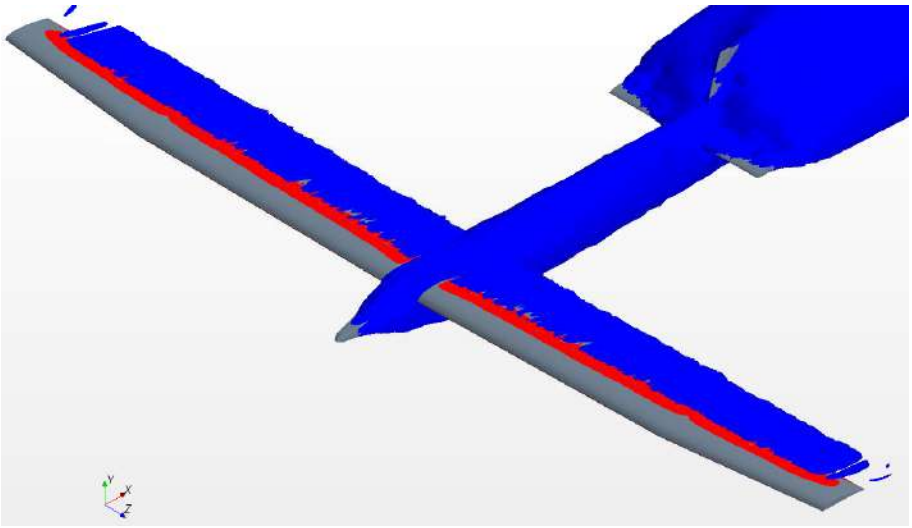

Figure 6.10: Isosurfaces of reversed flow (red) and turbulent kinetic energy (blue), AoA=0º.

intensity is low and as a result the transition model predicts natural transition. These results are in line with the obtained results from reference [44]. As it would be expected, the flow becomes turbulent after the wing separation bubbles.

Figure 6.11 shows two contour plots of the wing and tail skin friction coefficient. Figure 6.11 a) shows an increase in the skin friction coefficient after the laminar separation bubble and Figure 6.11 b) shows an increase in the skin friction coefficient on the inner tail surfaces. These surface areas where the skin friction increases are expected as a consequence of natural transition over the wing surfaces and tail bypass transition due to the fuselage turbulent wake. On the horizontal and vertical stabilizer surfaces, outside the turbulent wake, there is an increase in the skin friction coefficient which leads to believe natural transition is predicted in those surface areas.

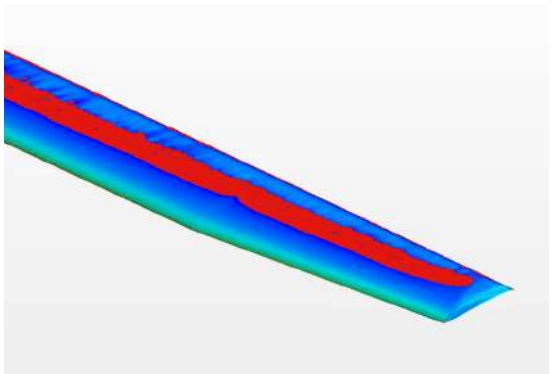

(a) Wing upper surface skin friction coefficient.

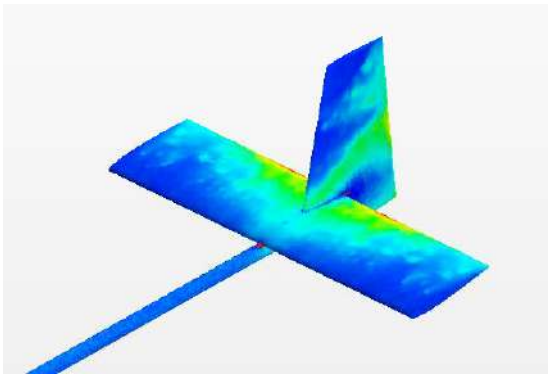

(b) Boom and tail skin friction coefficient.

Figure 6.11: Skin friction coefficient (C_f) contour plot with reversed flow isosurface in red, AoA=0º.

With the selected mesh it also possible to capture fine physics details such as the horseshoe vortexes located at the wing root and wingtip regions, as seen in Figure 6.12. In that figure, one can see the streamlines evidencing the vortexes located at the wingtip and wing root regions. The brown lines evidence the vortex cores. In this figure, apart from the horseshoe vortexes, one can as well detect through the vortex core lines, that a wingtip vortex in the horizontal stabilizer is also detected as would be

expected. Figure A.3 from Appendix A.3 presents a front view of the wingtip vortex where the streamlines revolve around the vortex core, and Figures A.4, A.5, A.6 and A.7 evidence surface streamlines around the LEEUAV from different views. Looking at the surface streamlines one can easily see where the flow is attached to the surface and where the laminar separation bubbles are located, where the flow moves inboard or outboard in the wingspan direction as a consequence of the wing finite shape and local pressure distribution.

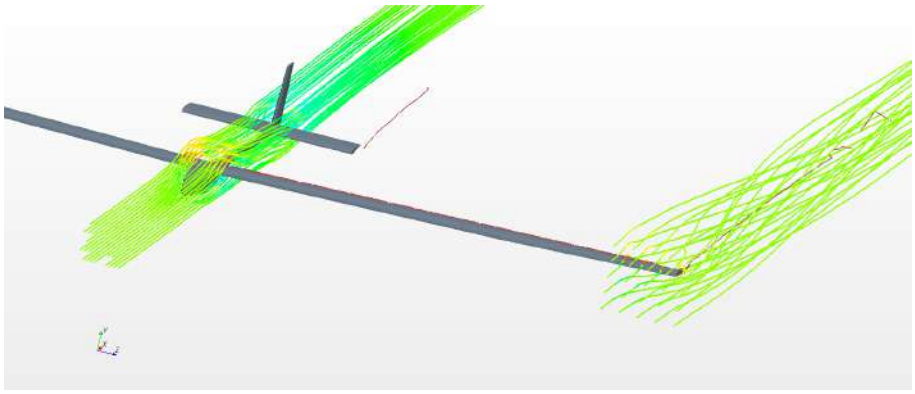

Figure 6.12: Horseshoe vortexes, AoA=0º.

Figure 6.13 shows the lift and drag data for the simulated angles of attack. A total of eleven angles of attack were simulated from -10º to 10º, with 2º increments.

Figure 6.13 a) shows the LEEUAV lift and moment coefficients evolution with the angle of attack. Maximum lift coefficient is obtained at 8º and is approximately equal to 1.51. The lift curve slope is 5.59 rad^{-1} which is lower than the slope obtained for the airfoil, as expected. The moment coefficient, obtained at the quarter-chord point, evidences that the LEEUAV, as it was designed, is naturally stable. At positive angles of attack it produces a pitch-down moment whereas at negative angles of attack its tendency is the opposite.

Figure 6.13 b) shows the LEEUAV drag polar. Minimum drag, C_{Dmin}, equals 0.0527 and is obtained when the lift coefficient is equal to 0.41 which corresponds to an angle of attack of -6º. Obtaining the minimum drag at that angle of attack is understandable since the wing has an incidence angle of five degrees with respect to the fuselage, which means the wing is actually operating at an angle of attack of -1º. At angles of attack close to 0º, the wing pressure or form drag is considerably lower since it is aligned with the flow. Zero lift drag, $C_{D,0}$, is approximately 0.06 and is obtained when the LEEUAV flies at -9º. In the lift coefficient range of -0.07 to 1.2, that corresponds to angles of attack ranging from -10º to 2º, the drag polar resembles a parabola with C_D increasing very little when compared to C_L. In the lift coefficient range of 1.2 to 1.51, that corresponds to an angle of attack in the range of 2º to 8º, the drag polar presents an almost linear behavior. It is also at this angle of attack range that the lift slope slightly decreases. An explanation for this behavior might have to do with the region of separated flow that starts to develop precisely at this angle of attack range at the wing root region. For angles of attack above 8º, the drag coefficient increases dramatically while the lift coefficient starts decreasing which is a clear indicator, as shown by Figure 6.7, of massive flow separation over the wing surfaces. Flying at angles of attack above 8º should be avoided at the risk of the aircraft losing lift and the wing control

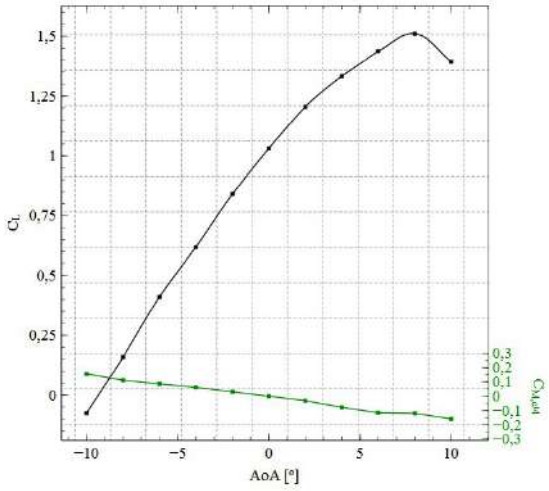

(a) C_L and $C_{M,c/4}$ versus AoA.

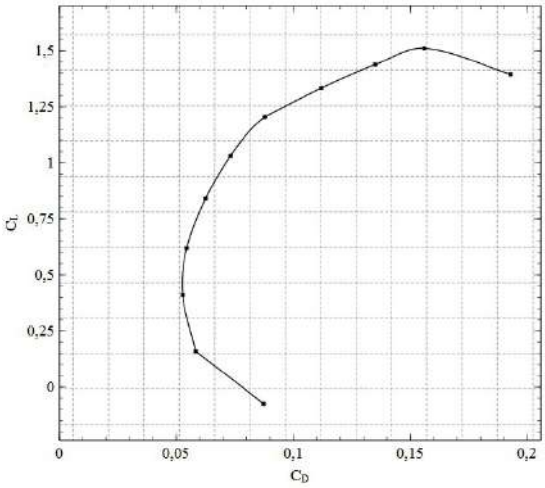

(b) C_L versus C_D.

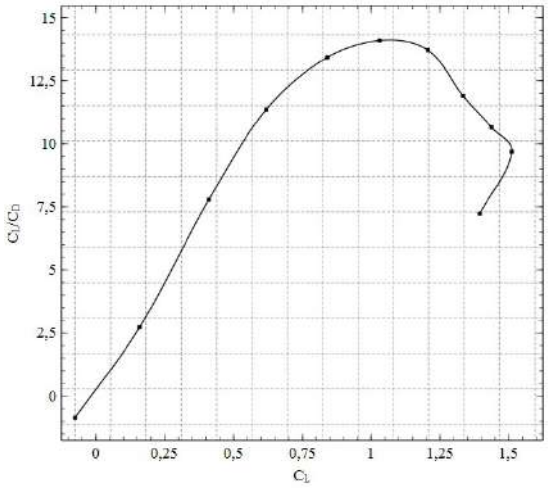

(c) C_L/C_D versus C_L.

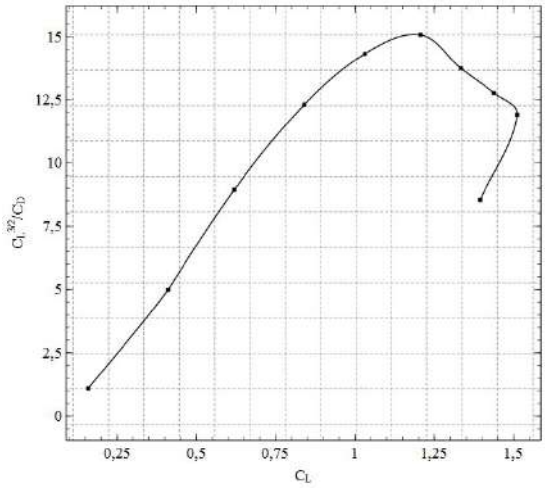

(d) $C_L^{\frac{3}{2}}/C_D$ versus C_L.

Figure 6.13: LEEUAV aerodynamic performance charts.

surfaces not being able to actuate the aircraft.

Figures 6.13 c) and d) show the C_L/C_D and $C_L^{\frac{3}{2}}/C_D$ evolution with C_L. The first figure gives an idea of the lift coefficient the airplane should have to maximize its range and consequently its endurance. The second figure indicates the airplane maximum endurance in terms of its lift coefficient in case the LEEUAV should fly with internal combustion engines. Figure 6.13 c) shows that C_L/C_D has its peak when the lift coefficient is between 1 and 1.2, which occurs when flying the aircraft at angles of attack close to 1º, thus it is at this angle of attack the LEEUAV should operate to maximize its range and endurance during its cruise flight phase. Looking at Figure 6.13 d), for the airplane to maximize its endurance it should fly at angles of attack that produce lift coefficients in the order of 1.2, which means it should fly with an angle of attack of about 2º.

Table 6.3 summarizes the LEEUAV aerodynamic performance data.

As Figure 6.13 shows and Table 6.3 summarizes, the maximum lift-to-drag ratio obtained in the aerodynamic simulations was 14.01 which is below the estimated 20 at cruise conditions.

Table 6.3: LEEUAV aerodynamic performance table.

Maximum lift coefficient	C_{Lmax}	1.51
Maximum lift angle of attack	$\alpha_{C_{L}max}$	8º
Zero lift angle of attack	α_{0lift}	-9.5º
Lift vs angle of attack curve slope	$C_{L\alpha}$	5.59 rad^{-1}
Minimum drag coefficient	C_{Dmin}	0.0527
Zero lift drag coefficient	$C_{D,0}$	0.06
Maximum lift-to-drag ratio	$C_L/C_{D_{max}}$	14.01
Angle of attack of maximum lift-to-drag ratio	α_{C_L/C_Dmax}	0º
Maximum lift$^{3/2}$-to-drag ratio	$C_L^{3/2}/C_{D_{max}}$	15.06
Angle of attack of the maximum lift$^{3/2}$-to-drag ratio	$\alpha_{C_L^{3/2}/C_Dmax}$	2º

The cruise stall speed is determined as

$$U_{stall} = \sqrt{\frac{2W}{\rho_\infty S C_{Lmax}}} \tag{6.2}$$

where W corresponds to the LEEUAV weight, ρ_∞ is the atmospheric air density at 1,000 m, S is the wing planform area and C_{Lmax} the maximum lift coefficient. Using Eq. (6.2) the LEEUAV stall velocity is determined to be 6.21 m/s which is very close to the expected 6.1 m/s.

The LEEUAV maximum cruise speed is determined equaling its thrust to its drag and solving for V_{max} which results in the following equation [45]:

$$U_{max} = \sqrt{\frac{(T_A/W)_{max}(W/S) + (W/S)\sqrt{(T_A/W)^2_{max} - 1/(L/D)^2_{max}}}{\rho_\infty C_{D,0}}} \tag{6.3}$$

where $(T_A/W)_{max}$ is the maximum thrust-to-weight ratio and (W/S) is the wing loading. Using the information available from reference [19] to determine the maximum available thrust and this thesis aerodynamic results, the LEEUAV maximum cruise velocity was determined to be 29.3 m/s, which is well above the estimated 21.1 m/s.

At the beginning of this chapter a brief description of the mesh selection process was addressed. Some of the reasons why mesh 7M was selected was because it was one of two meshes that allowed to run simulations with residuals of acceptably low magnitudes and because its CPU time per iteration was reasonable. However, if one recalls the Spalart-Allmaras airfoil simulations, it comes to mind that its residuals convergence rate was fairly good and its lift and drag predictions quite accurate within reasonable angles of attack. This way, to compare the two models predictions now at a three-dimensional level, several studies involving the SA turbulence model were performed. Figure 6.14 shows the lift and drag coefficients comparison between the two turbulence models and their percentile discrepancy.

In this analysis, as it was the case when dealing with the airfoil studies, the SA model presents excellent lift coefficient predictions at angles of attack below 6º. As the angle of attack increases, flow separation in specific regions start to develop and this model fails to predict lift loss which is clearly seen in Figure 6.14 a). When the predicted lift coefficient with the $k-\omega$ SST model reaches its peak at 8º and then starts to decrease with increasing angle of attack, the SA model does not predict lift loss at

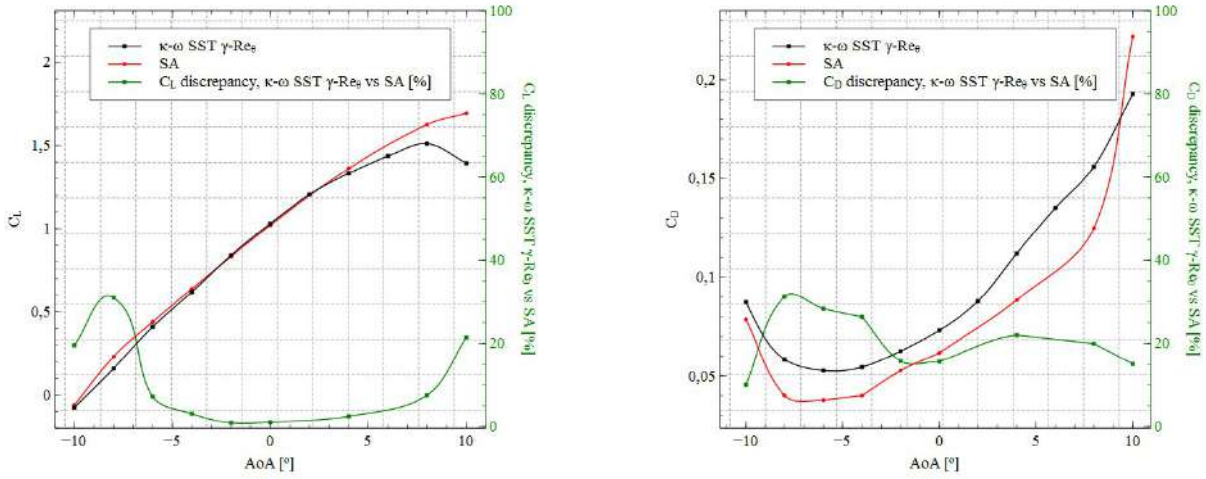

(a) C_L versus AoA.

(b) C_D versus AoA.

Figure 6.14: LEEUAV aerodynamic performance comparison, $k-\omega$ SST vs SA.

that angle. In fact, the lift coefficient continues to increase although at a slightly lower rate. In general, from the performed simulations, the lift data obtained with the SA model is in accordance with the $k-\omega$ SST model for angles of attack below 6º. Although at high angles of attack the SA model lift predictions fail to detect lift loss, at the recommended angles of attack, the SA model predictions seem to be very accurate.

As for the drag coefficient, like it was the case when analyzing the airfoils, turbulence model SA fails to produce aerodynamic data that is in line with what the $k-\omega$ SST model presents. However, the last time these two models were compared in terms of drag coefficient prediction, turbulence model SA generally overpredicted this coefficient at low angles of attack. In these three-dimensional analyses it seems the tendency is the opposite. From -10º until approximately 9º, the drag coefficient predicted by the SA model underpredicts the $k-\omega$ SST drag data. One reason for this discrepancy might have to do with the mesh itself since that at a three-dimensional level it would not be reasonable to produce a fine mesh in all regions of the control volume at the risk of increasing the computation time. Generally the percentile discrepancy between the two models is in the range of 10% to 30%.

Although the SA model predictions failed to provide accurate lift data at high angles of attack and the computed drag data is underpredicted when compared to the $k-\omega$ SST model, it provides swift simulations with low residuals magnitudes and every simulation was obtained in under 1500 iteration steps. As only one transport equation, apart from the Navier-Stokes equations for mass and momentum, needs to be computed in each iteration step, the CPU time per iteration is approximately 120 s which means each simulation using this turbulence model takes in average two days to provide acceptable results. All simulations were performed on the same machine using the same number of processors. The memory usage is approximately 12 GB or RAM.

6.4 General LEEUAV Conclusions

This chapter first introduced the mesh and physics models studies in which it was understood which mesh presented the best aerodynamic results while having in consideration the time and accuracy inherent to those simulations. From those studies it was understood that only mesh 7M provided acceptable aerodynamic data and the best CPU time per iteration considering the convergence of the lift and drag coefficients and the residuals magnitudes.

Having selected the appropriate mesh, numerous aerodynamic simulations were performed at different angles of attack where apart from collecting the lift and drag data, several aerodynamic effects were studied as well. Those effects were the now well known laminar separation bubbles present on the LEEUAV wing and wingtips, wing root reversed flow regions and wing horseshoe vortexes.

All of these phenomena were expected given the prior two-dimensional simulations and the LEEUAV geometry at its wingtip and wing root regions. The laminar separation bubbles form as a consequence of the laminar boundary layer detachment and later re-attachment. This was clearly captured in Figure 6.10 and is an excellent example of natural transition over almost the entire wingspan. Looking at the fuselage region between the nose and the wing, the flow is also predicted to become turbulent as a consequence of the increasing adverse pressure gradients. As the boundary layer transitions from laminar to turbulent, it generates a turbulent wake around the fuselage that propagates in the downstream direction. In the aforementioned figure, at 0^o, that wake flows over the inner parts of the tail which in turn induce transition in those surfaces. This transition mechanism is due to the high turbulence intensity present in the local freestream and is known as bypass transition.

The recirculation bubbles located at the lateral fuselage surfaces below the wing leading edge are expected to be the consequence of the number of fuselage cross-sections. A solution would be to increase the number of cross-sections, especially in the regions where the fuselage cross-section area changes rapidly.

The wingtip bubbles are the consequence of the chosen wingtip geometry. If a round surface would have been modeled, the air that flows from the pressure to the wing suction side might accompany the surface and eventually reduce the laminar separation bubble on the wing upper surface.

On the wing root region, because no wing root fairing was designed, beginning at 2^o, a region of separated flow starts to develop and increase as the angle of attack also increases. It is believed this separated flow region is responsible for the LEEUAV lift slope decrease and drag increase beginning at that angle of attack.

In terms of performance parameters, the predicted lift-to-drag ratio is 14.01 which is approximately 30% below the design objective which was 20. The predicted stall speed is in line with the design objective and the cruise maximum speed was determined to be 29.3 m/s which is well above the estimated 21.1 m/s. There may be a number of reasons as to why the obtained cruise performance values differ from the design parameters. In Chapter 2 there was a reference to the methods used in the performance parameters estimation which consisted in using low-fidelity methods such as empirical correlations which although practical at an initial design point may not be very accurate. In this thesis, through the employ-

ment of high-fidelity methods such as the use of turbulence models, the obtained results are expected to be more realistic.

As a matter of curiosity, the SA model was used in several simulations and its results compared with the ones from the $k-\omega$ SST model. Generally, the lift data showed good agreement between the two models for angles of attack bellow 6º. For angles of attack above 6º the SA model failed to predict lift loss. Once again, when comparing the drag predictions between the two models there are some discrepancies and the SA model fails to predict aerodynamic effects such as natural transition. However, the SA model CPU time per iteration step is considerable lower than the $k-\omega$ SST model which is a highly desirable characteristic.

In conclusion, the $k-\omega$ SST turbulence model used with the $\gamma-Re_\theta$ transition model predicted results that are in line with the two-dimensional studies. It seems these models are accurate and capture fine mesh phenomena like the horseshoe vortexes as long as the mesh is appropriate. One known problem with these two models is the convergence rate and residuals magnitudes that depending on a series of factors, like the mesh quality, might require extensive troubleshooting procedures. On the other hand, the SA turbulence model provided relevant lift data at low angles of attack and all simulations residuals converged in under 1500 iterations steps while presenting acceptable magnitudes. This leads to believe that if lift data is to be obtained quite rapidly, one could and should use this turbulence model. However, if relevant drag predictions are to be computed, and when no information regarding transition location is available, then the $k-\omega$ SST turbulence model used with the $\gamma-Re_\theta$ transition model is recommended.

Chapter 7

Parametric Optimization Studies

Last chapter dealt with the aerodynamic evaluation of the LEEUAV as it was designed in the conceptual stage. However, in the course of studying the flow behavior around the LEEUAV at different angles of attack, it was understood that some geometric characteristics should be the subject of parametric studies and aerodynamic considerations. This chapter addresses the proposed parametric studies.

7.1 Rounded Wing Tips

The wingtip geometry, as it was originally designed, is truncated rather than having a rounded surface. An expected consequence of having a truncated wingtip is that the vortex located in that region will develop on that surface outer regions. The purpose of designing and simulating the flow around a rounded wingtip was to create a smooth surface without discontinuities that enabled the easier flow passage from the wing pressure side to the suction side [46]. With the proposed design, the long laminar separation bubble that covered approximately 90% of the wingspan might be reduced. If that is the case, there might be a reduction, however small, in the wing drag components which is highly desirable.

Figure 7.1 shows the comparison between the isosurfaces of reversed flow, at an angle of attack of 0^{o}, for the original and newly proposed wingtip design. The two top sub-figures show the isosurfaces of reversed flow in the original wingtip geometry and the two bottom sub-figures show the same kind of isosurfaces for the new rounded wingtip geometry. Comparing the two configurations, it is understood that the recirculation bubbles located at the wingtip truncated region are now non-existent. Furthermore, with the new geometry and at the simulated angle of attack, there is a reduction in the upper LSB of approximately three centimeters. Figure 7.2 compares the wingtip vortex location between the original and proposed wingtip geometries. With the rounded wingtip, the wingtip vortex effectively moves in the fuselage direction thus proving the beneficial effects in reducing the wing LSB. In terms of lift and drag coefficients there are no significant gains although the wing drag coefficient decreased very slightly.

(a) Original wingtip geometry, top view.

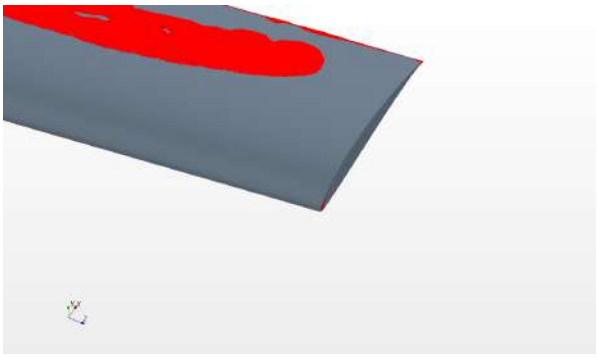

(b) Original wingtip geometry, side view.

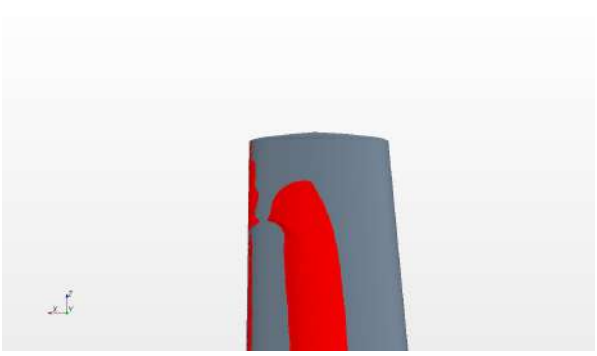

(c) Rounded wingtip geometry, top view.

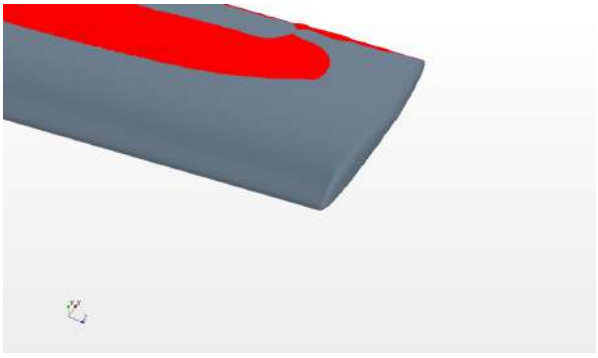

(d) Rounded wingtip geometry, side view.

Figure 7.1: Isosurfaces of reversed flow in the wingtip surfaces, AoA=0º.

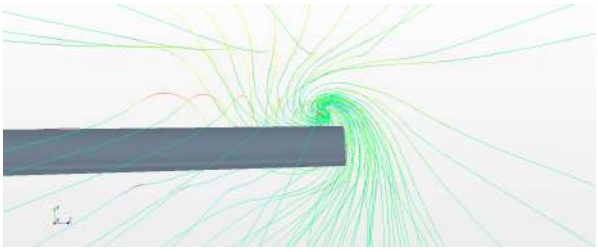

(a) Original wingtip vortex location.

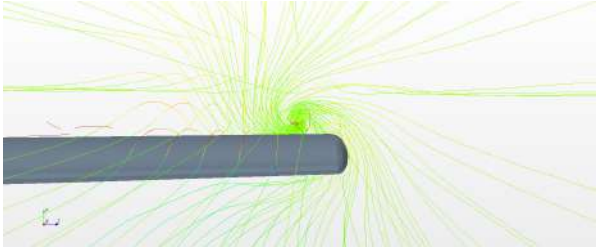

(b) Rounded wingtip vortex location.

Figure 7.2: Comparison between the original and rounded wingtip vortexes location.

7.2 Wing Root Fairing

The LEEUAV wing root region was not designed to present a particularly smooth transition between the wing and fuselage surfaces. Not having a smooth geometric transition between those surfaces proved to generate undesired aerodynamic effects. One of those was the development, beginning at 2º, of a region of separated flow on the wing upper surface. As the angle of attack increased so did that region of separated flow, which in turn increased the LEEUAV drag.

The wing root region is critical due to the intersection of two bodies with their own pressure distribution fields and boundary layers. If no geometric transition is employed, the drag build-up could, in the right conditions, dramatically increase in those areas.

The LEEUAV wing has a positive offset of 5º with respect to the fuselage longitudinal axis and the incoming airflow. The consequences are that above angles of attack of -5º the wing lower surface

boundary layer will generally be very thin, thus its interaction with the fuselage boundary layer is not expected to be significant. On the other hand, the wing upper surface boundary layer is subject to more intense pressure gradients that promote rapid boundary layer growth and flow separation which was detected in the previous simulations.

Figure 7.3 shows the proposed wing root fairing design. The top view evidences the increase in the wing root chord, while maintaining the original linear trailing edge design. This gradual increase in the wing chord was developed to ensure a smooth geometric transition between the fuselage and wing. The view from the LEEUAV underbelly shows that a smooth transition between the fuselage lateral faces and wing was also ensured with the objective of eliminating the recirculation bubble that developed in that region at negative angles of attack.

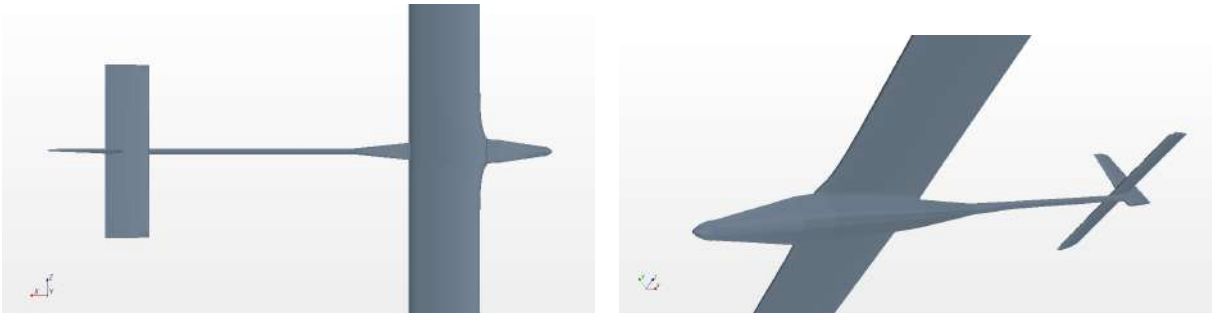

(a) Wing root fairing top view.

(b) Wing root fairing underbelly view.

Figure 7.3: Wing root fairing views.

Figure 7.4 compares the regions of reversed flow at 4º, between the two wing root configurations. Figure 7.4 a) shows the original wing root design and the region of reversed flow created by the geometry at that location and the consequent interaction between the wing and fuselage boundary layers. Figure 7.4 b) shows that in the newly designed wing root fairing, apart from the wing upper surface laminar separation bubble, the regions of reversed flow are now considerably smaller and their thickness are comparable to that of the separation bubble, if not smaller. In terms of reducing the region of separated flow, the introduction of the wing root fairing was a major improvement.

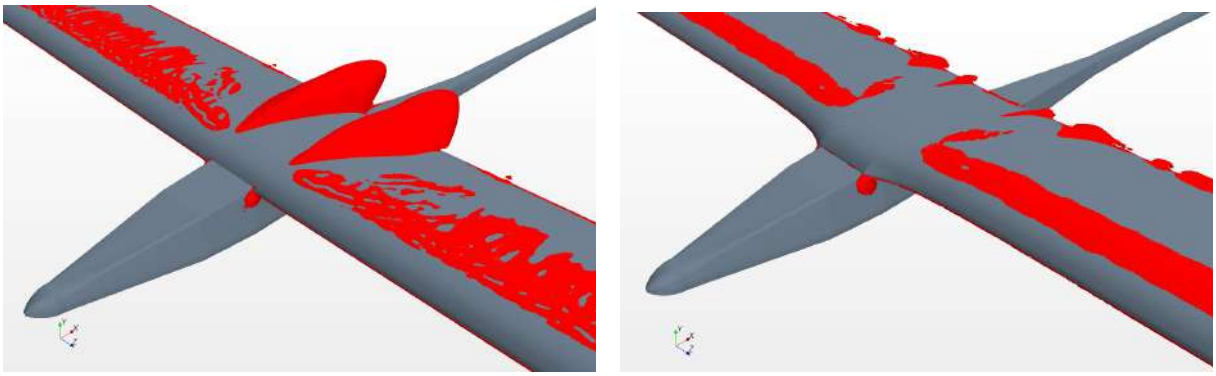

(a) Original LEEUAV configuration.

(b) LEEUAV with wing root fairing.

Figure 7.4: Isosurfaces of reversed flow in the wing root region, AoA=4º.

Figure 7.5 presents two charts of the lift and drag coefficients varying with the angle of attack. In those sub-figures one can compare the aerodynamic data from the original design and the one obtained

with the wing root fairing. The lift coefficient is smaller although very similar to the original configuration. As it was expected, due to the region of reversed flow mitigation in the wing root region, there is a decrease in the drag coefficient. Even though the drag coefficient decreased, so did the lift coefficient which proved that at least at the simulated angles of attack there were no gains in the lift-to-drag ratio.

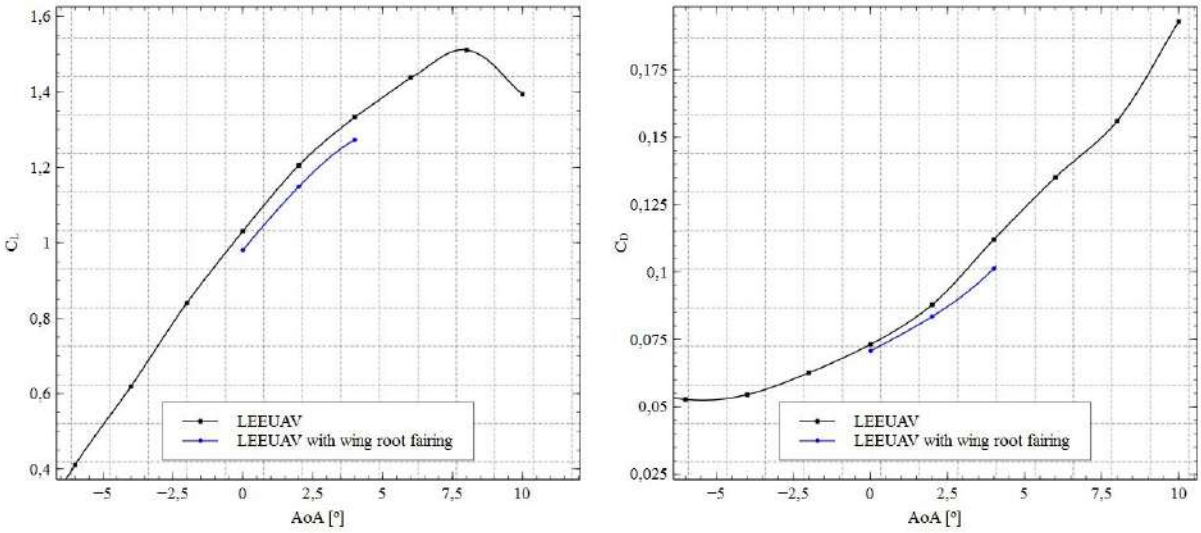

(a) C_L versus AoA.

(b) C_D versus AoA.

Figure 7.5: LEEUAV with wing root fairing aerodynamic performance charts.

7.3 Nose Shape

The original nose design, as Figure 7.6 a) shows, does not promote a smooth geometric transition with the fuselage. In the original nose design, its small length and angular generatrix produce significant adverse pressure gradients that promote flow transition. As Figure 7.6 b) shows, a solution to the original design was achieved by increasing the nose length by 20 mm and decreasing the generatrix curvature so that the transition between the nose and fuselage becomes smoother. Figure 7.7 shows the nose pressure coefficient as a function of position in the Ox direction, for the upmost and downmost nose surface in the yOx plane of symmetry, at an angle of attack of 0º. In that figure the x coordinates appear to have negative values due to the fact that the nose was designed to be in the negative side of the Ox axis. Apart from the stagnation areas at both nose tips, the proposed nose design evidences lower pressure gradients and pressure peaks. The proposed design almost does not present adverse pressure gradients at the simulated angle of attack, thus proving to be an improvement to the original design.

7.4 Wing Washout

Wing washout consists in reducing the lift distribution on the wing surface in the wingspan direction. There are a number of ways to adjust the lift distribution over the wing and one of those is ensured

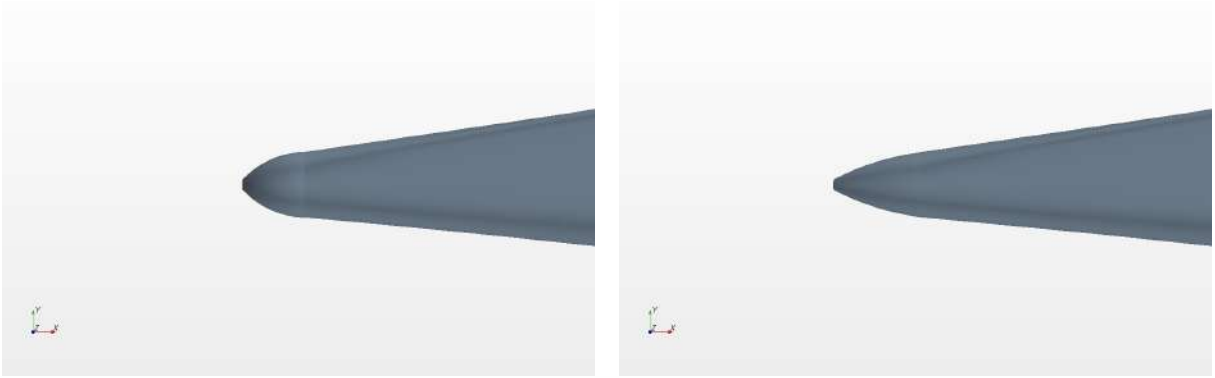

(a) Original nose shape design.

(b) Proposed nose shape design.

Figure 7.6: LEEUAV nose shape comparison.

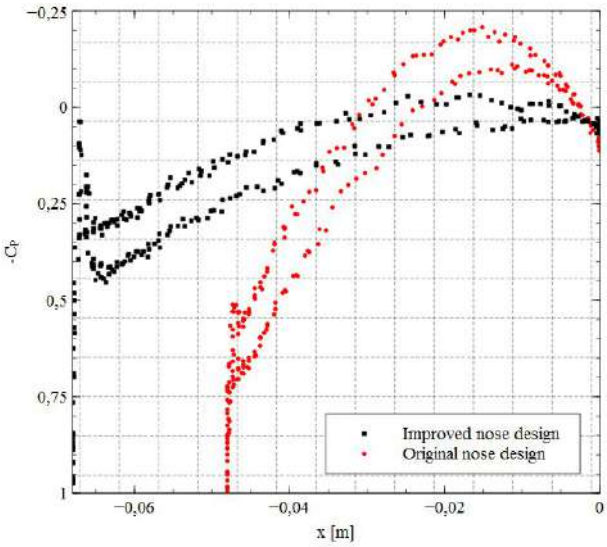

Figure 7.7: LEEUAV nose C_p curves comparison, AoA=0º.

by reducing the wing section incidence angle, or twist angle, from the wing root to the wingtip. The consequence is that at high angles of attack, when an airplane starts to experience lift loss, which generally occurs when the flow is no longer attached to the wing surface due to high adverse pressure gradients, the flow that is expected to be detached in the wing root region is not in the wingtip region. This way, controlling the aircraft trough the ailerons is still possible.

With the objective of ensuring the flow is still attached to the wing surface at the aileron regions, the incidence angle at wing section S3 was reduced in 4º. The performed studies showed that only when reducing that wing section incidence angle in 4º or more, would the air flow remain attached to the wing. Originally, every wing section had a positive 5º incidence angle with respect to the fuselage longitudinal axis.

Figure 7.8 compares the regions of reversed flow at an angle of attack of 10º between the original LEEUAV design and the one with wing washout. Reducing the wing twist proved to reduce flow separation in the wing region where the ailerons are located, thus guarantying aileron control at that angle of attack. There is a decrease in the lift coefficient of 7% and 20% in the drag coefficient.

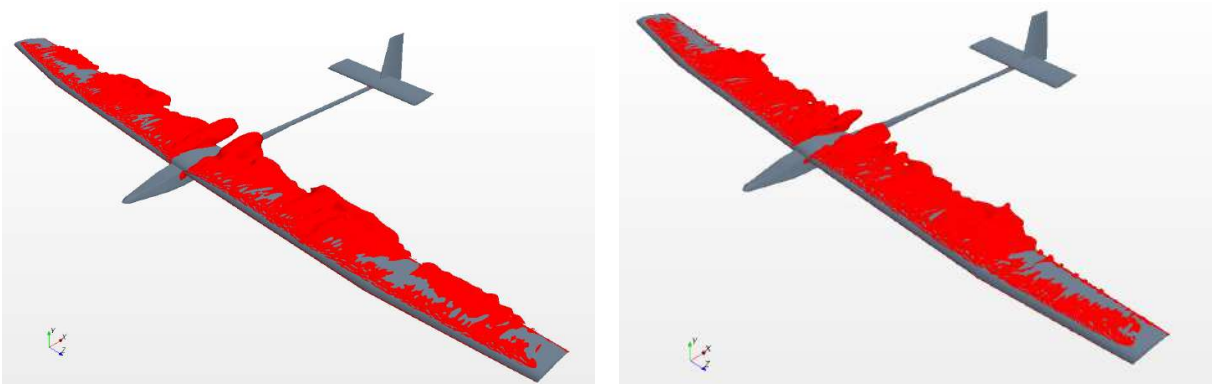

(a) Original LEEUAV configuration.

(b) LEEUAV with wing washout.

Figure 7.8: LEEUAV isosurfaces of reversed flow, AoA=10º.

7.5 General Parametric Conclusions

In this chapter, several modifications of the LEEUAV original geometry were proposed with the objective of improving its cruising flight performance.

The first design proposal was related to the wingtip geometry and the laminar separation bubbles length. The original LEEUAV wingtip design was truncated rather than rounded thus hindering the natural flow transition from the lower to the upper wing surfaces. Promoting the flow transition using a rounded wingtip surface will help locate the wingtip vortex on the wing upper surface thus reducing the aforementioned laminar separation bubbles. With the new geometry there was a slight decrease in the wing LSB as Figure 7.1 shows.

The wing root region proved to be producing considerable regions of separated flow in the original LEEUAV design at angles of attack above 2º. With the wing root fairing a smooth transition between the fuselage and wing was ensured thus eliminating the aforementioned region of separated flow at the simulated angles of attack. Although the new design proved fundamental in the drag decrease, there was as well a lift decrease which did not improve the lift-to-drag ratio.

Regarding the LEEUAV nose design, the original geometry proved to produce significant adverse pressure gradients which are a well known catalyst for natural flow transition. The new nose design proved to promote, at the simulated angles of attack, less intense or no adverse pressure gradients which may delay the flow transition around the fuselage.

The maximum lift angle of attack was determined to occur at 8º, whereupon massive flow separation would occur on the wing upper surface, beginning at its leading edge. As the flow would separate on the wing surface, the area where the ailerons would be positioned, would as well be in the region of separated flow which would decrease or make it impossible to maneuver the aircraft with those control surfaces. Reducing wing section S3 incidence angle by 4º proved to significantly reduce the separated flow regions from wing section S2 to S3 thus enabling aileron control at angles of attack up to 10º.

From the performed studies, it is advised to promote studies at the structural and financial levels regarding the adaptation of the LEEUAV wingtips, wing root fairing and modified nose geometries.

Chapter 8

Conclusions

8.1 Achievements

At the beginning of this document, the objectives of this thesis were addressed and consisted of the development of a CAD tool that enabled the swift parametric design of generic UAV geometries and their aerodynamic evaluation using high-fidelity models. Furthermore, one UAV in particular, the LEEUAV, would be virtually built using the developed CAD tool and aerodynamically evaluated and parametrically optimized.

Using FreeCAD as the CAD software package and the developed scripts, it was proved that not only was it possible to design generic UAVs, the user would only need to write Python scripts and let the CAD program design the aircraft shape, thus eliminating the need to use the CAD program graphical interface. This software package also proved to comply with a list of objectives such as the possibility of using both Windows and Linux as the working operating systems and the generation of sane geometry and mesh files that are fully supported by the CFD software where the aerodynamic simulations will be performed. Apart from the previous characteristics, FreeCAD is also open source which is highly desirable from a financial point of view. The developed CAD scripts can be divided in five segments or actions which consist in importing all the required FreeCAD modules required to effectively build a generic UAV, the acknowledgment of the geometric constraints, the geometric constraints verification, the building and assembly of generic UAV components like the wing or fuselage and finally, the export of geometric and mesh files containing the three-dimensional aircraft that will be used in the aerodynamic simulations.

Considering the aerodynamic simulations, a number of CFD software packages were researched but ultimately Star-CCM+ was the software of choice. Prior to using specific physics, meshing and turbulence models, first there was the need to perform validation tests using reliable sources. During the validation phase, two turbulence models were employed in the aerodynamic simulations where it was determined that only the $k-\omega$ SST turbulence model used together with the $\gamma - Re_\theta$ transition model provided valuable lift and drag data. The SA turbulence model was also employed in the aerodynamic simulations and proved to provide valuable lift data but failed when needed to predict drag related phe-

nomena such as natural transition. Only when using the Turbulence Suppression model, which required the knowledge of the transition locations, would the drag data be in agreement with the experimental data. Afterwards, using the knowledge from the validation studies, the flow around the LEEUAV airfoil was simulated at different angles of attack which provided an understanding of what aerodynamic behaviors were to expect later at a three-dimensional level. Still at a two-dimensional level, two solar panel configurations were simulated in order to understand their effects when installed on the wing upper surface. From the performed simulations it was understood that both configurations forced flow transition at the panel leading edge which in turn contributed to lift reduction and drag increase. The conclusion was that the solar panel on the wing must be installed in such a way that no surface discontinuities are present. Afterwards, now at a three-dimensional level, several aerodynamic simulations were performed having in consideration the LEEUAV cruise flight phase. As it was expected, two-dimensional aerodynamic effects such as the laminar separation bubbles are present on the wing surfaces. The selected mesh and physics models allowed to capture aerodynamic phenomena such as the spanwise laminar separation bubbles of varying length and thickness along the LEEUAV wing which are a consequence of the flow natural transition, regions of separated flow located at the wing leading edge at the extremes of the simulated angles of attack, the effects of the interaction between the fuselage and wing boundary layers and the flow bypass transition on the tail surfaces which are located on the LEEUAV turbulent wake.

Regarding the LEEUAV cruise flight performance, some of the conceptual design expected performance parameters were met and some were not. For example, the expected lift-to-drag ratio was 20 when the one obtained through the aerodynamic simulations was 14.01. This discrepancy suggests CFD analyses should be employed at the conceptual design phase. The predicted and obtained stall speeds are very similar which is approximately 6.21 m/s. The expected maximum speed was 21.1 m/s while the value obtained using the aerodynamic simulations and data from reference [19] indicate that the maximum speed would be approximately 29.3 m/s. There may be a number of reasons why the computed and conceptual performance parameters are not the same. At the conceptual phase, low-fidelity methods were employed in the computation of the aforementioned performance data. As an example, the lift-to-drag ratio which accounts for all the three-dimensional effects of the lift and drag such as the LSBs, regions of separated flow or transition phenomena, it is hardly rigorous to predict that performance ratio based on relations that determine the lift and drag information based on aircraft characteristics such as its weight or wingspan and on empirical relations, historical data, tabulated parameters and definitions alike.

The SA turbulence model was again employed now at a three-dimensional level to understand what are the consequences of using this model in the lift and drag predictions. The conclusions are that, similarly to the two-dimensional aerodynamic simulations, the lift coefficient is accurately predicted and is in line with the data obtained when using the $k-\omega$ SST turbulence model and the $\gamma - Re_\theta$ transition model at angles of attack where aerodynamic phenomena such as flow separation are not present or present at a small scale. Once more the drag data differs from what was obtained using the $k-\omega$ SST turbulence model with the $\gamma - Re_\theta$ transition model. In terms of the required CPU time for the residuals

to converge, this model is clearly superior. In conclusion, at angles of attack close to 0º and when one can manage to over or underpredict an aircraft drag coefficient and when time is of the essence, the use of the SA turbulence model is recommended. However, if there is the need to better predict the drag coefficient, then the $k-\omega$ SST turbulence model used with the $\gamma - Re_\theta$ transition model should be employed.

Some shape improvements were proposed to the baseline LEEUAV which consisted in modifying the wing, fuselage and nose geometries. The wingtip shape modification proposal consisted in creating a rounded wingtip to improve the air flow passage from the pressure to the wing suction side thus reducing the wing upper surface LSB length. Having a rounded wingtip proved to reduce the LSB length while slightly reducing the drag coefficient. Another wing modification had to do with the aileron control surfaces which were located inside a region of reversed flow at angles of attack above 8º. With the proposed modification, at 10º, although there are regions of reversed flow starting at the wing leading edge, the flow on the wing surface where the ailerons are located is still attached to the wing thus enabling roll control at least until that angle of attack. Due to the interaction between the fuselage and wing boundary layers, above angles of attack of 2º, a region of separated flow starts to develop at the wing leading edge in the wing root region. A solution to this problem was achieved by implementing a wing root fairing which ensured a smooth geometric transition between the wing and fuselage. With this modification and at the simulated conditions, no region of separated flow was detected in the wing root region and there was a reduction in the drag coefficient. The original nose shape also proved to induce significant adverse pressure gradients which might trigger natural flow transition in those surfaces. With the proposed nose shape, at the simulated angle of attack, little to no adverse pressure gradients were detected which shows improvement in the original shape.

Throughout the aerodynamic evaluation of the two validation airfoils, LEEUAV airfoil, LEEUAV and proposed shape modifications, a total of 3.5 TB and 60,000 CPU hours were required to achieve the results presented in this thesis.

The work developed in this thesis inserts itself in an optimization cycle. Starting at the geometric constraints level where the designer states the UAV geometric dimensions, the CAD scripts then build and assemble the designed UAV shape and export several geometry and mesh files to be used by the CFD software. After the aerodynamic simulations, the engineer then decides if one particular geometry suits the projects objectives or if there is the need to improve any feature.

8.2 Future Work

In terms of future work and interesting ideas to implement in the scope of this thesis and project, there are a few concepts that might be interesting to think about.

As it was stated in the third and sixth chapters, only the cruise flight phase was considered in the LEEUAV design and three-dimensional analyses. However, during the entire flight mission profile a number of other flight conditions are encountered. It would be interesting to simulate the effects of crosswinds which are a common occurrence during takeoffs and landings. Another interesting study

would be to simulate the effects of coordinated turns. For such studies it would be necessary to evaluate the entire aircraft, which is easily done by mirroring the LEEUAV geometry with respect to the yOx plane of symmetry and later aerodynamically evaluate the entire aircraft.

Another interesting idea would be to simulate the effects of control surfaces like ailerons, rudder and elevators. In terms of the CAD scripts, it would be fairly easy to develop such geometries since it only requires the import of the selected airfoils, the cutting of the original geometry at the required places and the positioning of the new control surfaces. One aspect to have in mind is that the inclusion of these surfaces adds discontinuities to the original geometry, which will have its toll on the aircraft aerodynamic performance.

The inclusion of wingtip devices such as end plates or winglets would as well be an interesting study to cope with the wing lift induced drag.

Since the LEEUAV will be a light aircraft, its landing gear will probably be fixed rather than actuated by electric motors that would increase its weight. If that is the case, then the landing gear should be aerodynamically evaluated to understand its contribution to the total aircraft drag.

The LEEUAV fuselage was designed using ten cross-sections. Although the boom and tail geometries are sufficiently defined, the fuselage region comprising the cargo and electronics bay could be improved by the insertion of additional cross-sections thus making it a smoother surface.

The LEEUAV will have a propeller in the nose region and its effect on the flow was not studied. It would be interesting to do so since the propeller is transmitting energy to the fluid which should delay natural transition around the fuselage. Possibly, the region of separated flow in the wing root region might be reduced which would consequently reduce the drag.

It would be interesting to make a battery of tests with a scaled model of the LEEUAV inside a wind-tunnel to understand what is the relation with the aerodynamic simulations. Because no wind-tunnel or flight and ground tests were performed yet, there is no real certainty that the studied aerodynamic phenomena will actually behave the way it was predicted. The aerodynamic simulations do not include effects such as random wind gusts, fluid-structure interaction, skin deformation or the effect of a real aircraft with its surface imperfections and control surfaces.

With the objective of making the aerodynamic evaluation phase of the UAV cost free, it would be interesting to promote the transition from the licensed Star-CCM+ software to an open source program.

Bibliography

[1] Robert Graves. *Greek Myths: Illustrated Edition*. Penguin Group, 1955.

[2] Daniel Arasse. *Leonardo da Vinci*. Konecky and Konecky, 2005.

[3] Carvalho. *História dos Balões*. Relógio d'Água, 1991.

[4] Charles Gillispie. *The Montgolfier Brothers and the Invention of Aviation*. Princeton University Press, 1992.

[5] Gibbs-Smith Charles. *Sir George Cayley Father of Aerial Navigation*. Royal Society of London, 1962.

[6] Peter L. Jakab and Tom D. Crouch. *The Wright Brothers and the Invention of the Aerial Age*. National Geographic Books.

[7] Robert L. Hirsch, Roger Bezdek, and Robert Wendling. Peaking of World Oil Production: Impacts, Mitigation & Risk Management. 2005.

[8] I. Allison et. al. The Copenhagen Diagnosis: Updating the World on the Latest Climate Science. *UNSW Climate Change Research Center*, page 11, 2009.

[9] The Global Climate 2001 – 2010: A Decade of Climate Extremes Summary Report. *World Meteorological Organization*, (1119), 2013.

[10] Reg Austin. *Unmanned Aircraft Systems*. Wiley, 2010.

[11] Project Sunrise. `https://www.projectsunrise.info/`, 2014.

[12] Nasa Armstrong Fact Sheet: Pathfinder Solar-Powered Aircraft. `https://www.nasa.gov/centers/armstrong/news/FactSheets/FS-034-DFRC.html/`, 2014.

[13] Airbus Space and Defense. Solar Powered High Altitude Pseudo-Satellite Successful Test Flight. `https://www.astrium.eads.net/en/news2/first-flight-of-astrium-s-zephyr-solar-haps.html/`, 2014.

[14] Solar Impulse 2. `https://www.solarimpulse.com/en/our-adventure/solar-impulse-2/`, 2014.

[15] Solar Impulse Across America. `https://www.solarimpulse.com/timeline/view/7356/`, 2014.

[16] A. C. Marta and P. Gamboa. *Conceptual and Preliminary Design Summary Long Endurance Electric UAV*. 2013.

[17] A. C. Marta and P. Gamboa. *Electric Long Endurance UAV*. 2013.

[18] XFOIL. https://www.web.mit.edu/drela/Public/web/xfoil/, 2014.

[19] Héctor Vidales. Design, Construction and Test of the Propulsion System of a Solar UAV. Master's thesis, Instituto Superior Técnico, 2013.

[20] DLR Institute of Aeronautics and Flow Technology. *Electric Flight - Potential and Limitations*, Lisbon, Portugal, October 2012.

[21] Solidworks. https://www.solidworks.com/, 2014.

[22] Terrafugia, Inc. https://files.solidworks.com/casestudies_eng/pdf/Terrafugia_FINAL1.pdf/, 2014.

[23] Dassault Systemes CATIA. https://www.3ds.com/product-services/catia/, 2014.

[24] Siemens NX. https://www.plm.automation.siemens.com/en_us/products/nx/, 2014.

[25] Openvsp. https://www.openvsp.org/, 2014.

[26] Salome. https://www.salome-platform.org/, 2014.

[27] Freecad. https://www.freecadweb.org/, 2014.

[28] Ansys Fluent. https://www.ansys.com/Products/Simulation+Technology/Fluid+Dynamic+Products/ANSYS+Fluent/, 2014.

[29] Cd adapco STAR-CCM+. https://www.cd-adapco.com/products/star-ccm/, 2014.

[30] Edge. https://www.foi.se/edge/, 2014.

[31] Tau DLR. https://www.tau.dlr.de/, 2014.

[32] Openfoam. https://www.openfoam.com/, 2014.

[33] Gregory A. Williamson, Bryan D. McGranahan, Benjamin A. Broughton, Robert W. Deters, John B. Brandt, and Michael S. Selig. *Summary of Low-Speed Airfoil Data*, volume 5. 2012.

[34] F. R. Menter. Two-Equation Eddy-Viscosity Turbulence Models for Engineering Applications. *AIAA Journal*, Volume 32(Number 8), August 1994.

[35] D. C. Wilcox. Multiscale Model for Turbulent Flows. *AIAA*, Vol. 26(No. 11):pp. 1311–1320, November 1988.

[36] W. P. Jones and B. E. Launder. The Calculation of Low Reynolds Number Phenomena with a Two-Equation Model of Turbulence. *Int. J. Heat Mass Transf.*, Vol. 16:1119–1130, 1973.

[37] F.R. Menter, R. B. Langtry, S. R. Likki, Y. B. Suzen, P. G. Huang, and S. Völker. A Correlation-Based Transition Model Using Local Variables - Part I: Model Formulation. *Journal of Turbumachinery*, 128, July 2006.

[38] R. B. Langtry, F.R. Menter, S. R. Likki, Y. B. Suzen, P. G. Huang, and S. Völker. A Correlation-Based Transition Model Using Local Variables - Part II: Test Cases and Industrial Applications. *Journal of Turbumachinery*, 128, July 2006.

[39] P. R. Spalart and S. R. Allmaras. A One-Equation Turbulence Model for Aerodynamic Flows. *AIAA*, 1992.

[40] Yongsheng Lian and Wei Shyy. Laminar-Turbulent Transition of a Low Reynolds Number Rigid or Flexible Airfoil. *AIAA Journal*, Volume 45(Number 7), July 2007.

[41] Stuart E. Rogers, Florian Menter, Paul A. Durbin, and Nagi N. Mansour. A Comparison of Turbulence Models in Computing Multi-Element Airfoil Flows. *AIAA*, 1994.

[42] P. Goding, D. W. Zingg, and T. E. Nelson. High-Lift Aerodynamic Computations with One- and Two-Equation Turbulence Models. *AIAA Journal*, Volume 35(Number 2), February 1997.

[43] John D. Anderson Jr. *Fundamentals of Aerodynamics*. McGraw-Hill, 2011.

[44] R. B. Langtry and F. R. Menter. Transition Modeling for General CFD Applications in Aeronautics. *AIAA*, 2005.

[45] John D. Anderson Jr. *Introduction to Flight*. McGraw-Hill, fifth edition, 2005.

[46] Sighard F. Hoerner and Henry V. Borst. *Fluid-Dynamic Lift Practical Information on Aerodynamic and Hydrodynamic Lift*. Mrs. Liselotte A. Hoerner, 1985.

Appendix A

Appendix

A.1 LEEUAV Dimensions and Input Parameters

Table A.1: LEEUAV wing dimensions and input parameters.

Wing cross-sections	4	Wing sweep between S1 and S2	0.0º
Wing chord at S0	350 mm	Wing sweep between S2 and S3	5.5º
Wing chord at S1	350 mm	Dihedral angle between S0 and S1	0.0º
Wing chord at S2	350 mm	Dihedral angle between S1 and S2	1.0º
Wing chord at S3	252 mm	Dihedral angle between S2 and S3	1.0º
Distance between S0 and S1	60 mm	Incidence angle at S0	-5.0º
Distance between S1 and S2	1340 mm	Incidence angle at S1	-5.0º
Distance between S2 and S3	850 mm	Incidence angle at S2	-5.0º
Wing sweep between S0 and S1	0.0º	Incidence angle at S3	-5.0º

Table A.2: LEEUAV fuselage dimensions and input parameters.

Fuselage cross-sections	10	Section S4 $r2\_4$	15 mm
Distance between S0 and S1	220 mm	Section S5 $R5$	15 mm
Distance between S1 and S2	100 mm	Section S6 $R6$	15 mm
Distance between S2 and S3	267 mm	Section S7 lu_7	28 mm
Distance between S3 and S4	260 mm	Section S7 h_7	16 mm
Distance between S4 and S5	755 mm	Section S7 $r1\_7$	2 mm
Distance between S5 and S6	111 mm	Section S7 $r2\_7$	15 mm
Distance between S6 and S7	107 mm	Section S8 lu_8	24 mm
Distance between S7 and S8	70 mm	Section S8 h_8	30 mm
Distance between S8 and S9	220 mm	Section S8 $r1\_8$	1 mm
Section S0 $R0$	25 mm	Section S8 $r2\_8$	1 mm
Section S1 lu_1	90 mm	Section S9 lu_9	12 mm
Section S1 h_1	62 mm	Section S9 h_9	32 mm
Section S1 $r1\_1$	10 mm	Section S9 $r1\_9$	1 mm
Section S1 $r2\_1$	30 mm	Section S9 $r2\_9$	1 mm
Section S2 lu_2	110 mm	Section S0 $delta\_y0$	10 mm
Section S2 h_2	75 mm	Section S1 $delta\_y1$	42 mm
Section S2 $r1\_2$	5 mm	Section S2 $delta\_y2$	50 mm
Section S2 $r2\_2$	30 mm	Section S3 $delta\_y3$	15 mm
Section S3 lu_3	82 mm	Section S4 $delta\_y4$	13 mm
Section S3 h_3	45 mm	Section S5 $delta\_y5$	10 mm
Section S3 $r1\_3$	1 mm	Section S6 $delta\_y6$	6 mm
Section S3 $r2\_3$	20 mm	Section S7 $delta\_y7$	6 mm
Section S4 lu_4	1 mm	Section S8 $delta\_y8$	6 mm
Section S4 h_4	15 mm	Section S9 $delta\_y9$	6 mm
Section S4 $r1\_4$	15 mm		

Table A.3: LEEUAV tail dimensions and input parameters.

Tail sections	5	VS chord at S0	250 mm
Dist. between HS S0 and S1	300 mm	VS chord at S1	150 mm
Dist. between VS S0 and S1	300 mm	VS chord at S2	250 mm
Dist. between VS S0 and S2	65 mm	HS sweep angle	0º
HS chord at S0	214 mm	HS dihedral angle	0º
HS chord at S1	214 mm	HS incidence angle	4º

Table A.4: LEEUAV nose dimensions and input parameters.

Radius $rn1$	25 mm
Radius $rn2$	4 mm
Length ln	48 mm

A.2 CAL1215J Validation Data

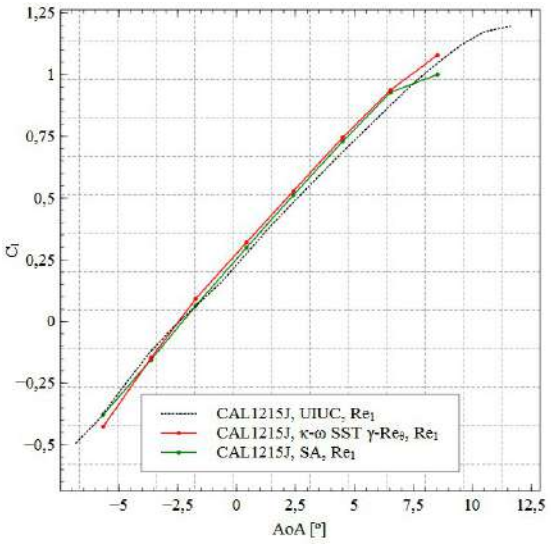

(a) C_l versus AoA.

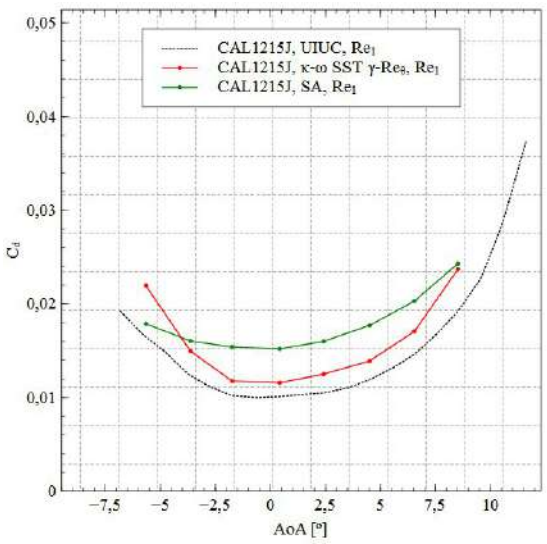

(b) C_d versus AoA.

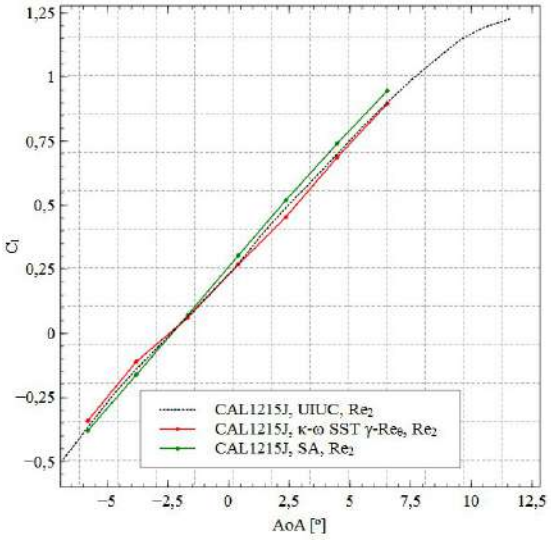

(c) C_l versus AoA.

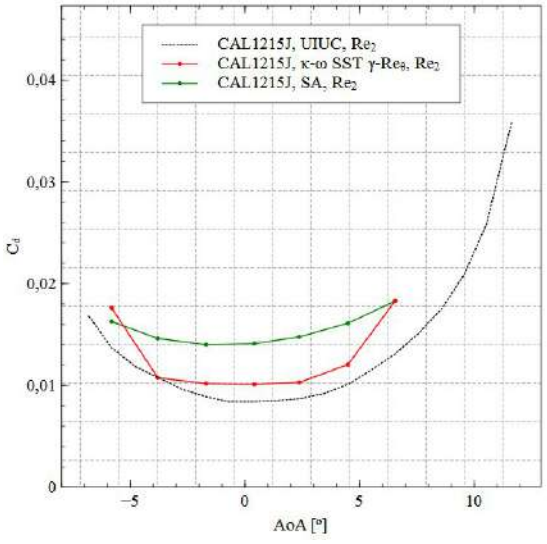

(d) C_d versus AoA.

Figure A.1: CAL1215J lift and drag coefficients at Re_1 and Re_2.

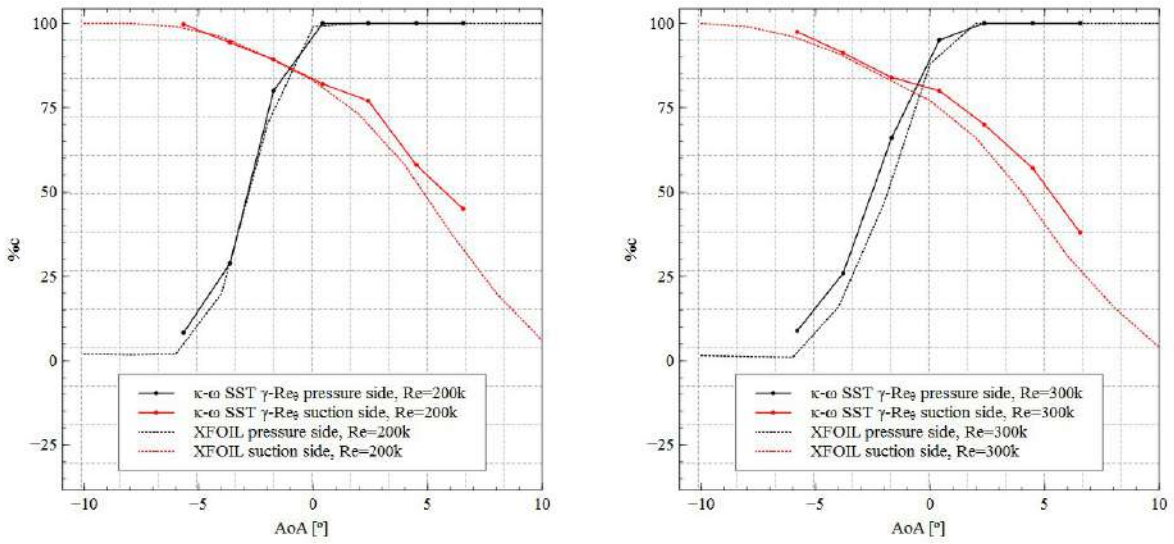

(a) Re_1 (b) Re_2

Figure A.2: CAL1215J, transition curves, XFOIL vs $k-\omega$ SST & $\gamma - Re_\theta$.

A.3 LEEUAV Aerodynamic Data

Figure A.3: Wingtip vortex, AoA=0°.

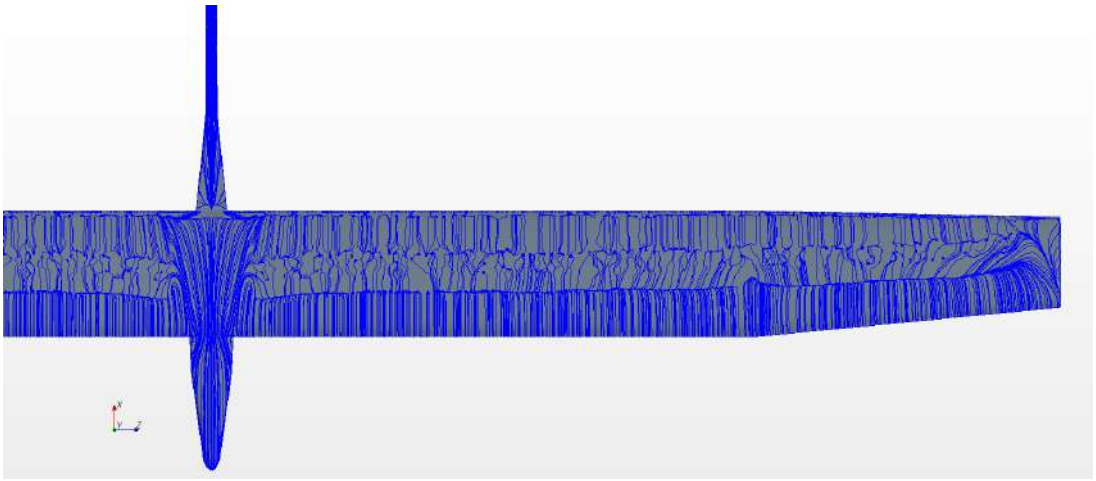

Figure A.4: LEEUAV surface streamlines, top view, AoA=0°.

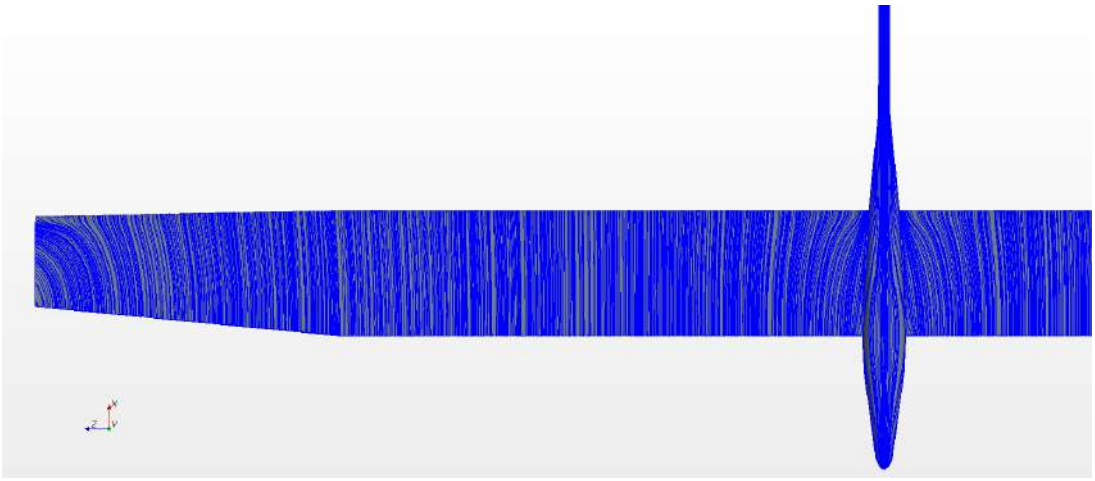

Figure A.5: LEEUAV surface streamlines, bottom view, AoA=0º.

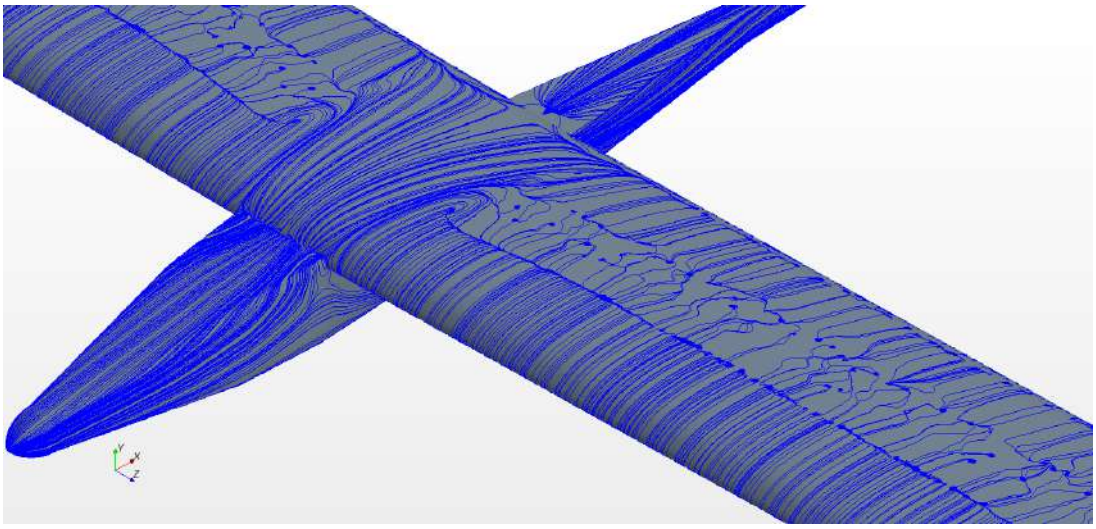

Figure A.6: LEEUAV surface streamlines, side view, AoA=0º.

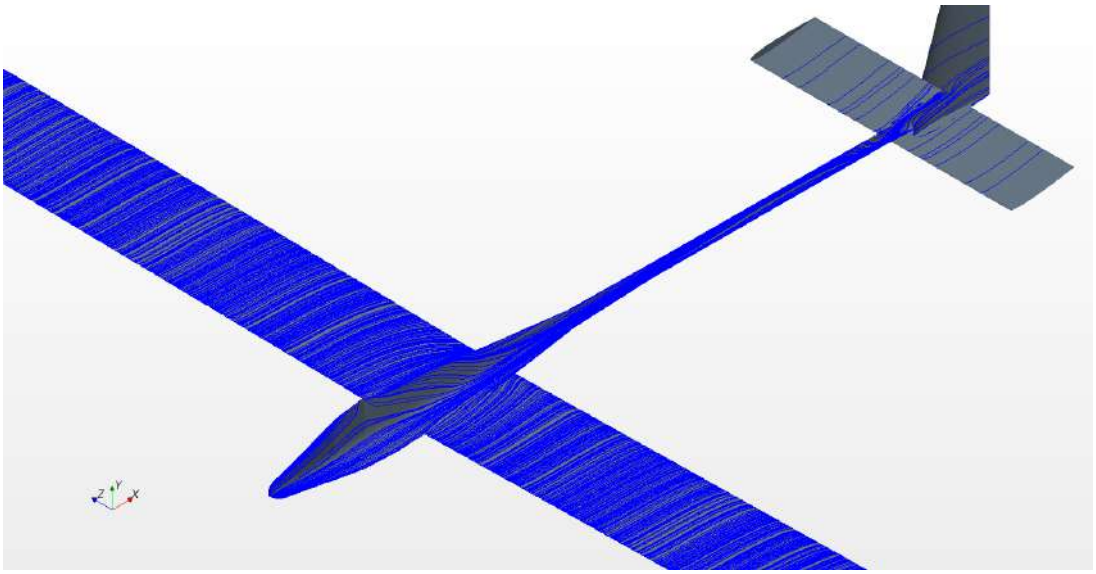

Figure A.7: LEEUAV surface streamlines, bottom side view, AoA=0º.

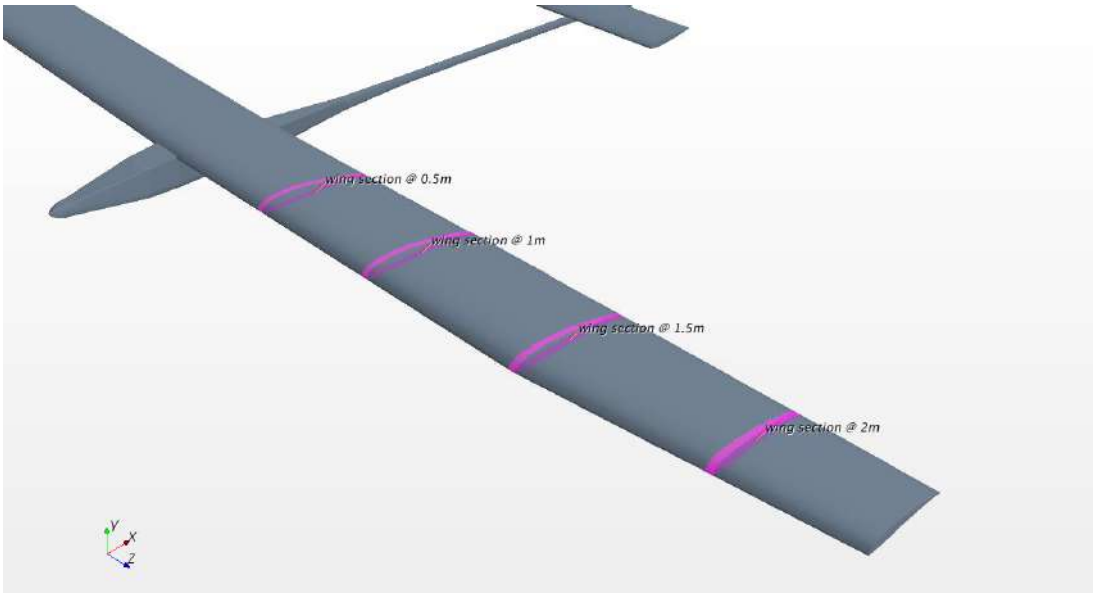

Figure A.8: Wing sections at z=500 mm, z=1000 mm, z=1500 mm and z=2000 mm.